



HAL
open science

Towards an electrically-injected optical parametric oscillator

Alice Bernard

► **To cite this version:**

Alice Bernard. Towards an electrically-injected optical parametric oscillator. Physics [physics]. Université Sorbonne Paris Cité, 2018. English. NNT : 2018USPCC104 . tel-02320246

HAL Id: tel-02320246

<https://theses.hal.science/tel-02320246>

Submitted on 18 Oct 2019

HAL is a multi-disciplinary open access archive for the deposit and dissemination of scientific research documents, whether they are published or not. The documents may come from teaching and research institutions in France or abroad, or from public or private research centers.

L'archive ouverte pluridisciplinaire **HAL**, est destinée au dépôt et à la diffusion de documents scientifiques de niveau recherche, publiés ou non, émanant des établissements d'enseignement et de recherche français ou étrangers, des laboratoires publics ou privés.

U-PC

Université Sorbonne
Paris Cité

université
PARIS
DIDEROT
PARIS 7

THESE DE DOCTORAT DE L'UNIVERSITE
SORBONNE PARIS CITE

PREPAREE A L'UNIVERSITE PARIS DIDEROT – PARIS 7

ECOLE DOCTORALE 564 : PHYSIQUE EN ILE-DE-FRANCE

LABORATOIRE MATERIAUX ET PHENOMENES QUANTIQUES

Towards an electrically injected optical parametric oscillator

Par Alice BERNARD

Thèse de doctorat de physique

Dirigée par Giuseppe LEO

Présentée et soutenue publiquement à Paris le 10 juillet
2018

Présidente du jury : Mme Angela VASANELLI
(Université Paris 7)

Rapporteurs : Mme Isabelle SAGNES
et M. Laurent VIVIEN (C2N)

Examineurs : M. Claudio CORIASSO (Prima Electro)
et M. Claude ALIBERT (Université de Montpellier)

Directeur de thèse : M. Giuseppe LEO (Université Paris 7)

Co-directeur de thèse : M. Jean-Michel GERARD (CEA)

Membre invité : M. Michel KRAKOWSKI (III-V Lab)

Remerciements

Mon travail s'est partagé entre deux centres de recherche, l'Université Paris 7 et le Commissariat à l'Energie Atomique. Je garde de ces deux endroits un excellent souvenir. Même si je remercie ici une poignée de gens, ce sont toutes les personnes avec qui j'ai interagi pendant la thèse qui m'ont fourni un environnement de travail optimal. Je souhaite également saluer l'UFR de Physique de Paris 7 pour la qualité des cours proposés, en particulier aux étudiants de première année, me donnant envie de continuer dans le domaine.

Je remercie mon directeur de thèse de m'avoir fait confiance pour porter un projet ambitieux et de m'avoir donné beaucoup de liberté. Giuseppe m'a fourni un environnement de travail stimulant, s'est toujours montré dynamique et motivé, et m'a donné beaucoup de temps, d'enthousiasme et de bonnes idées. Je remercie aussi Jean-Michel pour sa gentillesse, son calme, sa créativité, sa disponibilité constante et sa capacité infinie à résoudre les problèmes pratiques et théoriques. Merci également à mes rapporteurs, Laurent Vivien et Isabelle Sagnes, pour l'attention détaillée portée à mon manuscrit et pour leurs suggestions, ainsi qu'aux membres de mon jury, Claudio Coriasso, Claude Alibert, Michel Krakowski et Angela Vasanelli. Merci aussi à Philippe Adam, qui a montré un intérêt constant envers le projet et m'a aussi fait confiance pour le mener à bien.

Avant et pendant la thèse, il y a beaucoup de personnes que je voudrais remercier : merci donc à Sara Ducci pour l'intérêt des cours de son master et pour avoir été toujours présente pour orienter mes amis ou moi, et à Maria Amanti de m'avoir encadrée sur mes premières manips, de m'avoir donné la première occasion d'être co-auteur sur un article et de m'avoir conseillée par la suite. A Julien Claudon et Joël Bleuze, merci de leur gentillesse, leur culture scientifique et d'avoir toujours la porte ouverte pour une discussion. Je remercie aussi Yann Genuist pour ses exploits quotidiens avec la MBE et Yoann Curé pour ses coups de pouce avec la PL ou l'informatique. Merci à Alessio Andronico pour les outils développés et sa bonne humeur, à Marco Ravaro pour ses mesures et suggestions, à Yohan Désières pour ses conseils avisés, à Badhise Ben Bakir pour des discussions stimulantes, et à Jean-Luc Rouvière et Edith Bellet-Amalric pour avoir caractérisé mes échantillons avec talent. Je souhaite aussi remercier les doctorants et post-doctorants pour leur accueil, en particulier Cécile Ozanam et Silvia Mariani. Merci à William Hease

d'avoir été toujours disponible pour débattre passionnément de fabrication en salle blanche, même depuis l'Autriche, et à Tiphaine Dupont d'avoir pris une soirée pour me parler de l'intégration III/V sur Si. Merci à Romain Fons d'avoir pris la relève pour les derniers échantillons, et à Tobias Sattler et Alberto Artioli pour les blagues et les longues conversations. Pour les échanges de matériel, les discussions et la bonne humeur, je remercie Fares, Biswarup, Mehdi, Natalia, Valerio, Pierre, Eduardo, Debora, Samanta, Carlo, Iannis, Daria, Yacine, Guillaume, Claire et les autres. Je remercie aussi les permanents, qui nous prêtent du matériel et facilitent notre quotidien : Ivan Favero, Régis André, Moïra Hocevar, Eva Monroy, Bruno Gayral, Christophe Durand, Joël Eymery, Henri Mariette, Joël Cibert, Jean-Phillipe Poizat, Bruno Daudin, Didier Boilot...

Je tiens aussi à saluer les ingénieurs de salle blanche, qui tiennent une place centrale dans notre travail. Merci donc à Stephan Suffit pour son humour et pour m'avoir formée au top niveau du MEB, ainsi qu'à Christophe Manquest et Pascal Filloux. Côté PTA, je n'aurais jamais pu réaliser les structures de cette thèse sans l'aide de Thierry Chevolleau et Thomas Charvolin, que je remercie chaleureusement. Merci également à Jean-Luc Thomassin de m'avoir débloquée de nombreuses fois pendant des lithographies, ainsi qu'à Marlène Terrier, Christophe Lemonias, Nicolas Chaix, Frédéric Gustavo, Michaël Rosticher et Loïc Becerra.

Je remercie aussi le personnel administratif pour leur efficacité et leur sympathie : Joëlle Mercier, Jocelyne Moreau, Anne Servouze et Céline Conche. Côté électronique et mécanique, merci à Marc Apfel, Alain Cangemi, Patrick Lepert et Martial Nicolas pour leur compétence et leur gentillesse.

Je remercie chaleureusement Michel Krakowski pour sa disponibilité et son efficacité, ainsi que Bruno Gérard et Olivier Parillaud pour leur place capitale dans ce projet.

Enfin, merci aux amis et à la famille, en particulier Vincent pour son humour, Mathias pour avoir fait disparaître les problèmes pendant la soutenance et avant, et Pedro pour son soutien constant. Et naturellement, mes parents pour tout.

Contents

List of figures	vii
List of tables	xii
List of acronyms	xiii
Introduction	1
1. Three-wave mixing in GaAs	11
1.1 Nonlinear optics in plane waves	11
1.1.1 From the nonlinear polarization to the coupled equations	11
1.1.2 Three-wave mixing processes	13
1.1.3 Second-harmonic generation	14
1.1.4 Optical parametric amplification	16
1.2 Nonlinear optics in waveguides	17
1.2.1 Effective area	17
1.2.2 SHG in the presence of losses	18
1.2.3 OPA in the presence of losses	20
1.2.4 OPA in the presence of gain	21
1.3 OPOs	22
1.3.1 Single pass DROPO	23
1.3.2 Double-pass DROPO	25
1.3.3 TROPO	27
1.4 Phase-matching strategies in GaAs	33
1.4.1 Form birefringence	34
1.4.2 Quasi-phase matching	35
1.4.3 Modal phase matching	37
2. QD and QW laser diodes	41
2.1 Phenomenological description of lasers	41

2.1.1	Optical gain in a two-level system	41
2.1.2	Laser threshold condition	42
2.1.3	Loss sources	45
2.1.4	Efficiency	46
2.2	Gain in semiconductors	48
2.2.1	Fermi Golden Rule.....	49
2.2.2	Bulk case.....	50
2.2.3	Quantum wells.....	53
2.2.4	Quantum dots	55
2.3	Optical selection rules	59
3.	Diode-OPO: concept and design	63
3.1	Phase-matching bandwidth and quantum dots laser spectrum.....	64
3.2	Choice of epitaxial structure.....	66
3.2.1	Refractive index model.....	66
3.2.2	Phase matching.....	67
3.2.3	Modal selection.....	70
3.2.4	Phase-matching tolerances.....	74
3.3	Choice of the doping profile.....	76
3.3.1	Doping profiles in the GaAs-based diode.....	77
3.3.2	Doping profiles in the InP-based diode	79
3.3.3	Modal gain necessary for laser threshold	81
3.3.4	Threshold current	82
3.3.5	Additional loss sources for signal and idler	84
3.4	Conclusion	85
4.	Laser characterizations	87
4.1	Optical setup.....	87
4.2	Basic characteristics.....	88
4.3	Far field measurements.....	91
4.4	Comparison of far field and internal parameters	93

4.5	Effect of trapped carriers outside the camelback.....	95
4.6	Conclusion.....	96
5.	Refractive index measurements	99
5.1	Justification.....	99
5.2	Principle of measurement.....	99
5.3	Sample fabrication and characterization.....	101
5.3.1	Growth.....	101
5.3.2	Composition measurement.....	101
5.3.3	Choice of grating period.....	103
5.3.4	Gratings fabrication.....	103
5.4	Measurement.....	105
5.4.1	Optical setup.....	105
5.4.2	Measurement procedure.....	106
5.5	Results.....	108
5.6	Discussion.....	110
5.6.1	Experimental accuracy.....	110
5.6.2	Comparison with literature.....	112
5.7	Conclusion.....	113
6.	Fabrication	115
6.1	Fabrication overview of ridge lasers.....	115
6.2	Choice of etch mask.....	116
6.3	Optical lithography.....	116
6.4	Mask roughness.....	120
6.5	ICP-RIE etching.....	121
6.5.1	Requirements.....	121
6.5.2	Principle.....	123
6.5.3	Etching mechanisms.....	124
6.5.4	Choice of chemistry.....	125
6.5.5	Results.....	125

6.5.6	Choice of parameters.....	127
6.5.7	Passivation layer.....	129
6.6	Removal of mask residues.....	129
7.	Double-cavity DOPO	133
7.1	Choice of coupling method	133
7.1.1	Evanescent couplers	134
7.1.2	Bragg-exchange.....	135
7.1.3	Adiabatic couplers.....	135
7.1.4	Adiabatic couplers physics in a nutshell.....	137
7.2	Critical points	139
7.3	Choice of geometry	140
7.4	Proposed design.....	140
7.4.1	Choice of material.....	142
7.4.2	Conversion efficiency and OPO threshold	143
7.4.3	Tolerances.....	144
7.4.4	DBR design.....	146
7.4.5	Tunability	146
7.4.6	Transfer.....	147
7.4.7	Laser.....	152
7.5	Conclusion	154
	General conclusion	146
	List of publications	149
	Bibliography	150

Résumé

Le travail présenté dans cette thèse porte sur la conception, la fabrication et la caractérisation de sources prévues pour fonctionner à la fois comme diode laser et comme oscillateur paramétrique optique. Ces lasers sont conçus pour émettre sur un mode d'ordre supérieur afin de permettre une conversion de fréquence paramétrique avec les modes fondamentaux du guide à la fréquence moitié. La diode laser et l'OPO partagent la même cavité optique ; pour assurer l'accord de phase et corriger les écarts à la structure nominale induits lors de l'élaboration par épitaxie, la largeur de ruban est utilisée comme paramètre de contrôle des indices efficaces. Les diodes proposées sont donc étroites (3-5 μm) et gravées profondément. En conséquence, il est potentiellement intéressant d'utiliser des boîtes quantiques pour limiter les recombinaisons non radiatives sur les flancs.

Dans le cadre de ce travail, nous avons conçu des diodes basées sur ce principe pour les deux systèmes GaAs/AlGaAs et InGaAsP/InP, qui permettent respectivement d'obtenir potentiellement une émission OPO au voisinage de 2 μm ou de 3 μm . Dans le cas de l'InGaAsP/InP, nous avons étudié au préalable l'indice de réfraction des alliages InGaAsP dans une plage de longueur d'onde jusque-là non couverte par la littérature. Ces données ont été acquises via des mesures d'indice efficace (m-lines) de couches guidantes d'InGaAsP épitaxiées en accord de maille sur un substrat d'InP. Pour des structures laser-OPO optimisées, les simulations montrent que le seuil OPO devrait être obtenu pour une puissance de pompe intracavité de quelques centaines de mW, qu'il est réaliste d'atteindre pour des diodes laser à l'état de l'art. Nous avons étudié les propriétés électro-optiques de diodes lasers à puits quantiques GaAs/AlGaAs réalisées sur la base de nos dessins; l'observation de l'effet laser sur le mode TE₂ valide le dessin vertical original de nos diodes lasers. En vue de la fabrication de laser-OPO à ruban étroit, nous avons développé des procédés de fabrication nouveaux sur la Plateforme Technologique Amont (CEA – Grenoble), notamment la gravure profonde (>10 μm) par ICP-RIE. Enfin, nous avons proposé un concept alternatif de diode-OPO, comprenant des cavités laser et OPO distinctes couplées par un taper adiabatique.

Mots-clés: diode laser, Fabry-Pérot, Oscillateur Paramétrique Optique, épitaxie par jet moléculaire, guide d'onde, photonique intégrée, AlGaAs, InGaAsP, boîtes quantiques, puits quantiques, mesures d'indice efficace, gravures par ICP-RIE.

Abstract

The work presented in this thesis deals with the design, fabrication and characterization of sources intended to function as both laser diodes and optical parametric oscillators. These lasers are designed to emit on a higher order mode to allow parametric frequency conversion with fundamental modes of the guide at half frequency. The laser diode and OPO share the same optical cavity; to ensure phase matching and correct nominal structure deviations induced during epitaxial processing, the ridge width is used as a control parameter of the effective indices. The proposed diodes are therefore narrow (3-5 μm) and etched deeply. Consequently, it is potentially interesting to use quantum dots to limit non-radiative recombination on the sidewalls.

In the context of this work, we have designed diodes based on this principle for the two GaAs/AlGaAs and InGaAsP/InP systems, which respectively allow to potentially obtain an OPO emission in the vicinity of 2 μm or 3 μm . In the case of InGaAsP/InP, we previously studied the refractive index of InGaAsP alloys in a wavelength range not covered by literature to this day. This data was acquired via effective m-line index measurements of InGaAsP guiding layers epitaxially grown on and lattice-matched to an InP substrate. For optimized laser-OPO structures, simulations show that the OPO threshold should be obtained for an intracavity pump power of a few hundred mW, which is realistic to achieve for state-of-the-art laser diodes. We have studied the electro-optical properties of GaAs/AlGaAs quantum well laser diodes made on the basis of our designs; the observation of the laser effect on the TE₂ mode validates the original vertical design of our laser diodes. For the manufacture of narrow-ridge lasers-OPOs, we have developed new manufacturing processes on the Plateforme Technologique Amont (Upstream Technology Platform, CEA - Grenoble), including deep etching (> 10 μm) by ICP-RIE. Finally, we have proposed an alternative diode-OPO concept, comprising distinct laser and OPO cavities coupled by an adiabatic taper.

Keywords:

Laser diode, Fabry-Perot, Optical Parametric Oscillator, Molecular beam epitaxy, waveguide, integrated photonics, GaAs, AlGaAs, InP, InGaAsP, quantum dots, quantum wells, micro fabrication, electronic lithography, efficient index measurement, m-lines, grating coupler, adiabatic coupler, ICP-RIE dry etchings.

List of figures

Figure 1. Simplified diagram of the band structure of a laser diode, a QCL and an ICL.	3
Figure 1-1. Three-wave mixing interactions	14
Figure 1-2. SHG conversion efficiency for different values of coherence length.....	16
Figure 1-3. Normalized SHG conversion efficiency vs. normalized phase mismatch	16
Figure 1-4. Normalized SHG conversion efficiency, $L=1 \text{ cm}^{-1}$, for $\alpha_{\omega} = 0$ and $\alpha_{2\omega} = 0, 1, 2, 3$ and 4 cm^{-1}	19
Figure 1-5. SHG conversion efficiency as a function of propagation length, for different levels of losses.	19
Figure 1-6. OPA gain vs. L	21
Figure 1-7. Common OPO configurations	22
Figure 1-8. Pump threshold in a DROPO at degeneracy.	24
Figure 1-9. Mode diagram of a DROPO.....	25
Figure 1-10. Variation of the pump and signal/idler fields in different types of OPOs	26
Figure 1-11. Ratio of single-pass to double-pass DROPO threshold as a function of phase mismatch and mirror phase shift parameter	27
Figure 1-12. Simulation of the fields propagating in a single-pass DROPO	30
Figure 1-13. Simulation of the fields propagating in a laser-OPO, treated like an unfolded double-pass DROPO.	30
Figure 1-14. Variation of TROPO threshold power with pump amplification.	31
Figure 1-15. Variation of the pump power threshold as a function of phase-matching coefficient and mirror phase-shift parameter.....	32
Figure 1-16. Types of phase-matching	34
Figure 1-17. Index modes profile and type of phase-matching employed in form-birefringent AlGaAs waveguides.....	35
Figure 1-18. Generated power as a function of L/Lc for various phase matching schemes.....	35
Figure 1-19. Fabrication process of orientation-patterned GaAs	36
Figure 1-20. Quantum well intermixing.....	37
Figure 1-21. Snake waveguides	37
Figure 1-22. Intensity of the interacting modes and type of phase-matching employed in a waveguide engineered for SHG	38

Figure 2-1. Possible interactions of a two-level system with a photon of resonant energy	42
Figure 2-2. Variation of the amplitude of a field injected at the cavity entrance	42
Figure 2-3. Maximal material gain in a GaAs QW vs 2D carrier density	44
Figure 2-4. Inverse differential quantum efficiency as a function of laser cavity length	46
Figure 2-5. Density of states in a semiconductor for structures of decreasing dimensionality	49
Figure 2-6. Gain diagram of a bulk semiconductor	51
Figure 2-7. Position of quasi-Fermi levels difference – gap vs. electron concentration for GaAs	52
Figure 2-8. Gain in bulk GaAs	52
Figure 2-9. Gain diagram in a quantum well	54
Figure 2-10. Gain in a quantum well vs. 2D carrier density	55
Figure 2-11. Normalized maximal gain vs. 2D carrier density in GaAs	55
Figure 2-12. Light emission spectra of a quantum dot laser at different temperatures	57
Figure 2-13. Calculated material gain for different quasi-Fermi levels in case of a QW and QD active layer	58
Figure 2-14. Potential and particle wave function in the envelope function approximation	59
Figure 3-1. Type-II phase matching in the DOPO waveguides at degeneracy	66
Figure 3-2. Left: epitaxial structure of the GaAs-based diode	67
Figure 3-3. Epitaxial structure and interacting modes of the InP-based diode	68
Figure 3-4. Index mismatch as a function of ridge width and pump wavelength in the GaAs-based diode	68
Figure 3-5. Index mismatch as a function of ridge width and pump wavelength in the InP-based diode	69
Figure 3-6. Tunability out of degeneracy of the GaAs-based diode.	70
Figure 3-7. Tunability out of degeneracy of the InP-based diode	70
Figure 3-8. First symmetric modes supported by the waveguides in the GaAs and InP-based diodes for different numbers of quantum wells	73
Figure 3-9. Confinement factors for TE ₀ and TE ₂ in multi QW DOPOs and their ratio, as a function of the number of QWs	73
Figure 3-10. Variation of the normalized conversion efficiency with ridge width for the GaAs-based diode	75
Figure 3-11. Variation of the normalized conversion efficiency with ridge width for the InP-based diode	76

Figure 3-12. OPO threshold as a function of signal/idler propagation losses, for several values of normalized conversion efficiency, resonator length and reflectivity	77
Figure 3-13 Bandgap and three doping profiles of the GaAs-based structure	78
Figure 3-14. Voltage-current curves corresponding to the different doping profiles presented in figure 3-13.....	78
Figure 3-15. Doping profiles in the InP structure.....	80
Figure 3-16. Voltage-current curve corresponding to the different doping profiles presented in figure 3-15.....	80
Figure 3-17. Modal gains required to reach the lasing threshold for the GaAs-based and InP-based QW diodes	82
Figure 3-18. Material gains required to reach the lasing threshold for the GaAs-based and InP-based QW diodes.....	82
Figure 3-19. Threshold current densities for the GaAs-based and InP-based QW diodes.	83
Figure 3-20. Threshold current density for a single layer of quantum dots for the GaAs-based QD diode.....	84
Figure 4-1. Optical setup used for lasers characterization.....	87
Figure 4-2. Surface series resistance as a function of laser length.....	88
Figure 4-3. Threshold current density as a function of laser length	89
Figure 4-4. Light-current curve of laser chip n° 1402 against a liner fit above threshold.....	89
Figure 4-5. Optical spectrum of laser chip n° 1402 below and above threshold.....	91
Figure 4-6. Predicted far field intensity for modes TE ₀₀ and TE ₂₀ (fundamental and first even mode in the direction of growth) vs. angle along the fast axis.....	91
Figure 4-7. Far field of different lasers.	92
Figure 4-8. Far field patterns at different currents for two lasers of different lengths	93
Figure 4-9. Far field on the fast axis for a 4 mm laser	93
Figure 4-10. Inverse of differential efficiency as a function of length.....	94
Figure 4-11. Comparison between far field and optical spectrum in a 1 mm laser ...	95
Figure 4-12. Required material gain at threshold with and without carrier accumulation between cladding and camelback.....	96
Figure 5-1. Coupling condition.....	101
Figure 5-2. Difference to the formula proposed by [139], for the relation between Ga and As fraction in InGaAsP lattice-matched to InP	102
Figure 5-3. Optical setup for index measurement.	105
Figure 5-4. Elements of the rotating setup.	107

Figure 5-5. Example of coupling measurement at a wavelength of 1.55 μm	108
Figure 5-6. Determination of the refractive index and thickness for a slab of $\text{In}_{0.67}\text{Ga}_{0.33}\text{As}_{0.72}\text{P}_{0.28}$ at $\lambda = 1.55 \mu\text{m}$	109
Figure 5-7. Determination of the refractive index and core thickness for a slab of $\text{In}_{0.67}\text{Ga}_{0.33}\text{As}_{0.72}\text{P}_{0.28}$ on InP at a wavelength of 1.55 μm	109
Figure 5-8. Refractive index measured at 1.55, 2.12 and 3.1 μm vs. y.	110
Figure 5-9. Refractive index of InGaAsP lattice-matched to InP vs. wavelength. ...	112
Figure 6-1. General overview of ridge lasers fabrication.....	115
Figure 6-2. General view of the processes used to define AlGaAs structures	118
Figure 6-3. Masks used for AlGaAs dry etching and resulting structures.....	122
Figure 6-4. SiN dry etching	122
Figure 6-5. Metal mask undulation	123
Figure 6-6. RIE and ICP-RIE chambers	123
Figure 6-7. Main processes involved in RIE etching.	124
Figure 6-8. Examples of large ($>1 \mu\text{m}$) structures etched by ICP-RIE.....	126
Figure 6-9. Results of ICP-RIE etching of GaAs with the parameters given in Table 6-1.....	126
Figure 6-10. Example of structures etched by ICP-RIE.....	126
Figure 6-11. Etch in typical conditions with and without helium leak in the chamber.	128
Figure 6-12. Result of a single ICP etching on pillars of various sizes	128
Figure 6-13. Result of ICP etches in typical conditions at different temperatures... 130	130
Figure 6-14. Early example of ICP etch.	130
Figure 6-15. View of a cleaved waveguide facet before mask removal.....	130
Figure 7-1. Example of evanescent coupling	135
Figure 7-2. Bragg-exchange coupler.....	135
Figure 7-3. Adiabatic coupler.....	136
Figure 7-4. Resonant coupling	137
Figure 7-5. Eigenmodes in an adiabatic coupler. Index mismatch varies continuously from left to right.....	138
Figure 7-6. Transfer in a resonant coupler.	139
Figure 7-7. General view of the proposed coupled-cavity design.	142
Figure 7-8. Effective indices of guided modes in the structure.....	143
Figure 7-9. SPDC efficiency vs. ridge width in a 0.95 μm thick waveguide surrounded by $\text{Al}_{0.8}\text{Ga}_{0.2}\text{As}$ and air.	143
Figure 7-10. OPO pump power threshold for a ridge width of 4 μm and 2 μm as a function of length and signal/idler reflectivity.....	144

Figure 7-11. Normalized SPDC efficiency as a function of ridge width and thickness.	144
Figure 7-12. Normalized SPDC efficiency as a function of ridge width and thickness, for a waveguide temperature of 20°C and 50°C.....	145
Figure 7-13. Normalized SPDC efficiency as a function of ridge width and thickness, for pump wavelengths of 990 nm and 1010 nm.	145
Figure 7-14. Tunability curves of the waveguide supporting frequency conversion.	147
Figure 7-15. Transverse view of the structure.	148
Figure 7-16. BPM simulation of light propagation in the structure and normalized guided power along z , in the upper and lower waveguides	148
Figure 7-17. Modal decomposition of the BPM-simulated field in figure 7-16 on the eigenmodes of the GaAs waveguide.....	149
Figure 7-18. Side and top view of the proposed taper geometry	150
Figure 7-19. Power transmitted to the eigenmodes in figure 7-20	151
Figure 7-20. Four eigenmodes of the ridge GaAs waveguide of width 2 μm	151
Figure 7-21. Model used to estimate the laser temperature rise	152
Figure 7-22. Junction temperature as a function substrate thickness, for three laser lengths.	153

List of tables

Table 1. Characteristics of the materials used for three-wave mixing in this thesis (GaAs and InP) compared to LiNbO ₃	7
Table 3-1. Modal reflectivities of the first even modes in the structures presented earlier.....	71
Table 3-2. Sources of variations in the effective index mismatch for the structures presented earlier	74
Table 3-3. FCA-induced losses for the first two even modes of the waveguide at λ_p and the fundamental TE mode at $2x \lambda_p$ in the GaAs-based diode.	79
Table 3-4. FCA-induced losses for the first two even modes of the waveguide at λ_p and the fundamental TE mode at $2x \lambda_p$ in the InP-based diode.....	80
Table 3-5. Losses due to FCA in a single quantum well for the structures presented above.....	84
Table 4-1. Summary of laser characteristics.....	90
Table 5-1. Physical properties and measured indices of the studied samples	111
Table 5-2. Parameters of the one-oscillator fit inferred from the index measurements.	113
Table 6-1. Typical parameters used for ICP-RIE etches of AlGaAs.	125
Table 6-2. Typical parameters used for ICP-RIE etches of SiN.	126
Table 7-1. Data sheet of a typical AlGaAs laser.....	134
Table 7-2. Compatibility of different coupler types with the DOPO project	136
Table 7-3. Advantages and drawbacks of different coupling geometries.	141
Table 7-4. Layer structure proposed for the coupled-cavity design.	142
Table 7-5. Coupling constants for fundamental TE and TM modes at 2 μm , given a rectangular grating of depth 200 nm and duty cycle 50%.....	146

List of acronyms

AR	Active Region
BPM	Beam Propagation Method
DFG	Difference-Frequency Generation
DP-DROPO	Double-pass Doubly Resonant Oscillator
DROPO	Doubly Resonant Oscillator
DWELL	Dot in a well
FCA	Free Carrier Absorption
FSMB	Fixed Stage Moving Beam
FWHM	Full Width at Half Maximum
ICL	Interband Cascade Laser
ICP-RIE	Inductively Coupled Plasma - Reactive Ion Etching
LI	Light-Intensity
NL	Nonlinear
OP	Orientation Patterned
OPA	Optical Parametric Amplification
OPO	Optical Parametric Oscillator
MBE	Molecular Beam Epitaxy
NIR	Near Infrared
PPLN	Periodically Poled Lithium Niobate
QD	Quantum Dot
QCL	Quantum Cascade Laser
QPM	Quasi-Phase Matching

QW	Quantum Well
RK	Runge-Kutta
SFG	Sum-Frequency Generation
SHG	Second Harmonic Generation
SK	Stranski-Krastanov
SPDC	Spontaneous Parametric Down-Conversion
SROPO	Singly Resonant Optical Parametric Oscillator
TIR	Total Internal Reflection
TROPO	Triply Resonant Optical Parametric Oscillator

Introduction

Photonics can be described as a field of research started by the invention of the laser [1] and expanded by a transfer of technology from microelectronics. While it spans all aspects of light manipulation, the term “photonics” usually designates it as a cousin of electronics, manipulating photons like electronics manipulates electrons. Two years only after the first operation of a laser, stimulated emission was demonstrated in GaAs diode lasers [2,3]. Since then, new applications appeared at the junction between the two fields. Miniaturization of the components starting with the laser allowed new products to reach the general public thanks to mass fabrication and compactness. Today the field of photonics covers a large number of applications ranging from optical telecommunications, data storage and possibly optical computing in the future to health, defense and security.

Many building blocks of photonic circuits have been demonstrated on silicon, but its lack of a direct band gap has hindered the demonstration of a laser in this material. While Si lasers based on engineered Si-based materials or Raman transitions have been demonstrated [4], the effective usefulness of these techniques is still hampered by low efficiency or lack of electrical pumping. Meanwhile, a large technology developed around III/V laser diodes. After their first demonstration in GaAs, they were based on AlGaAs ternary alloys because of their quasi-null lattice mismatch over their composition range. Then other families were added, like InGaAsP, GaInSb, AlGaInP, InGaN, and now II-VI materials. Threshold currents have been reduced by several orders of magnitude with the introduction of confined heterostructures and progress in epitaxial growth. To date, laser diode technology is best developed in GaAs and InP platforms, and present research in these fields concentrates on the addition of new functionalities.

In the absence of efficient Si-based lasers, silicon photonics relies on the integration of external III/V emitters. To date, two techniques are commonly used for III/V on Si integration. In heterogeneous integration, building blocks from different materials are connected: this method requires delicate coupling and alignment. The other method, which relies on bonding wafers with a polymer, has led to the demonstration of efficient III/V-Si hybrid lasers but does not scale well in mass production. Epitaxy of III-V materials directly on Si is considered a promising solution for large-scale fabrication [5], although it is still at the development stage (the field is going through a renewal after an initial interest in the 90's [6]).

Nowadays, with the progress of the last years on new materials, the total spectrum covered by laser diodes has expanded from the near infrared (NIR) to the entire 400-3300 nm range. However, the emission wavelength of laser diodes is fundamentally set by the material interband transition energy and the constraint of using electronic transitions sets a limit on accessible wavelengths. Making green, orange or ultraviolet laser diodes is still challenging and blue LEDs became available only recently [7]. By exploiting other optical transitions, the spectrum accessible to laser sources has been broadly extended. The first non-diode semiconductor laser was the quantum cascade laser (QCL), proposed in 1971 [8] (figure 1.b). Its core principle is to engineer a superlattice of quantum wells (QWs) so that an electron can cascade down between intersubband levels. The first QCL was demonstrated in 1994 [9], after the development of molecular beam epitaxy (MBE) made it possible to grow semiconductor layers with a precision down to the atomic scale. The possibility of engineering the material transition levels makes QCLs very versatile sources, covering the 3 μm to 300 μm range to this day¹. Interband cascade lasers (ICL) are based on a similar concept: electrons cascade down a superlattice but undergo interband transitions (figure 1.c) in the 2-4 μm range. This scheme was proposed in 1995 [11] and demonstrated quickly after [12], but continuous wave (CW) room temperature operation was obtained only in 2008 [13].

To this day, these different sources cover the electromagnetic spectrum from the visible to the far-infrared range. However ICLs, which cover the gap between laser diodes and QCL, are still at an earlier stage of development. Yet the wavelength range from 2 to 4 μm is of particular interest in the spectroscopy community as it contains various rotational and vibrational peaks of atmospheric and hydrocarbon molecules. While resonances of spectroscopic peaks can be measured in the visible / NIR range, their absorption lines are orders of magnitude smaller than in the 2-4 μm range. Monitoring hydrocarbon species with high sensitivity would allow for more

¹ With the exception of the Reststrahlen band, from 28 to 30 μm . QCLs emitting at longer wavelengths are still limited to the cryogenic regime [10].

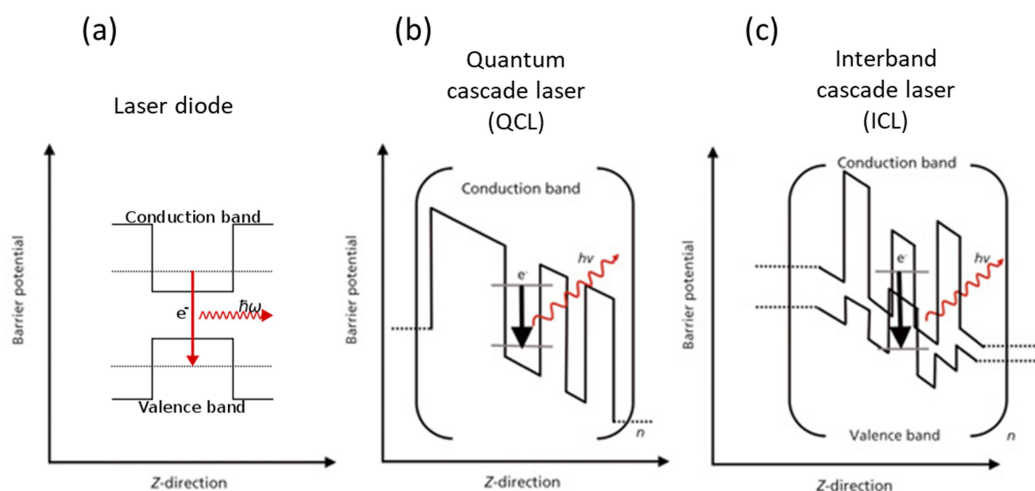


Figure 1. Simplified diagram of the band structure of a laser diode, a QCL and an ICL. In the former, carriers recombine between conduction and valence band levels and a limited number of active regions exist. In QCLs, periodic structures are built in which injected electrons undergo transitions between intersubband levels of QWs. After a radiative transition, carriers are injected into another period (injection region are indicated by dashed lines). ICLs operate with a similar principle, but carriers undergo interband transitions.

Figures taken from [14,15].

efficient production, transportation and combustion systems [16]. Methane and carbon dioxide detectors, particularly, are currently sparking interest for environmental monitoring and detection of gas leaks [17]. Other areas of applications include defense and security, with spectral signatures of explosives and biochemical agents or their byproducts around $2\ \mu\text{m}$ [16], and the medical field, with the possibility of portable sensors of atmospheric gases to base diagnosis on breath analysis [18].

Presently, this wavelength range is only partly covered by laser sources. Material constraints limit QCL emission to relatively long wavelengths. Indeed, while emission at $3.4\ \mu\text{m}$ was demonstrated as early as 1998 [19], development to shorter wavelengths has been slow: the limit was pushed to $3.1\ \mu\text{m}$ in 2006 [20], then $2.75\ \mu\text{m}$ one year later [21]. However these sources are limited to a research environment and maximal operation of $\approx 10^\circ\text{C}$. The lowest wavelength achieved by a QCL to our knowledge is $2.65\ \mu\text{m}$ [22] at cryogenic temperatures (200K). At room T and in continuous wave (CW), the current limit is still above $3\ \mu\text{m}$ [23]. Bridging the gap from the shorter wavelength side, GaSb diodes have demonstrated emission in the $2\text{-}3\ \mu\text{m}$ range [24] and have been used for gas sensing in research environments [25], but at the moment they are not commercially available. ICLs, on the other hand, are

available to the general public - albeit at a high price. Several groups have demonstrated spectroscopic detectors based on ICLs around 3 μm [26,27].

In addition to emission in a particular wavelength range, sources used for spectroscopy should be tunable. This can be induced by changing the peak gain wavelength or cavity resonance. In a standard integrated laser, wavelength is tuned by control of current and temperature, namely through thermo-refractive effect to shift cavity resonance, and through temperature dependence of the gap. Both settings affect the emitted power so that wavelength is not tunable independently of power output. Tunability with these means is limited to a few tens of nanometers and as a consequence, laser diode emitters are usually optimized for the detection of a single chemical species. Several solutions have been developed to produce more widely tunable sources, in order to expand the range of tracked species and increase measurement precision.

A way to do this is via an array of distributed feedback (DFB) lasers providing a wide overall frequency covering by overlapping single lasers ranges [28]. This technique, proposed by [29], is cheaper than fabricating and aligning individual laser diodes because all DFB gratings can be defined on the same wafer. Although a very good wafer homogeneity is required, this technique is well established commercially: companies like Daylight solutions or Pendar Technologies offer broad-spectrum sources based on this principle. QCLs are particularly powerful in that respect because their gain spectrum can be engineered to be as large as desired. A source based on this concept, called heterogeneous QCL, demonstrated tunability from 5 to 10 μm [30]. However, while QCL arrays may be demonstrated in the short-wavelength range in the future, at the moment they operate mostly in the mid-infrared (MIR) range, where QCLs are better controlled.

External cavities also provide large tuning ranges when combined with wide gain sources. QCLs in external cavities are well developed, including for gas monitoring [31]. There has been a lot of effort to propose field-deployable sources, and [32] is an example of miniaturized hand-held external cavity setup. ICLs have also been integrated in external cavities, but they are more upstream to this day: for example [33] shows a tunability of 150 nm around 3.2 μm , albeit with an emitted power of only 4 mW.

In this context, nonlinear optics offers a solution for widely tunable sources from NIR to MIR. One of the effects arising from nonlinear susceptibility of a material is frequency conversion via three-wave mixing. In this case, differently from the

sources presented earlier, the involved energy levels are virtual: the constraint linked to using electronic transitions of the material disappears. All energy levels inside the gap are theoretically accessible and tunability is considerable. A common example of frequency conversion is provided by green lasers, which rely on the second-harmonic generation (SHG) from Nd:YAG or Nd:YVO₄ lasers at 1064 nm. Three-wave mixing has also been used to access the 2 - 4 μm region from the MIR emission of QCLs. In that case the nonlinear susceptibility is designed and resonant. The first demonstration of SHG in a QCL was in the 3.6 - 4.7 μm range [34], and SHG at 3.75 μm has also been demonstrated [35].

When a nonlinear medium is placed inside a cavity, a threshold may occur when its parametric gain exceeds losses, similarly to a laser threshold. This system is called an optical parametric oscillator (OPO). Like lasers, OPOs offer a coherent and monochromatic output, and moreover they are continuously tunable over hundreds of nanometers. Many macroscopic OPOs have been developed specifically for spectroscopic sensing in the NIR or MIR [36,37], and some companies offer in situ diagnostics based on these tools (e.g. Blue Industry and Science, Quantel Lasers). However, they are more delicate to control than lasers. This is mostly due to the phase-matching condition: waves at different frequencies must stay in phase, which sets a constraint on their refractive indices. For example, in the case of SHG, indices of fundamental and harmonic must be equal. This being generally impossible because of chromatic dispersion, birefringence is often used for frequency conversion. The phase-matching condition limits the types of suitable materials and makes OPOs very sensitive to environmental variations. To date, OPOs mostly remain bulky lab-based systems, operated by specialists of nonlinear optics.

Historically, the standard gain material of nonlinear optics is LiNbO₃, used for its birefringence, wide transparency range and high nonlinear quality factor². The first OPO was demonstrated with a birefringent LiNbO₃ crystal [38]. In 1993, periodically poled LiNbO₃ (PPLN) was fabricated by the application of an intense electric field on the material at the micrometric scale [39], enabling a novel phase-matching technique, called quasi-phase matching (QPM) [40]. Instead of controlling the

² The quality factor for three-wave mixing is $\chi^{(2)}/n^3$ where $\chi^{(2)}$ is the second-order susceptibility and n the refractive index (see chapter 1).

effective indices to satisfy phase relations, the fields are left free to go out of phase and the sign of $\chi^{(2)}$ is periodically reversed to compensate for this. Other periodically poled materials have been demonstrated, like ppKT, ppLiTaO₃, ppRTA... To date these crystals remain the most widely used in visible and NIR OPOs.

In parallel with the use of bulk crystals, there has been an effort to exploit frequency conversion in waveguides because they provide higher field intensities and interaction lengths. Despite the drawbacks of using waveguides, which are for the moment higher propagation losses and complex fabrication, today there is already a large range of integrated optical components in LiNbO₃, including PPLN waveguides for frequency conversion [41].

More recently, semiconductors have also been used for frequency conversion, enabling the integration of light generation, conversion, processing and detection on the same chip. These materials often have remarkable nonlinear properties compared to ferroelectric crystals (see table 1).

While there is a large field of research on nonlinear processes in silicon, this crystal does not have second-order susceptibility (see chapter 1 for the definition of higher-order susceptibilities) because it presents inversion symmetry. As a consequence, three-wave mixing processes cannot occur in it unless strain is induced. Frequency conversion and OPOs based on four-wave mixing in Si have been demonstrated, but the frequencies involved in these processes are in the same range. Thus these sources cannot provide access to a different part of the optical spectrum as in the case of three-wave mixing.

On the other hand, III/V compounds have a second-order susceptibility. To date, most of nonlinear optics in III/Vs occurs in GaAs because of its high quality factor and mature technology.

GaAs was not commonly used in frequency conversion before the 1990's because it lacks birefringence, like all cubic crystals. Several techniques (which we will revisit in chapter 1) have been developed to satisfy phase matching in this material.

Historically, the first phase-matching technique makes use of orientation-patterned GaAs (OP-GaAs). Nonlinear optics based on GaAs expanded dramatically after the first fabrication of this material [43], which quickly led to the demonstration of an OPO [44]. Today OP-GaAs in macroscopic cavities shows performances comparable to traditional media, with e.g. CW output power over 3 W, 45 % efficiency and $M^2=1.5$ [45,46]. To date, losses at short wavelength and a complex fabrication

technology hinder the exploitation of OP-GaAs waveguides in the NIR, while a MIR OPO based on a OP-GaAs waveguide was demonstrated in 2012 [47]. At present propagation losses and the lack of GaAs-based source at 2 μm remain the main limitation of this platform. For this reason, OP-GaSb is being developed to integrate source and QPM conversion in the same material [48], and upstream material studies for orientation-patterning in other III/Vs are starting to emerge [49,50].

Material	Refractive index n (at $\lambda = 1 \mu\text{m}$)	2nd-order susceptibility d_{eff} [pm/V] (at $\lambda = 1 \mu\text{m}$)	Figure of merit d_{eff}^2/n^3 [pm/V]	Thermal conductivity [W/m.K]
LiNbO ₃	2.2 ³	25	59	5.6
GaAs	3.5	170	674	45
InP	3.29	130 ⁴	474	68

Table 1. Characteristics of the materials used for three-wave mixing in this thesis (GaAs and InP) compared to LiNbO₃. d_{eff} is the most used nonlinear coefficient. Note that in AlGaAs and InGaAsP, alloy scattering decreases the thermal conductivity down to 1 order of magnitude.

Another technique to make GaAs exploitable for guided-wave nonlinear optics is based on form birefringence through the insertion of thin layers of different index, as proposed in [51]. This scheme originally relied on layers of different Al content in AlGaAs, but was limited by the low index contrast. Oxidation of layers with high Al content [52] permitted the demonstration of an OPO threshold in a micrometric waveguide [53]. To further increase index contrast, it was proposed to use selective etching in order to create a structure pierced by thin layers of air [54]. To date, the main limit of the AlOx-based technique is set by the losses induced by impurities leftover from the oxidation process. More fundamentally, this scheme cannot be easily integrated with electrical injection since AlOx layers are insulating. Furthermore, symmetry conditions of GaAs limit use of this technique to TM-polarized pumps. This is a strong limitation since common semiconductor sources in the near-infrared are QW laser diodes, with TE polarized emission.

³ Manufacturer value.

⁴ Extrapolated from [42] with Miller's rule.

Both the above methods are based on complex material patterning that introduces propagation losses and other intrinsic limitations. Fortunately, a third phase-matching strategy exists, which is relatively easy to implement and does not require significant deviations from traditional laser and waveguide design: modal phase matching. This technique simply relies on the engineering of modal dispersion in a waveguide to compensate for material dispersion. Among the possible schemes, a significant one is the use of Bragg and total-internal reflection (TIR) modes, introduced in [55]. This design has led to the demonstration of a twin-photon source [56] and a twin-photon laser diode [57]. Intracavity conversion in a laser diode [58] has also been achieved, as well as a widely tunable source around 2 μm [59]. However, no OPO based on modal phase matching has been demonstrated to date, regardless of several design proposals [60,61].

Despite five decades of progress after the invention of the first OPO, no electrically injected OPO on-chip has been demonstrated, although OPO threshold was reached in optically pumped waveguides [47,53] and intracavity conversion was obtained in a laser diode [58].

In this context, this thesis presents the work towards optical parametric oscillation inside a laser diode. We describe the design of two sources, based on GaAs (InP) for emission at 1 μm (1.55 μm) and down-conversion around 2 μm (3 μm). These emitters would provide widely tunable sources in the 2-4 μm range.

The design presented in this thesis is based on modal phase matching, since this technique is compatible with electrical injection and TE-polarized sources in the NIR. Ridge width is used as a degree of freedom to control phase mismatch after epitaxy in narrow, deeply etched waveguides. As a consequence, quantum dots (QDs) and dashes are proposed as active area medium in order to limit non-radiative recombination on the sidewalls [62].

The development of these sources is a joint project of Paris Diderot University, CEA Grenoble and the III-V Lab. Advances made during this thesis were shared between these labs and my PhD was split between Paris Diderot and CEA Grenoble. The original idea of diode-OPO, based on GaAs, is presented in [61]. The III-V Lab fabricated broad-area QW lasers based on this design and I characterized them. In parallel, I started establishing a fabrication process of narrow deeply-etched laser diodes. In addition, to transfer the concept to the InP platform, I built an m-lines setup and measured the refractive index of InGaAsP at 3 μm . Then, on the base of these measurements, I designed an InP-based phase-matched diode. Finally, I

conceived an alternative design for light generation and conversion in two distinct albeit monolithic cavities linked by a vertical coupler.

This work is organized as follows. *Chapters 1 and 2* are an introduction to the physics of the systems used in this thesis. Nonlinear optics in waveguides is presented in chapter 1 and QD / QW laser diodes in chapter 2. I focus particularly on doubly and triply resonant OPO thresholds, and on the impact of propagation losses for frequency conversion. Concerning laser diodes, this text is a general introduction but it shows the specificities of QW vs. QD diodes. *Chapter 3* presents the diode-OPO concept and the two designs based on this idea in the GaAs and InP platforms. In *chapter 4*, I report on my characterizations of broad area QW laser diodes based on the GaAs vertical structure. *Chapter 5* shows the refractive index measurements of InGaAsP in the NIR-MIR range, on which I established the design of chapter 2. *Chapter 6* is devoted to fabrication efforts undertaken to develop narrow, deeply-etched laser diodes. Finally, in *chapter 7* I provide an alternative design based on a vertical coupler.

1. Three-wave mixing in GaAs

We give here an overview of three waves mixing processes in waveguides. Optical parametric amplification (OPA) and oscillation (OPO) are described in the cases of null or finite propagation losses. We extend our description to the case of a triply resonant oscillator (TROPO) and discuss phase-matching strategies in GaAs.

Nonlinear optics in plane waves

From the nonlinear polarization to the coupled equations

Frequency mixing and other nonlinear effects arise from the electronic response of a material under intense electric field. The basic description of polarization in a dielectric is

$$\vec{P}(\vec{r}, t) = \varepsilon_0 \chi \vec{E}(\vec{r}, t) \quad (1.1)$$

where ε_0 is the vacuum permittivity and χ is the dielectric susceptibility of the material.

Under limited electric field, this picture is sufficient. However, shortly after the first demonstration of lasers [1], their intense electric fields allowed for the demonstration of higher-order effects in the polarization [63]. In this description, for a homogeneous and time-invariant dielectric material, having a local response in time and space, the polarization is expressed as

$$\vec{P}(\vec{r}, t) = \varepsilon_0 \chi^{(1)} \vec{E}(\vec{r}, t) + \varepsilon_0 \chi^{(2)} \vec{E}(\vec{r}, t)^2 + \varepsilon_0 \chi^{(3)} \vec{E}(\vec{r}, t)^3 \dots \quad (1.2)$$

where $\chi^{(i)}$ is the i -th order susceptibility of the material, that is a tensor of rank $i+1$: $\chi^{(1)}$ is a 3×3 matrix, $\chi^{(2)}$ a $3 \times 3 \times 3$ tensor, etc. The first term of this equation corresponds to the linear response of the polarization, while the sum of other terms is commonly called “nonlinear polarization” or P^{NL} . The susceptibility amplitudes decrease very fast with their order, which is why they can only be revealed at high electric fields. The various components of the nonlinear susceptibility result in different effects. In particular, $\chi^{(2)}$ gives rise to three-wave mixing, $\chi^{(3)}$ to four-wave mixing, and so forth. Since this thesis concentrates on $\chi^{(2)}$ effects, we will ignore higher-order terms of P^{NL} .

Polarization in return feeds back the electric field. In a non-magnetic, isotropic and dielectric optical medium with no free charges or currents, the following wave equation stands [64]:

$$\Delta \vec{E} - \left(\frac{n}{c}\right)^2 \frac{\partial^2 \vec{E}}{\partial t^2} = \mu_0 \frac{\partial^2 \vec{P}^{NL}}{\partial t^2} \quad (1.3)$$

In other words, the nonlinear terms of the polarization act as source terms for the electric field.

To solve for \vec{E} in (1.3), it is usual to write the electric field as a superposition of plane waves in Fourier domain:

$$\vec{E} = \sum_n \frac{1}{2} \left\{ E_n(\vec{r}, \omega_n) \exp[i(\omega_n t - \vec{k}_n \cdot \vec{r})] \vec{e}_n + c.c. \right\} \quad (1.4)$$

where c.c. stands for complex conjugate.

Similarly, the second-order polarization can be developed in Fourier domain, by injecting (1.4) into (1.2). For energy conservation, each (angular) frequency is determined by the other two, which is why the argument of the polarization is often written as $(-\omega_l; \omega_m, \omega_n)$. Then, if the frequencies satisfy $\omega_l = \omega_m + \omega_n$, the component of $P^{(2)}$ along the i -th axis is:

$$P_i^{(2)}(\omega_l = \omega_m + \omega_n) = \frac{\epsilon_0}{2} \sum_{m,n} \sum_{j,k} \chi_{ijk}^{(2)}(-\omega_l; \omega_m, \omega_n) E_j(\omega_m) E_k(\omega_n) \quad (1.5)$$

The nonlinear susceptibility can be simplified thanks to symmetry of the material. For example, in centrosymmetric crystals like Si, susceptibility tensors of even rank vanish. Far from the material resonances, where dispersion is negligible, Kleinman symmetry applies. As a consequence, the tensor $\chi_{ijk}^{(2)}$ can be written in a contracted form $d_{il} = (1/2) \chi_{ijk}^{(2)}$. The l index corresponds to (j, k) pairs and ranges from only 1 to 6 thanks to symmetries of the material reducing the number of independent components. (The factor $1/2$ is present for historical reasons). In GaAs, the only non-vanishing element of d_{il} is d_{14} , equal to ≈ 120 pm/V in the NIR.

We will now consider an electric field made of three monochromatic plane waves at ω_1 , ω_2 and $\omega_3 = \omega_1 + \omega_2$. Injecting (1.4) and (1.5) into (1.3) with the slowly-varying-envelope approximation yields the following coupled equations:

$$\frac{dE_1}{dz} = -i \frac{\omega_1 d_{\text{eff}}}{n_1 c} \frac{D}{2} E_3 E_2^* e^{-i\Delta k z} \quad (1.6a)$$

$$\frac{dE_2}{dz} = -i \frac{\omega_2 d_{\text{eff}}}{n_2 c} \frac{D}{2} E_3 E_1^* e^{-i\Delta k z} \quad (1.6b)$$

$$\frac{dE_3}{dz} = -i \frac{\omega_3 d_{\text{eff}}}{n_3 c} \frac{D}{2} E_1 E_2 e^{i\Delta k z} \quad (1.6c)$$

where Δk , defined as $k_3 - k_1 - k_2$, is called the *phase mismatch*; n_i is the refractive index at ω_i ; d_{eff} an effective nonlinear susceptibility (determined by waves polarizations and crystal symmetries); and D a degeneracy factor equal to 2 if the wave at ω_1 and ω_2 are distinguishable, and 1 otherwise.

These are the fundamental equations describing frequency mixing in nonlinear optical media. From there we can make the following remarks. Firstly, unless phase mismatch is null, the oscillating term $e^{-i\Delta k z}$ prevents consistent build-up or depletion of the fields. Control of the phase mismatch is thus critical to frequency mixing. This can also be interpreted as a conservation of the total photon momentum: $k_3 = k_1 + k_2$. Secondly, the coupled equations of nonlinear optics yield fundamental conservation relations. In a quantum description, the photon flux at ω_i is given by $I_i / (\hbar\omega_i)$ where I_i is the intensity. The quantities I_i/ω_i are then proportional to the flux of photons per unit time per unit area for the frequency ω_i and the coupled equations can also be expressed as

$$\frac{d}{dz} \left(\frac{I_1}{\omega_1} \right) = \frac{d}{dz} \left(\frac{I_2}{\omega_2} \right) = -\frac{d}{dz} \left(\frac{I_3}{\omega_3} \right) \quad (1.7)$$

These conservation relations are known as *Manley-Rowe relations*. They convey the conservation of energy during the frequency mixing process in a quantum description: for each photon destroyed at ω_3 , one has to appear at ω_2 and one at ω_1 .

Three-wave mixing processes

Figure 1-1 shows the processes allowed by three-wave mixing.

In *sum-frequency generation (SFG)*, two waves at frequencies ω_1 and ω_2 combine to create a wave at the sum frequency ω_3 . *Second-harmonic generation (SHG)* is a degenerate case of this process. In this case, a wave interacts with itself to create a field at the frequency $\omega_3 = 2 \omega_1$.

In *difference-frequency generation (DFG)* or *optical parametric amplification (OPA)*, a field at ω_3 (usually called the *pump* field) interacts with a field present at the crystal entrance (the seed), of frequency ω_2 , to generate a wave at ω_1 . Manley-Rowe relations

still apply, so the seed is amplified as well. The generated field of higher frequency and its complementary are usually called *signal* and *idler*, respectively.

Parametric fluorescence is similar to OPA, with the difference that no seed is present at the crystal input. This process is quantum in nature: an analogy can be made with the classical description of stimulated emission in lasers vs. quantum description of spontaneous emission.

The work presented in this thesis aims at an *optical parametric oscillator*. In this system, the nonlinear medium is placed inside a cavity resonating either at frequency ω_1 (singly-resonant OPO), ω_1 and ω_2 (doubly-resonant OPO) or ω_1, ω_2 and ω_3 (triple-resonant OPO). When nonlinear gain exceeds losses, a threshold appears in the converted light power, similarly to the case of a laser threshold: it is said that the system oscillates. While OPA can only be jump-started by parametric fluorescence, in a stable regime a constant signal / idler field exists and provides a seed for the three-wave mixing. These systems are described by the equations of OPA completed by self-consistent conditions after a cavity round-trip.

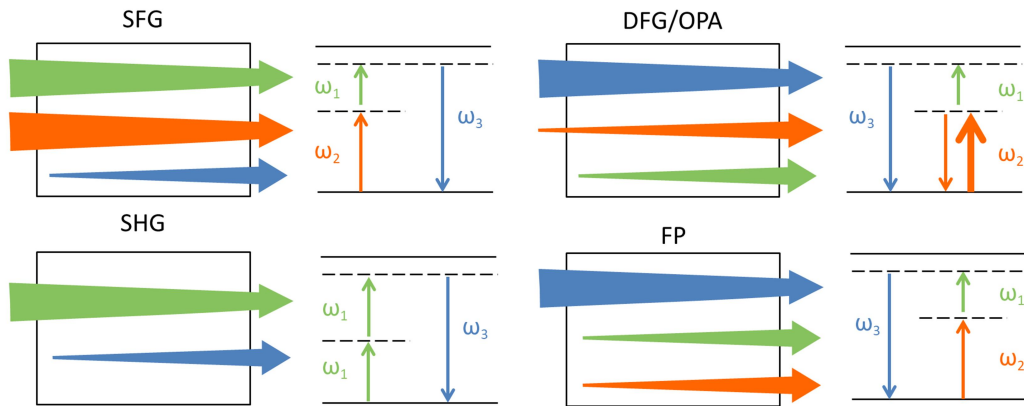


Figure 1-1. Three-wave mixing interactions. Left: waves amplitudes in a nonlinear medium. Right: virtual transitions, solid (dashed) lines corresponding to real (virtual) energy levels.

Second-harmonic generation

We will examine here the simple case of second harmonic generation to illustrate fundamental concepts of three-wave mixing. In the case of SHG, (1.6) reduces to

$$\frac{dE_\omega}{dz} = -i \frac{\omega d_{\text{eff}}}{n_\omega c} E_\omega^* E_{2\omega} e^{-i\Delta k z} \quad (1.8a)$$

$$\frac{dE_{2\omega}}{dz} = -i \frac{\omega d_{\text{eff}}}{n_{2\omega} c} E_\omega^2 e^{i\Delta k z} \quad (1.8b)$$

A common approximation is to assume *non-depletion of the pump*: the efficiency of frequency conversion is small enough for the pump power loss to be negligible. In this thesis, such assumption is largely justified and it will be made unless otherwise specified. $E_{2\omega}$ can then be set constant in (1.8), from which we deduce $E_\omega(z)$. The generated wave power is given by $P_{2\omega} = A I = A (1/2 \varepsilon_0 c n |E_{2\omega}|^2)$ where A is the field area. $P_{2\omega}$ turns out to be proportional to the square of P_ω , which allows us to define the conversion efficiency η_{SHG} and normalized conversion efficiency η_{norm}^0 as [64]

$$\eta_{SHG} = \frac{P_{2\omega}}{P_\omega^2} = \eta_{norm}^0 L^2 \left[\frac{\sin(\Delta k L/2)}{\Delta k L/2} \right]^2 \quad [W^{-1}] \quad (1.9a)$$

$$\eta_{norm}^0 = \frac{8\pi^2 d_{\text{eff}}^2}{\varepsilon_0 n_\omega^2 n_{2\omega} c \lambda_\omega^2 A} \quad [W^{-1} cm^{-2}] \quad (1.9b)$$

Since the normalized conversion efficiency does not depend on L , it is a convenient figure to compare SHG in different crystals.

From this simple description, we can observe the following features, which also hold for other types of $\chi^{(2)}$ processes:

- Generated power grows quadratically with distance and nonlinearity at phase matching.
- If the phase mismatch is not null, we can define the *coherence length* $L_c = \pi/\Delta k$. The generated field builds up during a length L_c , then decreases between L_c and $2L_c$. This variation is periodic, with the amplitude and period of energy exchange depending on L_c , and it arises from the interference between the generated and pump fields: if $\Delta k \neq 0$, the generated wave becomes more and more dephased with respect to the pump as it propagates, until it is π shifted at L_c , where the direction of energy transfer is inverted. This is shown in [figure 1-2](#) for several values of L_c .
- At fixed length, if $\Delta k \neq 0$, the conversion efficiency is affected by a rapidly decreasing function of $\Delta k L$. This is represented in [figure 1-3](#).

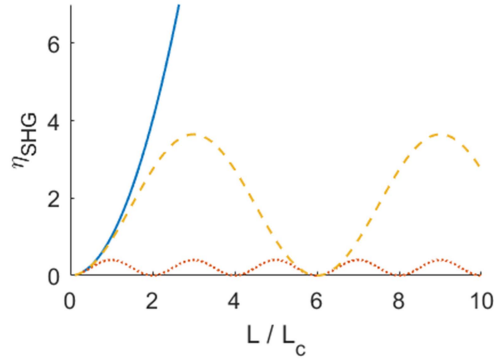


Figure 1-2. SHG conversion efficiency for different values of coherence length. Solid blue line: $L_c = \infty$ ($\Delta k = 0$), dashed yellow line: $L_c = 3$, red dot-dashed line: $L_c = 1$.

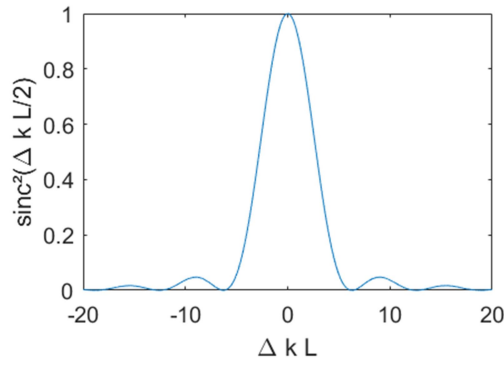


Figure 1-3. Normalized SHG conversion efficiency vs. normalized phase mismatch.

Optical parametric amplification

In the case of OPA, we make once more the undepleted-pump assumption. Then E_s is constant in (1.6) and its solution becomes [64]

$$E_s(z) = \left\{ E_s(0) \left[\cosh(gz) + \frac{i\Delta k}{2g} \sinh(gz) \right] + \frac{K_s}{g} E_i^*(0) \sinh(gz) \right\} e^{-i\Delta kz/2} \quad (1.10a)$$

$$E_i(z) = \left\{ E_i(0) \left[\cosh(gz) + \frac{i\Delta k}{2g} \sinh(gz) \right] + \frac{K_i}{g} E_s^*(0) \sinh(gz) \right\} e^{-i\Delta kz/2} \quad (1.10b)$$

where $K_{i,s}$ and g are defined by

$$K_j = -i \frac{\omega_j d_{\text{eff}}}{n_j c} E_p, \quad j = s, i \quad [cm^{-1}] \quad (1.11a)$$

$$g^2 = g_0^2 - \left(\frac{\Delta k}{2} \right)^2 \quad [cm^{-2}] \quad (1.11b)$$

$$g_0 = \sqrt{K_s K_i^*} = \sqrt{\frac{8\pi^2 d_{\text{eff}}^2}{\epsilon_0 c n_s n_i n_p \lambda_s \lambda_i} \frac{P_p}{A}} \quad [cm^{-1}] \quad (1.11c)$$

We will call g the *gain coefficient* and $P_{s,i}/P_{s,i}(0)$ the *gain G* . Note that the gain coefficient g_0 is higher at degeneracy and that in this case we can write $g = (\eta_{\text{norm}}^0 P_p)^{1/2}$, where η_{norm}^0 is the normalized conversion efficiency of SHG. In the long range, still in the undepleted pump approximation, the gain is exponential in the case of phase-matching. In the case where signal and idler are indiscernible and of same amplitude at $z = 0$, still assuming phase-matching, $G = (\cosh^2(gz) + \sinh^2(gz))$. Taking the *weak gain approximation* $gL \ll 1$ (verified in this thesis), the gain in this particular case takes the form $G \sim (1 + 2g^2 z^2)$.

Nonlinear optics in waveguides

Effective area

Hereafter, we will consider eigenmodes propagating in waveguides. The electric field of the m^{th} eigenmode in a waveguide is given by

$$\vec{E}_m(x, y, z) = \phi_m(x, y) \varepsilon(z) \vec{e}_m e^{-i\beta_m z} \quad (1.12)$$

where ϕ_m [m^{-1}] is the spatial distribution of the electric field in the transverse plane, ε [V] is the slowly varying part of the electric field in the direction of propagation, \vec{e}_m is the direction of polarization and β_m is the propagation constant. The wave equation (1.3) can be solved similarly to the case of plane waves [65], with a few substitutions in the results. Material indices are replaced by modal effective indices. Wave vectors k_i are replaced by propagation constants $\beta_i = 2\pi n_i / \lambda_{0i}$, where λ_{0i} is the wavelength in vacuum. The shift from plane waves to eigenmodes of various transverse profiles makes necessary the use of the *nonlinear overlap integral Γ* , defined as

$$\Gamma = \int \int d_{\text{eff}}(x, y) \phi_1(x, y) \phi_2(x, y) \phi_2(x, y) dx dy \quad [V^{-1}] \quad (1.13)$$

In the case of SHG and OPA presented earlier, the conversion efficiency and the gain coefficient become:

For SHG:

$$\eta_{norm}^0 = \frac{8\pi^2 |\Gamma|^2}{\epsilon_0 c (n_\omega^{\text{eff}})^2 n_{2\omega}^{\text{eff}} \lambda_\omega^2} \quad [W^{-1} cm^{-2}] \quad (1.14)$$

For OPA:

$$g_0 = \sqrt{\frac{8\pi^2 |\Gamma|^2}{\epsilon_0 c n_s^{\text{eff}} n_i^{\text{eff}} n_p^{\text{eff}} \lambda_s \lambda_i}} P_p \quad [cm^{-1}] \quad (1.15)$$

Other definitions stay identical to the plane-wave case.

Γ expresses the overall overlap between the interacting modes and the effective nonlinearity, and its maximization is crucial for the design of efficient nonlinear devices: the effective nonlinearity should be highest where all the three fields are most confined, and nonlinear processes are more efficient between modes of same order.

SHG in the presence of losses

Waveguides offer strong confinement at the wavelength scale, which gives rise to high optical intensities and more efficient nonlinear interactions. However, they can introduce non-negligible optical losses due to surface scattering or absorption, all the more important as the electric field explores the core/cladding interface in a small-section waveguide. Of course they come along with usual absorption, two-photon absorption and free carrier absorption (FCA), which occur also in bulk optics. We will describe SHG and OPA for modes propagating in lossy waveguides.

In the presence of linear losses, the coupled equations of SHG become

$$\frac{d\varepsilon_\omega}{dz} = -i \frac{\omega}{n_\omega c} \Gamma \varepsilon_{2\omega} \varepsilon_\omega^* e^{-ik\Delta\beta z} - \frac{\alpha_\omega}{2} \varepsilon_\omega \quad (1.16a)$$

$$\frac{d\varepsilon_{2\omega}}{dz} = -i \frac{\omega}{n_{2\omega} c} \Gamma \varepsilon_\omega^2 e^{-ik\Delta\beta z} - \frac{\alpha_{2\omega}}{2} \varepsilon_{2\omega} \quad (1.16b)$$

where α_ω and $\alpha_{2\omega}$ [m^{-1}] are the power loss coefficients at frequencies ω and 2ω , and ε is the slowly varying part of the electric field of (1.12).

We make again the assumption of undepleted pump, which here means that the pump losses due to the nonlinear interaction are negligible compared to other losses. The pump amplitude along propagation is then simply given by an exponential variation:

$$\varepsilon_\omega(z) = \varepsilon_\omega(0)e^{-\alpha_\omega z/2} \quad (1.17)$$

The solution of (1.16) results in [66]:

$$\eta_{SHG} = \eta_{SHG}^0 L^2 e^{-(\alpha_\omega + \alpha_{2\omega}/2)L} \frac{\sin^2(\Delta\beta L/2) + \sinh^2[(\alpha_\omega - \alpha_{2\omega}/2)L/2]}{(\Delta\beta L/2)^2 + [(\alpha_\omega - \alpha_{2\omega}/2)L/2]^2} \quad (1.18)$$

Losses have a double impact: they lower the conversion efficiency and relax the phase-matching condition. This is illustrated in figure 1-4, showing the normalized conversion efficiency as a function of phase mismatch for various values of $\alpha_{2\omega}$. As losses increase, the relative weight of the *sinc* function decreases and the full width at half maximum (FWHM) increases.

Figure 1-5 shows the conversion efficiency as a function of waveguide length for different values of α_ω and $\alpha_{2\omega}$, in the case of perfect phase matching. When one field experiences losses, the conversion efficiency reaches a limit value and when both fields do, an optimal length appears.

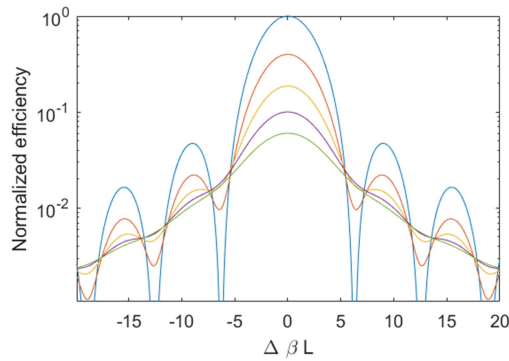


Figure 1-4. Normalized SHG conversion efficiency, $L=1 \text{ cm}^{-1}$, for $\alpha_\omega = 0$ and $\alpha_{2\omega} = 0, 1, 2, 3$ and 4 cm^{-1} from top to bottom.

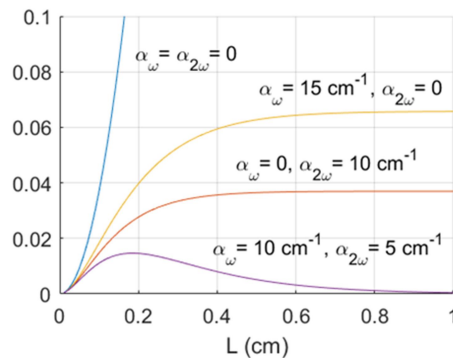


Figure 1-5. SHG conversion efficiency as a function of propagation length, for different levels of losses.

OPA in the presence of losses

Let us present the solution for OPA in lossy waveguides in the case of perfect phase-matching only. In the approximation of undepleted pump, the coupled equations become

$$\frac{d\varepsilon_s}{dz} = -i \frac{\omega_s}{n_s c} \Gamma \varepsilon_i^* \varepsilon_p(0) e^{-\alpha_p z/2} - \frac{\alpha_s}{2} \varepsilon_s \quad (1.19a)$$

$$\frac{d\varepsilon_i}{dz} = -i \frac{\omega_i}{n_i c} \Gamma \varepsilon_s^* \varepsilon_p(0) e^{-\alpha_p z/2} - \frac{\alpha_i}{2} \varepsilon_i \quad (1.19b)$$

$$\varepsilon_p(z) = \varepsilon_p(0) e^{-\alpha_p z/2} \quad (1.20)$$

The solution to this system is given by [67]

$$\varepsilon_s(z) = \left\{ \varepsilon_s(0) \cosh(G(z)) + \frac{K_s}{g_0} \varepsilon_i^*(0) \sinh(G(z)) \right\} e^{-\alpha_{si} z/2} \quad (1.21a)$$

$$\varepsilon_i(z) = \left\{ \varepsilon_i(0) \cosh(G(z)) + \frac{K_i}{g_0} \varepsilon_s^*(0) \sinh(G(z)) \right\} e^{-\alpha_{si} z/2} \quad (1.21b)$$

where α_{si} is the value of propagation losses at signal and idler wavelength (they are supposed equal) and $G(z)$ is a gain function depending on the position:

$$G(z) = g_0 \frac{1 - e^{-\alpha_p z/2}}{\alpha_p/2} \quad (1.22)$$

These equations are extremely similar to the case of OPA in a lossless medium (1.10), with a few differences:

- The gain coefficient g_0 is modulated by a gain function depending on the position. At fixed position L , g_0 decreases by a factor depending on pump losses only.
- The general form of fields amplitudes is similar to (1.10), but is additionally affected by an exponential decrease depending on the signal/idler loss coefficient.

Note that while the authors of [67] claim to work in the low-loss approximation, the only limitation set on losses is that they should be low enough to satisfy the approximation of slowly varying envelope. This is largely verified for the typical loss values in this thesis.

Furthermore, (1.22) and (1.23) are valid solutions of (1.20) and (1.21) regardless of the sign of α_p : they hold in the case of pump amplification as well as absorption.

OPA in the presence of gain

We choose to show the effect of pump gain as well as loss because this thesis is focused on the study of a laser-OPO. In this device, laser and OPO cavity are one and the same, and the OPO pump is provided by the laser field. In a laser at threshold, the field experiences a spatial variation that compensates for mirror losses (see [figure 1-10](#)):

$$Re^{\gamma L} = 1 \quad (1.23)$$

where we define γ as a “gain” or spatial variation. (Note that it is not the modal gain at threshold, which must equal the sum of mirror and propagation losses). In a laser of 1 mm with uncoated facets, R is typically in the range of 0.33 for the fundamental mode so γ is approximately 11 cm^{-1} . Lasers / OPOs presented here have higher pump reflectivities ($R = 0.67$), so this effect is less pronounced ($\gamma = 4 \text{ cm}^{-1}$ to 1.3 cm^{-1} for lasers of 1 to 3 mm).

[Figure 1-6](#) shows the effect of both signal/idler losses and pump gain/losses on the OPA power at degeneracy ($\omega_s = \omega_i$), for parameters in the typical range of the devices presented in this thesis. As expected, signal/idler variation goes from quadratic amplification to exponential decrease as the signal/idler losses increase. Pump gain can compensate for signal/idler losses (dash-dotted red curve), in which case longer waveguides are advantageous, but this effect is small and limited by the weak nonlinear gain set here.

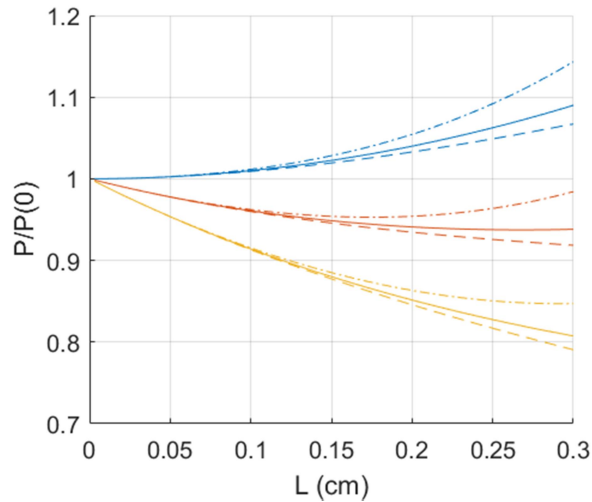


Figure 1-6. OPA gain vs. L , for $g_0 = 1 \text{ cm}^{-1}$ and $\alpha_s = \alpha_i = 0, 1, 2 \text{ cm}^{-1}$ (blue, red, yellow). Solid line: no pump variation; dashes: $\alpha_p = 2 \text{ cm}^{-1}$; dashes-dots: $\gamma_p = 3 \text{ cm}^{-1}$.

OPOs

When a nonlinear medium is placed inside a cavity, a threshold occurs for the generated field if the nonlinear gain overcomes losses. This is analogous to the laser threshold observed when a gain medium is placed inside a resonant cavity. The ensemble of nonlinear gain medium and cavity is an *OPO*. Unlike lasers, OPOs do not rely on the transitions between energy eigenlevels of valence electrons in matter. The energy levels involved are virtual, and can be controlled with external settings like temperature or crystal inclination. As a consequence, frequency output is tunable over a large wavelength range. OPOs today provide reliable sources of coherent, monochromatic light with much larger tunability than lasers.

One or several fields may be set in resonance in an OPO. OPOs where either the idler or the signal is reflected is usually called singly-resonant (SROPOs); those where both signal and idler are reflected are called doubly-resonant OPOs (DROPOs), and those where all three fields are resonating, triply-resonant OPOs (TROPOs). (Less common systems include cavities where signal and pump are resonating. For clarity they are usually called pump-signal OPOs instead of DROPOs). Increasing the number of resonating fields lowers the threshold power but degrades spectral stability.

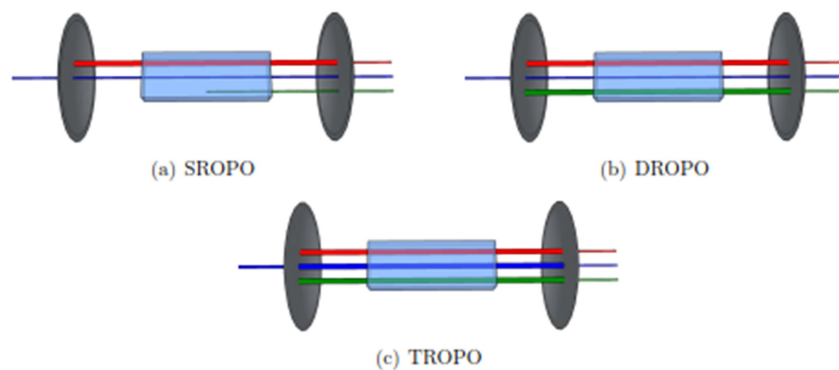


Figure 1-7. Common OPO configurations. Pump, signal and idler are represented in blue, red and green, respectively. Figure taken from [68]

The core of this PhD thesis deals with a laser diode – OPO in which laser and OPO cavities coincide and the laser beam acts a pump field. To lower the oscillation threshold, the design includes high-reflectivity mirrors at both signal and idler wavelengths. Since the pump obviously resonates to provide the laser effect, this device is a triply resonant oscillator. In the last chapter of this thesis, we also present the design of a DROPO that is vertically coupled with a monolithic but distinct laser

diode. Since no SROPOs are present in this thesis, their description is skipped but their characteristics can be inferred by setting $R_i = 0$ in the equations describing DROPO behavior.

Single pass DROPO

The threshold gain of a DROPO is found by setting the fields equal to themselves after a round trip in (1.22). Undepleted pump is assumed, unless otherwise specified.

Without propagation losses

Without propagation losses, in the case of weak gain, high reflectivity and perfect phase-matching, the gain at threshold is given by [69]

$$(g_0L)^2 = (1 - R_s)(1 - R_i) \quad (1.24)$$

The phase-matched pump threshold is then found by injecting (1.24) into (1.15). An approximate way to include (low) propagation losses in this estimation is to replace $R_{s,i}$ with $R_{s,i} \exp(-\alpha_{s,i}L)$.

$$P_p^{th,SP} = \frac{\epsilon_0 c n_s n_i n_p \lambda_s \lambda_i}{8\pi^2 \Gamma^2 L^2} (1 - R_s e^{-\alpha_s L})(1 - R_i e^{-\alpha_i L}) \quad (1.25)$$

With propagation losses

With propagation losses, the gain coefficient is replaced by a gain function that depends on the position (as we have seen for OPA), and the pump threshold in the phase-matched case becomes [69]:

$$P_p^{th,SP} = \frac{\epsilon_0 c n_s n_i n_p \lambda_s \lambda_i}{8\pi^2 \Gamma^2 L^2} \left[\frac{\alpha_p L/2}{1 - \exp(-\alpha_p L/2)} \ln \left(Q + \sqrt{Q^2 - 1} \right) \right]^2 \quad (1.26a)$$

$$Q = \frac{1 + R_s R_c \exp^{-2\alpha_{si}L}}{(R_s + R_c) \exp^{-\alpha_{si}L}} \quad (1.26b)$$

This is valid without approximation on losses, nonlinear gain or reflectivities.

The DROPO threshold as a function of resonator length is shown in [figure 1-8](#), for various values of propagation losses. Dashed lines correspond to the small losses approximation (1.24) and solid lines to the general case (1.25).

Using longer cavities has a clear interest in terms of threshold power: in the case of null propagation losses, switching from a 1 mm to 3 mm cavity decreases the pump threshold power by one order of magnitude. At higher loss levels, this effect

disappears as conversion efficiency is not increased by higher propagation lengths (see the discussion on [figure 1-5](#)). However, there is a compromise between threshold power and phase-matching control. Indeed, at phase matching the threshold power varies like $[\text{sinc}^2(\Delta kL/2)]^{-1}$ in the case of weak gain and high reflectivities. (Details of this calculation can be found in [\[68\]](#)). At higher waveguide lengths, the FWHM of this function gets narrower, reducing the phase-matching tolerance.

Spectral stability

Spectral stability of a DROPO is poorer than for a SROPO since both signal and idler are resonant modes of the cavity. This is represented in a modes diagram in [figure 1-9](#). In a SROPO, oscillation will occur on the mode closest to the phase-matching condition. In a DROPO, the modes have to satisfy both energy conservation and coincidence of signal / idler resonance. This condition can make operation unstable, as any mechanical or thermal disturbance may cause mode patterns to shift and oscillation to occur elsewhere. Furthermore, since the first pair of modes satisfying energy conservation is not necessarily phase-matched, the threshold suffers a penalty, varying like $[\text{sinc}^2(\Delta kL/2)]^{-1}$ as mentioned earlier.

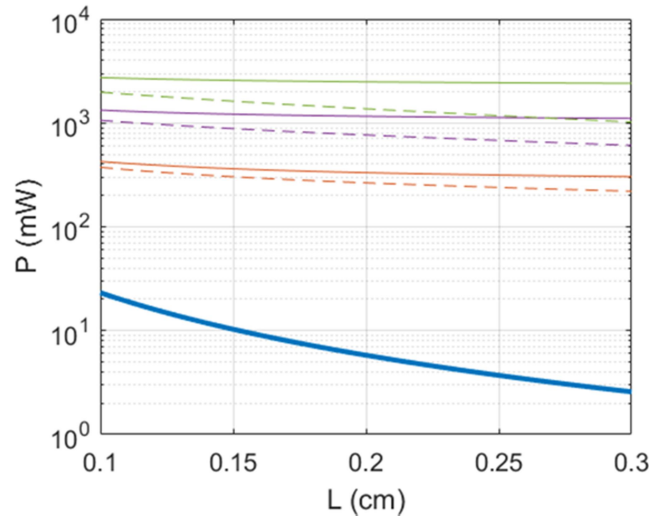


Figure 1-8. Pump threshold in a DROPO at degeneracy, with $\eta_0^{\text{SHG}} = 4 \text{ W}^{-1} \text{ cm}^{-2}$, $\alpha_p = 0$, and $R_{s,i} = 0.97$. Solid lines: exact solution (eq. 25), dashed lines: low-loss approximation (eq. 24). $\alpha_{s,i} = 0, 1, 2$ and 3 cm^{-1} (blue, red, purple, and green).

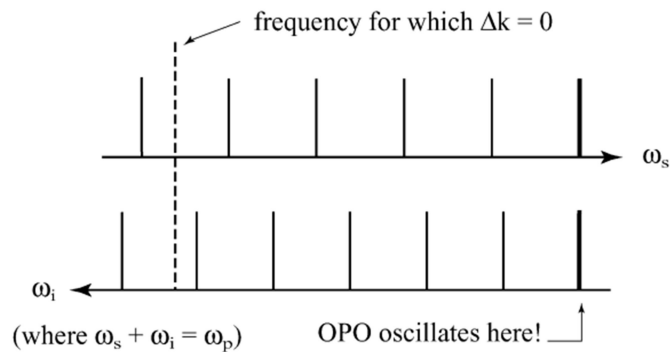


Figure 1-9. Mode diagram of a DROPO. Frequencies are drawn increasing in opposite directions, so that for any signal frequency the idler frequency directly under it is equal to $\omega_i = \omega_p - \omega_s$. Thus, any point on the axis represents a point where the energy conservation relation $\omega_s + \omega_i = \omega_p$ is satisfied, although only at points where signal and idler modes occur at the same horizontal point is the double-resonance condition satisfied. Figure taken from [64].

Double-pass DROPO

A double-pass (DP)-DROPO designates a system in which the pump is reflected once, thus providing parametric gain during both forward and backward propagation. DP-DROPOs are not dealt with in this thesis, but since they present analogies with TROPOs we will describe them quickly.

Figure 1-10 shows the spatial variation of pump and signal/idler fields in different types of OPOs. Note that the phase-matching condition is usually so stringent that the signal and idler only interact with the pump when they all travel in the same direction. For this reason, the signal/idler field in a SP-DROPO is only amplified as it travels in the forward direction. In a DP-DROPO, in each propagation direction, the signal/idler only interacts with the part of pump field propagating in the same direction, so with approximately half of the total pump power in the cavity. If the pump mirror has perfect reflectivity and induces no dephasing, this configuration is equivalent to unfolding the cavity and doubling the propagation length. In case of null losses, the pump threshold power is divided by 4 (since P_p^{th} varies like $1/L^2$).

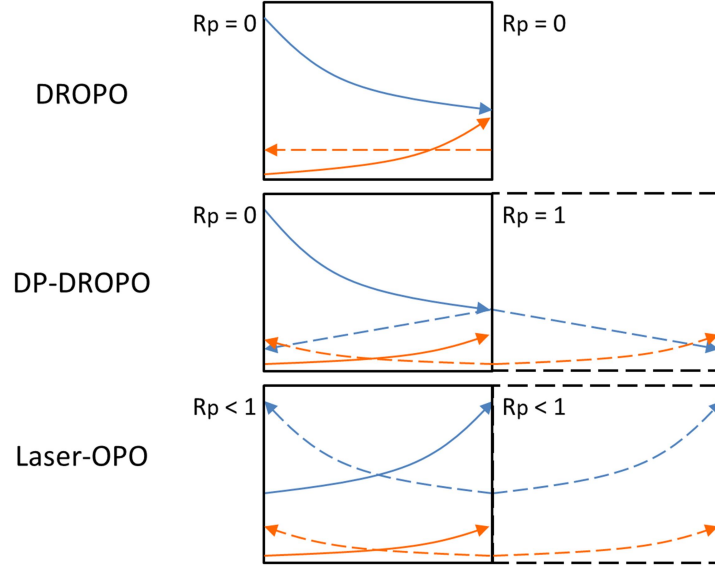


Figure 1-10. Variation of the pump and signal/idler fields in different types of OPOs. Blue: pump field, orange: signal/idler. Solid (dashed) lines: forward (backward)-propagating fields. The dashed rectangles and lines show unfolded cavities equivalent to reflections.

A detailed analysis of the pump threshold for arbitrary phase mismatch and mirror phase shift is given in [70]. We present here only the case of null linear losses, and refer the reader to [68] for a calculation of the threshold in the presence of parasitic losses. According to [70], the threshold power of a double-pass DROPO in the absence of linear losses and in the weak gain approximation is given by

$$P_p^{th,DP} = \frac{\epsilon_0 c n_p n_s n_i \lambda_s \lambda_i}{8\pi^2 \Gamma^2 L^2} \frac{(1 - R_s)(1 - R_i)}{1 + r^2 + 2r \cos(\theta_2)} \left[\text{sinc}^2 \left(\frac{\Delta k L}{2} \right) \right]^{-1} \quad (1.27a)$$

$$\theta_2 = \Delta k L - \Delta\varphi = \Delta k L - (\varphi_p - \varphi_s - \varphi_i) \quad (1.27b)$$

where r is the amplitude of complex reflectivity $r \exp(i\phi_p)$ for the pump and $\Delta\phi$ is the relative phase shift upon reflection. If $r = 0$, the denominator of (26) is equal to 1 and the threshold reduces to that of a single-pass DROPO. The ratio of single-pass to double-pass DROPO threshold as a function of phase mismatch is represented in figure 1-11. If the mirror does not introduce a phase shift, the behavior is similar to a single-pass DROPO: the threshold power is minimal for $\Delta k = 0$ and divided by 4 with respect to the single-pass case. However, if the mirror phase shift is non-null, it compensates for a phase mismatch during propagation. In that case, the minimum threshold power does not occur anymore for $\Delta k = 0$. The gain in terms of threshold

power is then less pronounced, but even in the worst case ($\Delta\phi = \pi$), the threshold power is divided by 2 with respect to the case of a single-pass oscillator.

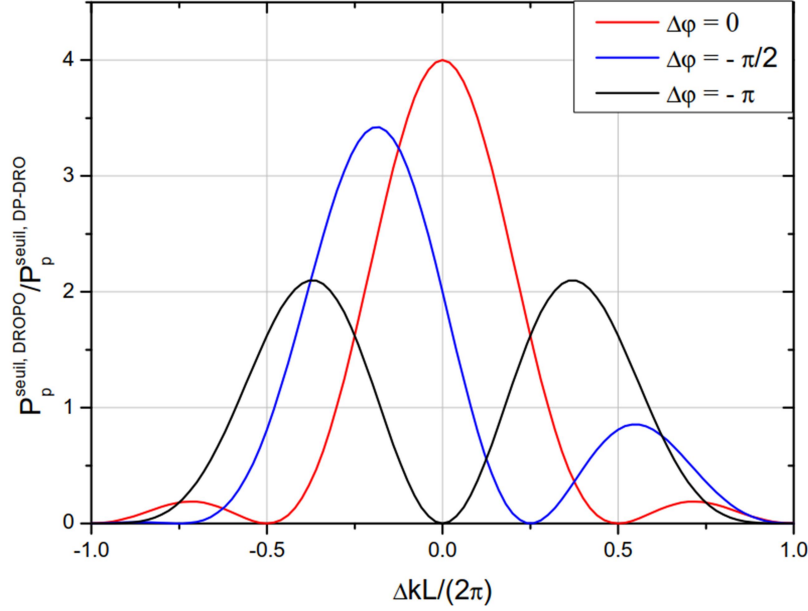


Figure 1-11. Ratio of single-pass to double-pass DROPO threshold as a function of phase mismatch. $\Delta\phi$ is the difference of phase shifts upon reflection. The amplitude of pump reflectivity is equal to 1. Figure taken from [68].

TROPO

Because of their instability, triply-resonating oscillators (TROPOs) are seldom implemented, and they are absent from most textbooks on nonlinear optics. To our knowledge, two analytical descriptions of TROPO have been published [71,72]. [72] considers an intracavity-OPO (IOPO). In this type of system, a SROPO or DROPO is placed inside a laser cavity. This presents the interest of harnessing the intense intracavity laser field, while keeping the two cavities separate and thus more easily stabilized. This work is transposed to the design of a laser diode – OPO in [60], which remains a proposition of principle to our knowledge. [71] considers a single triply resonant cavity pumped by an external laser. Their results are verified in an experimental work [73] where the authors achieved an ultra-low threshold in the mW range. In both articles, losses are neglected. We will present mostly the work of [71] since it treats a more general case (arbitrary phase mismatch and mirror phase shift).

Pump power threshold for null mismatch and phase shift

We firstly present the case of null mirror phase shift at phase matching. In this case, both articles give the same value for the pump threshold inside the cavity. It is just the threshold of a DP-DROPO:

$$P_p^{th} = \frac{1}{4} \frac{\epsilon_0 c n_s n_i n_p \lambda_s \lambda_i}{8\pi^2 \Gamma^2 L^2} (1 - R_s e^{-\alpha_s L}) (1 - R_i e^{-\alpha_i L}) \quad (1.28)$$

This is the traditional result for a DP-DROPO in the low-loss approximation (1.25). Here $P_p = P_p(0^+)$ designates the incoming pump power inside the cavity. Thus with respect to a DROPO, the pump power threshold measured outside the cavity, $P_p(0)$, is just lowered by the enhancement factor of the cavity. As we shall see later, dephasing and imperfect overlap of the modes frequency combs increase this minimum value of the pump threshold.

Effect of pump mode pattern

The equality between threshold of a TROPO and a DROPO is far from intuitive. Indeed, the pump is a plane wave in a DROPO and a standing wave in a TROPO, so stating this equality is equivalent to claiming that the pump mode pattern has no effect on the threshold, even though the spatial distribution of power is not the same in both cases. Nonetheless, to convince himself of this equivalence, the reader can remember that a standing wave is produced by the superposition of travelling waves in opposite directions, and that the signal/idler only interacts with the pump when it is travelling in the same direction. As a result, the counter-propagating part of the pump has no interaction with the signal / idler and the minimal pump power threshold is the same as in the DROPO case. However, making the pump resonate in the cavity is not without consequences for requirements on the fields phase.

Both [72] and [71] consider a single longitudinal cavity mode, whereas Fabry-Perot lasers typically exhibit a family of longitudinal modes in the absence of a DFB or other control scheme. The consequence of using a laser with several longitudinal modes would likely be an increase of threshold if only part of the power is inside the mode satisfying oscillation conditions.

Relevance of the mean field approximation (low losses)

The derived calculation of the pump threshold ignores the losses and assumes $R \approx 1$. The implications of this approximation are different for pump losses and signal / idler losses. Pump losses have an impact on the nonlinear gain, while s/i losses

impact on the total loss level. We examine the relevance of these assumptions and propose phenomenological corrections.

Relevance of mean field approximation 1): effect of pump gain/losses

[72] and [71] assume either a small or no variation of the pump field. However, as said earlier, this is generally not the case in a laser diode. We will analyze the impact of this variation on the power threshold, starting from the results derived in 1.2.4.

A rough analogy can be made between a laser-OPO and a symmetric SP-DROPO, where the pump undergoes amplification instead of absorption. The threshold power can be expected to be divided approximately by 4 since nonlinear gain occurs in both propagation directions.

We remind the reader that we are interested in the case of a laser at threshold, where the field experiences a spatial variation that compensates for mirror losses (1.23).

There is to our knowledge no analytical calculation of a TROPO threshold, or even double-pass DROPO threshold in the case of arbitrarily high losses or gain. For this reason, we implemented a RK (Runge-Kutta) solver in order to compare the variation of threshold vs. spatial variation γ to the case of a single-pass DROPO. The TROPO is treated like an unfolded DROPO cavity (based on the justification given earlier) and we are not considering any dephasing effect (phase mismatch and mirror phase shift are null). Signal and idler have identical frequencies and incoming power. This is shown in figures 1-12 and 1-13. Figure 1-12 shows the variation of pump (red) and signal/idler fields (blue) at threshold in a SP-DROPO where the pump field undergoes an amplification of 7.4 cm^{-1} to compensate for facet reflectivities of 33%. Figure 1-13 shows the fields variation at threshold in an unfolded cavity equivalent to a laser-OPO. The pump (laser) field still undergoes an amplification of 7.4 cm^{-1} corresponding to facet reflectivities of 33%. The incoming pump power in fig. 13 is one fourth of what it is in fig. 12. This is verified for facet reflectivities of 10%, 30%, 60% and 90%.

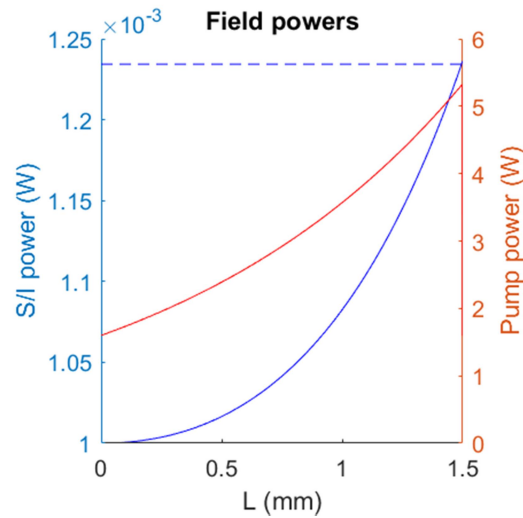


Figure 1-12. Simulation of the fields propagating in a single-pass DROPO. The input pump power is 1.6 W. The blue dotted line corresponds to the level $1/R_s^2$ necessary for s/i to reach threshold (here, $R_s = R_i = 0.8$).

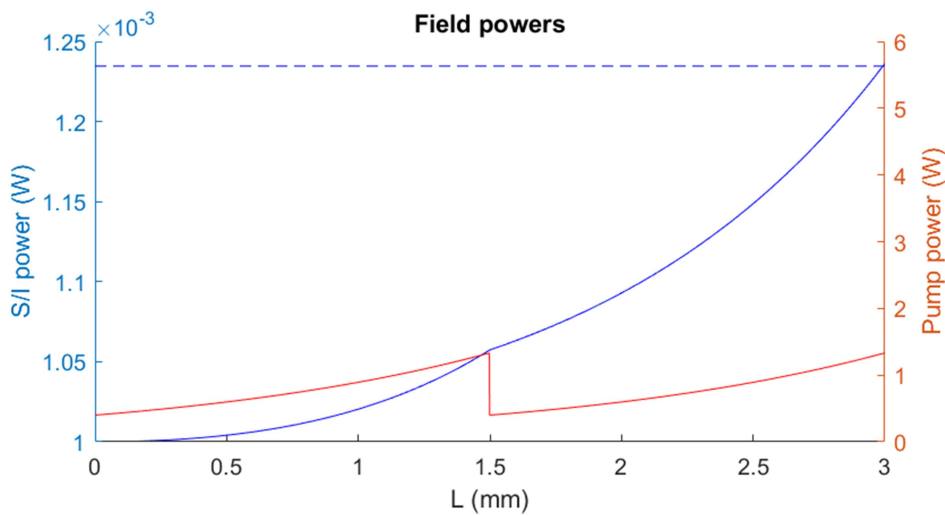


Figure 1-13. Simulation of the fields propagating in a laser-OPO, treated like an unfolded double-pass DROPO with no mirror phase shift. The incoming pump power is $1.6 / 4 = 0.4$ W. The blue dotted line corresponds to the level $1/R_s^2$ necessary for signal/idler to reach threshold (here, $R_s = R_i = 0.8$).

In the case of a laser – OPO, the quantity of interest is not the incoming pump power but the total power in the cavity. Total power in the cavity vs. incoming power is simply given by integrating the pump field along the direction of propagation. Furthermore, we have shown that the TROPO threshold power (incoming) is one-fourth that of a single-pass DROPO. This allows us to express the

TROPO threshold power (total power inside the cavity) in terms of the SP-DROPO threshold power (incoming), which is already given in eq. 25:

$$\begin{aligned} \frac{P_{TROPO}^{th,total}}{P_{SP-DROPO}^{th,inc.}} &= \frac{P_{TROPO}^{th,total}}{P_{TROPO}^{th,inc.}} \frac{P_{TROPO}^{th,inc.}}{P_{SP-DROPO}^{th,inc.}} \\ &= \frac{2(e^{\gamma_p L} - 1)}{\gamma_p L} \frac{1}{4} \end{aligned} \quad (1.29)$$

where γ designates the pump spatial amplification.

However, the threshold power of a SP-DROPO depends itself on the value of pump gain/losses (eq. 25). Taking these into account, the ratio of TROPO threshold to minimal threshold (no pump gain or losses) is:

$$\frac{P_{TROPO}^{th,total}}{P_{TROPO}^{th,total}|_{\gamma_p L=0}} = \frac{e^{\gamma_p L} - 1}{\gamma_p L} \left(\frac{\gamma_p L/2}{e^{\gamma_p L/2} - 1} \right)^2 \quad (1.30)$$

This is represented in [figure 1-14](#). At the levels of reflectivities presented in this thesis, $\gamma L \approx 0.4$, so the correction on the total pump power quite small.

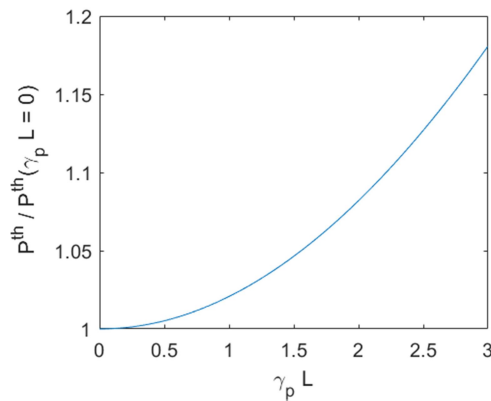


Figure 1-14. Variation of TROPO threshold power (total power inside the cavity) with pump amplification.

Relevance of mean field approximation 2): effect of signal/idler losses

As we have seen earlier, the threshold power in [\[71,72\]](#) corresponds to the weak losses approximation, which tends to underestimate the threshold (see [figure 1-8](#)). A more accurate estimation would be given by (1.25), corrected by the factor derived above (1.30).

Effect of phase mismatch and mirror phase shift

Taking into account the effects of phase mismatch and mirror phase shift, the threshold becomes [71]

$$\frac{P_{TROPO}^{th,total}}{P_{TROPO}^{th,total}|_{\Delta kL=\delta'=0}} = \frac{(\Delta kL/2)^2}{\sin^2(\Delta kL/2) \cos^2(\Delta kL/2 - \theta'/2)} \quad (1.31)$$

where θ' is a combination of mirror phase shifts: $\delta' = \delta_s + \delta_i - \delta_p$.

Fig. 15 shows the normalized threshold power as a function of phase mismatch, for various values of the mirror phase shift parameter. Similarly to the case of a DP-DROPO, a mirror phase shift causes the system to operate for Δk different from 0. If all fields are resonant, the system operates at the curves minimum. In the worst case of mirror phase shift, the threshold power is then increased by a factor of 5 only. In case of imperfect resonance, the system operates on the curves away from the minimum and the threshold is increased further.

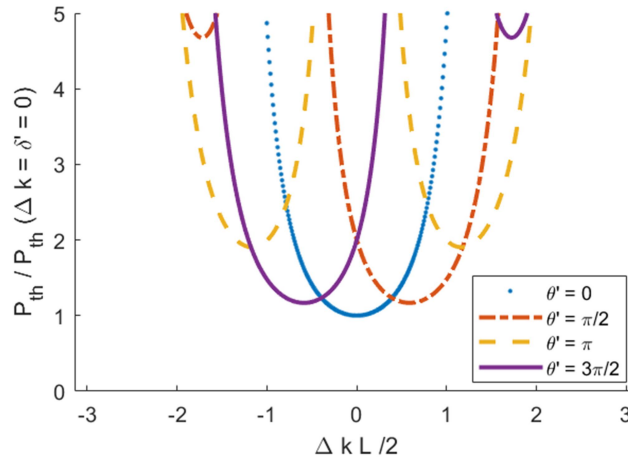


Figure 1-15. Variation of the pump power threshold as a function of phase-matching coefficient $\Delta kL/2$ for different values of the mirror phase-shift parameter θ' .

In experiments on triply resonant cavities, one does not control dephasing upon reflection and pays a fixed price on pump power. Authors in [73] find a factor of 0.4 between measured and predicted thresholds, which they ascribe to imperfect phase matching. In a semiconductor TROPO (or laser diode-OPO), no external setting exists to set the cavity length, which makes an *in situ* control of mirrors phase shifts all the more critical. One way to implement this could be the introduction of controlled Bragg mirrors with piezoelectric elements.

Phase-matching strategies in GaAs

As we have seen earlier, frequency-mixing processes require photon energy and momentum conservation:

$$\omega_1 + \omega_2 = \omega_3 \quad (1.32a)$$

$$\vec{k}_1 + \vec{k}_2 = \vec{k}_3 \quad (1.32b)$$

where the wave vectors magnitudes are $k_i = 2\pi / \lambda_i = 2\pi n_i / \lambda_0$. If the three waves propagate in the same direction, the condition on conservation of momentum becomes

$$n_1 \omega_1 + n_2 \omega_2 = n_3 \omega_3 \quad (1.33)$$

For example, in the case of SHG with signal and idler of same polarization, this imposes $n(\omega) = n(2\omega)$.

Usually the two conditions of (1.32) cannot be satisfied simultaneously because of material dispersion. As a consequence, a number of strategies have been developed to satisfy phase-matching in nonlinear materials.

Two types of phase-matching are commonly defined:

- Type I phase-matching: the two waves of lower frequency have the same polarization
- Type II phase-matching: the wave of higher frequency (ω_3) and one wave of lower frequency have the same polarization, and the other one is cross-polarized.

This is represented in [figure 1-16](#). We designate the crystal indices with a generic tag “ n_1, n_2 ”. In a uniaxial negative crystal, n_1 would be the ordinary index and n_2 the extraordinary; in the case of modal engineering, n_1 and n_2 would refer to the indices of different modes of the waveguide.

Note that type I phase-matching requires a smaller index difference at identical dispersion and frequency choice.

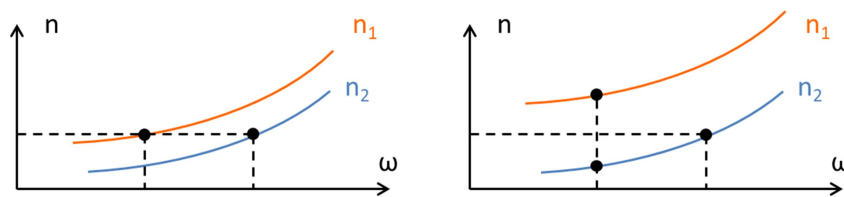


Figure 1-16. Types of phase-matching. Left: type I, right: type II.

Phase-matching schemes can generally be classified among exact or quasi phase-matching (QPM) types. In exact phase-matching, material or effective indices are engineered to achieve precisely the index mismatch satisfying (1.33). Phase mismatch is null, and the coherence length is infinite. On the contrary, in quasi phase-matching, phase mismatch is not null. The waves go in and out of phase as they propagate and the material symmetry is modified to compensate for this effect. This technique requires no particular engineering of the material index.

Form birefringence

To achieve phase-matching, it is common to use birefringent nonlinear materials, whose refractive index depends on the wave polarization direction. Unfortunately, GaAs (as well as AlGaAs or InGaAsP) is a cubic crystal, which lacks birefringence.

However, form birefringence can be introduced in AlGaAs waveguides through the selective oxidation of layers of high Al content. The effect of this manipulation of the local indices is to enhance the geometric birefringence between TE and TM guided modes. Then type-I phase matching becomes possible between fundamental modes of a ridge waveguide. [Figure 1-17](#) shows the index and modes profile in such a structure and the phase-matching scheme employed. This technique has permitted the demonstration of an OPO threshold inside a GaAs/AlGaAs ridge waveguide in 2013 [\[53\]](#). It puts little constraint on the waveguide geometry, which allows the use of extremely narrow ridges, increasing the modes intensity and conversion efficiencies [\[74\]](#). The main limitation of this scheme to this day is due to the large propagation losses introduced by the oxidation step. Moreover, the pump must be polarized in the TM direction. This makes the integration of a frequency converter waveguide with a standard quantum well laser diode impossible, unless a polarization converter provides the transition between the two steps.

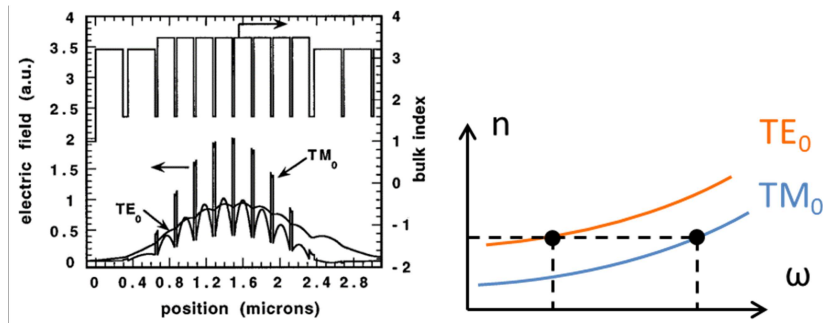


Figure 1-17. Left: Index and modes profile in form-birefringent AlGaAs waveguides (From [53]). Right: type of phase-matching employed.

Quasi-phase matching

In QPM, the material symmetry is inverted at a period equal to twice the coherence length. This is illustrated in figure 1-18. For a non-null phase mismatch, the direction of energy transfer would normally reverse periodically, preventing consistent energy buildup. Reversing the sign of nonlinearity inverses the direction of energy transfer in the regions where the generated fields would normally deplete. As a result, the final interaction is constructive. The generated fields power grow as $(2/\pi)^2 L^2$ (instead of L^2 for perfect phase-matching).

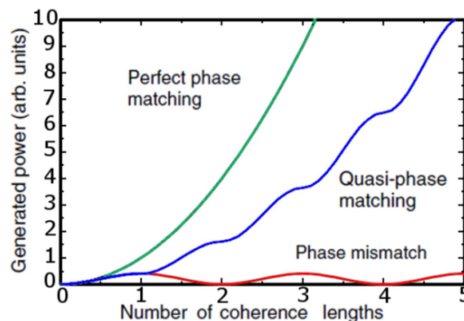


Figure 1-18. Generated power as a function of L/L_c for various phase matching schemes [75].

This scheme requires materials presenting a periodic inversion of the crystalline symmetry at a micrometric scale⁵. In practice, the first materials of this type were

⁵ A multiple of the coherence length can also be used, but the conversion efficiency decreases with the order of multiplicity.

ferroelectric crystals (LiNbO₃, KTP, LBO...) in which the periodicity is induced by the application of strong electric fields at periodic intervals, permanently inverting the orientation of the crystal.

GaAs substrates presenting this inversion are known as “orientation-patterned GaAs” or OP-GaAs. They can be fabricated by growing two layers of opposite orientations, introducing a micrometric pattern with lithography techniques, and resorting to an epitaxial regrowth on the resulting wafer (figure 1-19). The regrowth step is technologically heavy and introduces a limit on the maximal crystal height. Indeed, the domain walls tend to drift and become irregular during regrowth, which creates a limit to the maximal usable size; furthermore, apparition of defects at the interfaces is common. As a consequence, the main limitation of this technique in micrometric waveguides is currently the losses induced by interfaces defects. Bulk OP-GaAs has initially been used with high pump powers in macroscopic cavities, where it presents an advantage over ferroelectric crystals because of its important $\chi^{(2)}$ [44,76,77]. More recently, an OPO threshold has also been demonstrated in a micrometric OP-GaAs waveguide [47].

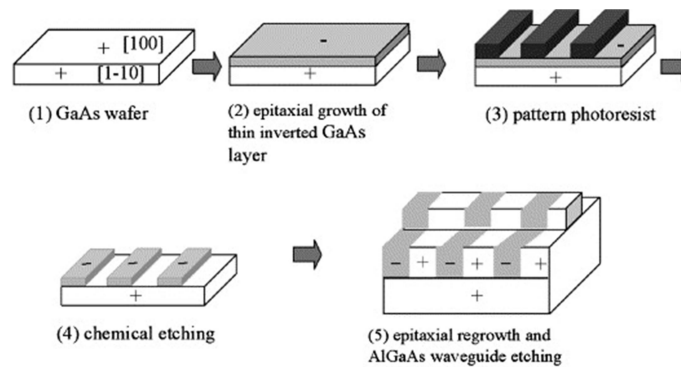


Figure 1-19. Fabrication process of orientation-patterned GaAs. Figure taken from [78]

Quantum well intermixing is also used to introduce a periodic modulation of the $\chi^{(2)}$. Intermixing designates the blending of quantum well and surrounding atoms (figure 1-20). It can be implemented by ion implantation or laser annealing among other techniques; these processes can be applied selectively, after masking part of the sample with lithography techniques. The usual effect is to increase the quantum well band gap, and it is commonly used to turn parts of a waveguide transparent at the quantum well wavelength. In nonlinear optics, QW intermixing has been used to periodically destroy the $\chi^{(2)}$ [79]. In that case, signal / idler power builds up during half of the total propagation length. While this method is less efficient and also introduces propagation losses, it is relatively easier to implement than

orientation-patterning, since it requires no epitaxial regrowth. The same technique has also been used to periodically modulate the $\chi^{(2)}$ through a local variation of the band gap [80].

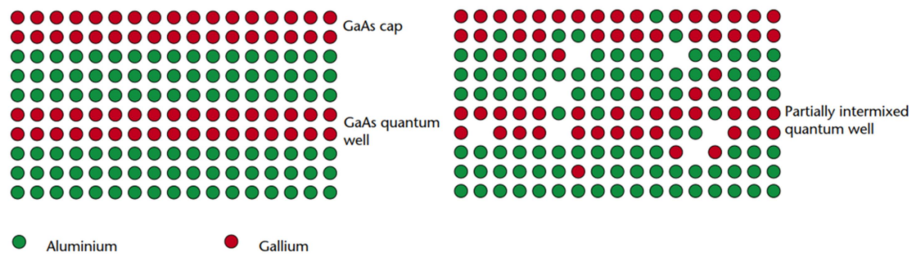


Figure 1-20. Quantum well before (left) and after (right) intermixing. Figure taken and adapted from [81]

More creative schemes exist to introduce a periodic inversion of the material in GaAs. In microdisks [82] and snake waveguides [83], this inversion arises naturally from the waveguide geometry (see figure 1-21). Finally, an elegant QPM scheme was proposed a few years ago, relying on two coupled parallel waveguides, in which light travels periodically from one to the other. However, no experimental demonstration of it exists to our knowledge [84].

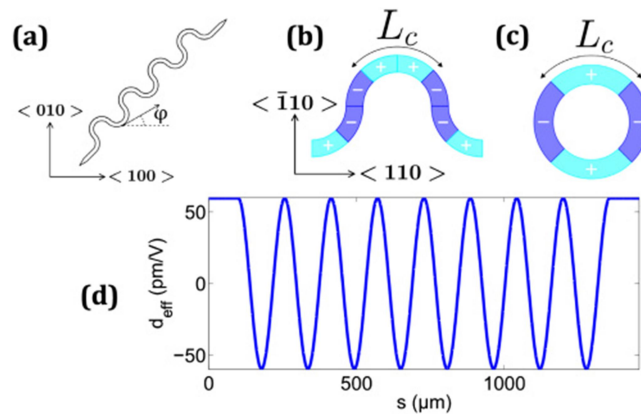


Figure 1-21. (a) General view of a snake waveguide, (b) Inversion domains and coherence length in a snake waveguide, (c) Same in a microdisk, (d) Effective nonlinear coefficient as a function of propagation length. Figure taken from [83]

Modal phase matching

Modal phase matching refers to the careful engineering of modes in a waveguide to achieve exact phase matching. Since the birefringence of standard semiconductor waveguides is usually too small to enable phase-matching, higher-order modes or different types of waveguides are used. Figure 1-22 shows an example of such a

waveguide, engineered for SHG from 1550 nm to 775 nm. The pump is guided by total internal reflection, mode, while the second harmonic is carried by a Bragg mode. This technique is extremely simple in terms of fabrication. Most of the complexity is related to the epitaxy, which is normally the best controlled step of fabrication⁶. Losses can be as low as 0.1 cm^{-1} in passive waveguides. The main drawback of this technique is the overlap of interacting modes, typically poorer than values achievable between fundamental modes in birefringent or QPM phase-matching.

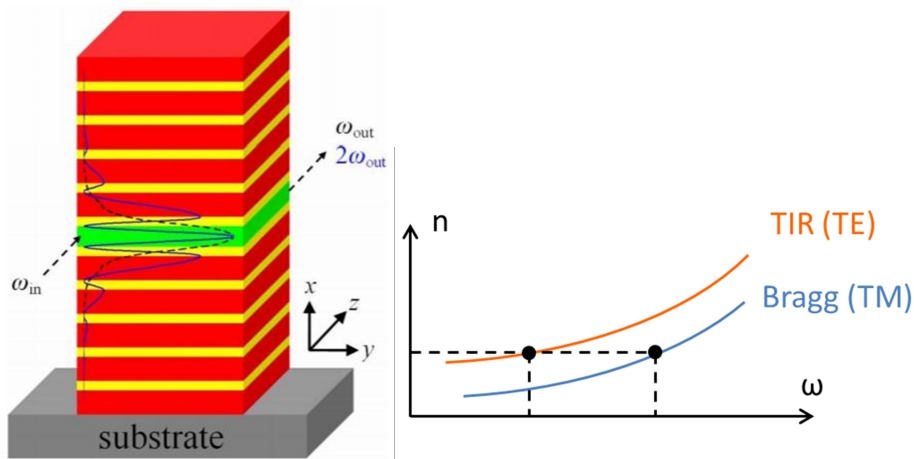


Figure 1-22. Left: intensity of the interacting modes in a waveguide engineered for SHG. Dashed line: pump (fundamental TIR mode), full line: second harmonic (Bragg mode).

Figure taken from [85]. Right: type of phase-matching employed.

⁶ At the state of the art, molecular beam epitaxy of AlGaAs offers a control of thickness down to the monolayer in quantum wells and down to 1% in thicker layers. In terms of compositions, the atomic fraction is controlled to 1% in $\text{Al}_{1-x}\text{Ga}_x\text{As}$.

2. QD and QW laser diodes

We give here an introduction to semiconductor laser diodes and explain the specificities of quantum dots (QD) and quantum well (QW) lasers. The first section provides a phenomenological description of lasers: we show what the quantities externally measurable in a typical setup are, and what makes an efficient laser. In section 2, we present the specificities of QW and QD lasers and derive their optical gain spectra. In section 3 we describe the selection rules for optical transitions.

Phenomenological description of lasers

Optical gain in a two-level system

We provide here an elementary description of the optical gain in a two-level system. In section 2, we will detail the origin of gain in confined semiconductor heterostructures.

Figure 2-1 shows the possible interactions of a photon with a 2-level system. If the latter is in an excited state, it can spontaneously relax and emit a photon at the energy $h\nu = E_2 - E_1$. The inverse process is absorption: the photon brings the system to its excited state. Finally, an incident photon can induce stimulated emission. The transition rates for these processes are given by the Einstein coefficients. Without going into details, we shall point out that the transition rates for absorption and stimulated emission are the same. As a consequence, the only way to achieve amplification in a medium is to first achieve *inversion of population*, that is bring more carriers in an excited state than in the ground state.

If inversion of population has been achieved in the medium, shining a light at the frequency $h\nu = E_2 - E_1$ creates a chain effect, as emitted photons cause further stimulated emission. Field power is then described by an exponential law: $P(z) = P(0) \exp(\gamma z)$, where γ is the *power gain coefficient* of the medium, usually expressed in cm^{-1} .

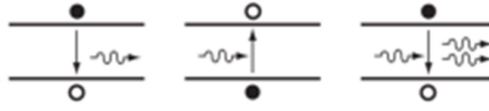


Figure 2-1. Possible interactions of a two-level system with a photon of resonant energy. Left: spontaneous emission, center: absorption, right: stimulated emission. Figure taken from [86]

Laser threshold condition

A laser requires a gain medium and a resonating cavity. Figure 2-2 shows the variation of a field injected at the entrance of a gain medium placed inside a cavity. Below threshold, the gain built during propagation is not important enough to compensate for mirror and propagation losses. At threshold, the field power is equal to itself after a round-trip in the cavity.

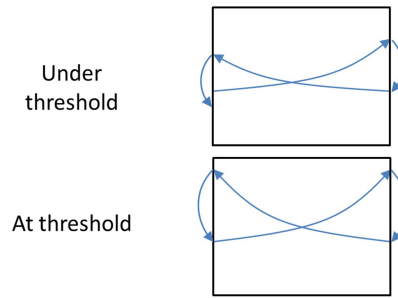


Figure 2-2. Variation of the amplitude of a field injected at the cavity entrance

Laser threshold is determined by the equality of complex electric field after a round-trip:

$$r_1 r_2 e^{2ikL} e^{(\gamma - \alpha_p)L} = 1 \quad (2.1)$$

where r_1, r_2 are the complex amplitudes of reflectivity for the electric field, γ is the power coefficient for optical gain, α_p is the power coefficient for propagation losses, k is the wave vector and L is the cavity length.

Taking the amplitude part of this equation yields:

$$\gamma = \alpha_p + \frac{1}{2L} \ln\left(\frac{1}{R_1 R_2}\right) = \alpha_p + \alpha_m \quad (2.2)$$

where we have defined the mirror losses α_m . This equation reflects the fact that *gain must equal total losses at laser threshold*. Above threshold, the gain cannot exceed

losses (or the power would grow exponentially until infinity, which is not physical) so the gain is clamped.

The phase part of (2.2) yields $2kL = 2p\pi$ (where p is an arbitrary integer). As a consequence, allowed mode frequencies in a linear cavity are spaced by the constant Free Spatial Ratio, or FSR:

$$\nu_p = p * FSR = p * \frac{c}{2nL} \quad (2.3)$$

The *confinement factor* indicates the fraction of field power present in a region of space. It's commonly defined in the plane perpendicular to the propagation axis:

$$\Gamma = \frac{\int_{x_1}^{x_2} \int_{y_1}^{y_2} |E(x, y)|^2 dx dy}{\int_{-\infty}^{\infty} \int_{-\infty}^{\infty} |E(x, y)|^2 dx dy} \quad (2.4)$$

The modal and material gain are linked by the relation

$$\gamma_{modal} = \Gamma \gamma_{material} \quad (2.5)$$

The laser threshold then becomes

$$\gamma_{mat} = \frac{1}{\Gamma} (\alpha_p + \alpha_m) \quad (2.6)$$

where γ_{mat} indicates the material gain.

The maximal gain of a typical quantum well vs. carrier density n_{2D} [cm^{-2}] is represented in [figure 2-3](#). The *transparency threshold* indicates the carrier density for which the gain is null and an incoming field is neither absorbed nor amplified by electron-hole transitions. At laser threshold, modal gain equals total losses. In a typical quantum well laser, the confinement factor is a few per cents (1 to 10%, depending on the number of wells) and the maximal material gain is in the range of $5\,000\text{ cm}^{-1}$. The available modal gain is then a few hundreds of cm^{-1} . The threshold indicated in [figure 2-3](#) corresponds to a confinement factor of 1% and total losses of 5 cm^{-1} .

If we make the assumption that the carrier density in the active area is constant, and if we ignore current leakage, at threshold the 3D carriers density is related to the injected current by [\[75\]](#)

$$J = \frac{q d n_{3D}}{t} \quad (2.7)$$

where q is the electron charge and d is the active area thickness. For a deep quantum well, carriers are efficiently trapped inside and d is the well thickness. t is the total recombination time given by $t^{-1} = (t_{rad}^{-1} + t_{nonrad}^{-1})$, where t_{rad} is the radiative recombination time and t_{nonrad} is related to nonradiative recombination processes. It is usually in the range of 3 ns for a conventional AlGaAs QW laser at around 300K.

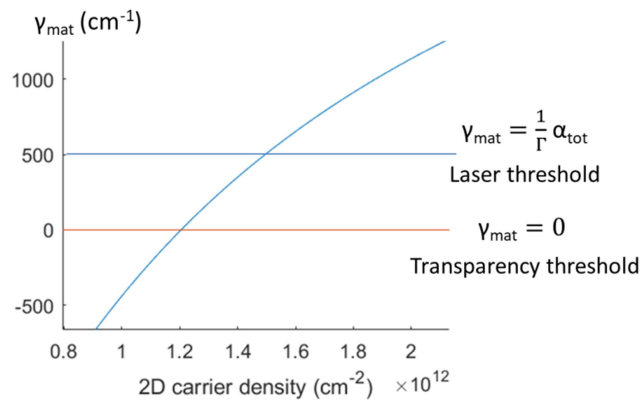


Figure 2-3. Maximal material gain in a GaAs QW vs 2D carrier density. Transparency and laser threshold

In quantum dot lasers, modal gain depends on the dot areal density and on the inhomogeneous broadening of their emission line. Precisely relating the two parameters is not always simple. While trends in dot density can be observed, measuring the exact density of a quantum-dot layer is experimentally complicated. Dots grown without capping layer for AFM or SEM measurements tend to mature⁷ during cooling time, making the comparison to capped layers unreliable, and TEM measurements require long and destructive sample preparations. In practice, the modal gain of a QD laser is usually retrieved from external parameters and related empirically to growth conditions or to tendencies noted in microscope observations.

⁷ Evolution of quantum dots size after deposition is described in early studies of QD growth, for example in [87]

Average modal gain values for Stranski-Krastanov (SK) QDs grown on GaAs are 10 to 20 cm⁻¹ per layer, with a record (to our knowledge) of 60 cm⁻¹ per layer [88].

Loss sources

Losses can be separated in two groups: mirror losses, which are present but necessary, and propagation losses, also called parasitic losses because they only delay the laser threshold.

As explained earlier, the *mirror losses* are usually expressed in inverse centimeters for easier comparison to linear losses and gain:

$$\alpha_m = \frac{1}{2L} \ln\left(\frac{1}{R_1 R_2}\right) \quad (2.8)$$

Scattering or diffusion losses are due to the scattering of electric field on irregular core/cladding interfaces. While it is not describable analytically in a 3D waveguide, if we reduce the problem to two dimensions with the effective method, the scattering losses are described by [89].

$$\alpha = \frac{\sigma^2 k_0^2 k_x^2 E_s^2 \Delta n^2}{\beta \int E^2 dx} \quad (2.9)$$

where σ is the variance of roughness size distribution, Δn is the index difference between core and cladding, and $E_s^2 / \int E^2 dx$ is the normalized optical intensity at the interface.

Losses will therefore be higher for narrow waveguides with high index contrast and for a surface roughness of size comparable to the wavelength. In passive AlGaAs ridge waveguides, scattering losses can be as low as 0.05 cm⁻¹ [90].

The extension of guided mode tails up to the *contacts* can cause propagation losses. Absorption in metals (or any other lossy material) is described by a complex optical index $n = n_r + i k$, where n_r is the refractive index and k is related to the absorption coefficient by

$$\alpha = \frac{4\pi}{\lambda} k \quad (2.10)$$

Modal absorption can be evaluated from the metal complex index, either by plugging it into a mode solver and retrieving a complex propagation constant for the mode, or by calculating the confinement factor of the mode inside the lossy area. Contact losses impose a lower limit on the cladding size, but compactness, ease of

epitaxy and thermal control are factors that require thinner claddings and substrates.

Free carrier absorption (FCA) occurs when incident photons cause intraband transitions of excited carriers. Electrons are brought from the bottom to a higher point in the conduction band, and holes are brought lower in the valence band. The absorption caused by this process is proportional to the carrier density: $\alpha = \alpha_n n + \alpha_p p$. In most cases (ignoring the carriers concentration in the well), carrier densities n and p can be considered equal to the dopants concentration.

Efficiency

Above threshold, the light – current curve of a laser is linear:

$$P_{\text{opt}} = \frac{h\nu}{q} \eta_d (I - I_{th}) \quad (2.11a)$$

$$= \frac{h\nu}{q} \eta_i \frac{\alpha_m}{\alpha_p + \alpha_m} (I - I_{th}) \quad (2.11b)$$

where I_{th} is the threshold current. We have introduced the *internal or injection efficiency* η_i and the *external or differential efficiency* η_d . The internal efficiency is the fraction of carriers injected at the contacts that recombine radiatively above threshold. The external efficiency η_d is further reduced with respect to η_i since propagation losses reduce the amount of light that is extracted from the cavity.

To extract the propagation losses and internal efficiency, it is typical to plot the inverse of differential efficiency as a function of cavity length. Internal efficiency is then given by the intercept of the regression line with vertical axis, and propagation losses are proportional to the slope. This is represented in [figure 2-4](#) (for $R_1 = R_2 = R$).

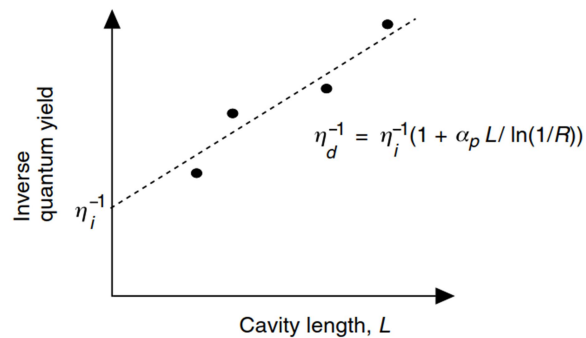


Figure 2-4. Inverse differential quantum efficiency as a function of laser cavity length. Figure taken from [75].

The *differential yield* is often used. It measures the number of optical watts obtained for each ampere injected after the threshold:

$$R_{\text{diff}} = \frac{dP}{dI} = \frac{h\nu}{q} \eta_d \quad (2.12)$$

A laser diode above threshold can be described as a perfect diode in series with a parasitic series resistance R_s . The laser power consumption is then approximately

$$P_{\text{in}} = I V_0 + R_s I^2 \quad (2.13)$$

where V_0 is the voltage difference across the junction at threshold, corresponding to the gap: $V_0 \sim h\nu/q$.

The wall-plug efficiency indicates the optical power output divided by total power consumption:

$$\eta_{\text{WP}} = \frac{P_{\text{opt}}}{P_{\text{in}}} \quad (2.14)$$

If the series resistance is null, the wall plug efficiency takes the form

$$\eta_{\text{WP}} = \eta_d \left(1 - \frac{I_{th}}{I}\right) \quad (2.15)$$

i.e. wall plug efficiency tends towards differential efficiency above threshold.

The electrical power that is not converted to optical power is dissipated in the form of heat: $P(\text{heat}) = P_{\text{in}} - P_{\text{opt}}$. Note that all terms of $P(\text{heat})$ are linear in I except for $R_s I^2$: series resistance is a significant component of laser heating. Experimentally, R_s can be extracted by taking the slope of the current-voltage curve after threshold. Lowering series resistance is a critical part of laser diode technology. An intrinsic resistance arises from the layers in the junction. It can be estimated from the carrier mobilities of the materials employed, and lowered by appropriate doping. Moreover, a parasitic resistance originates in the contacts. It can be measured locally and empirically related to the contacts fabrication method.

High operation temperatures are detrimental to laser operation, as they lower the available gain and increase nonradiative recombination mechanisms. The effect is an augmentation of the threshold current, described phenomenologically with a fit parameter T_0 :

$$I = I_0 \exp(T/T_0) \quad (2.16)$$

The lower the characteristic temperature T_0 , the more the threshold is sensitive to temperature variations. Current quantum well lasers have a T_0 in the 150-180K range for GaAs/AlGaAs QWs, and up to 200 K for strained InGaAs /AlGaAs QWs. Values for InGaAsP/InP quantum well lasers in the telecom range are lower, in the 50 K – 70 K range [86]. Record T_0 values for quantum dots lasers reach 500 K [91].

At high injection currents, heating degrades the laser characteristics further, until the light-current curve reaches a local maximum. This phenomenon, called *thermal rollover*, puts a limit on the maximal power output and efficiency achievable from a laser. Temperature increase in the laser is given by the product of output heat (described earlier) \times *thermal resistance* R_t . To keep temperature increase under control, series resistance and thermal resistance should be lowered. The thermal resistance is determined by the material heat conductivity and by the laser geometry (see [86] for analytical estimations of R_t in simple cases). Generally, geometries with low aspect ratios (wide, flat structures) should be privileged to facilitate heat conduction.

Gain in semiconductors

In section 2.1 we gave a basic description of the gain in two-levels systems. In semiconductors, energy levels are a continuum, which requires us to introduce the density of states. We remind the values of semiconductor density of states in the conduction band for various levels of confinement:

$$3\text{D(bulk)} \quad \rho(E) = \frac{1}{2\pi^2} \left(\frac{2m^*}{\hbar^2} \right)^{3/2} \sqrt{E - E_c} \quad (2.17a)$$

$$2\text{D(well)} \quad \rho(E) = \frac{m^*}{\pi\hbar^2} \Theta(E - E_c) \quad (2.17b)$$

$$1\text{D(wire)} \quad \rho(E) = \frac{m^*}{\pi\hbar} \sqrt{\frac{m^*}{2(E - E_c)}} \quad (2.17c)$$

$$0\text{D(dot)} \quad \rho(E) = 2\delta(E - E_c) \quad (2.17d)$$

with Θ the Heaviside function. Values for the valence band can be found by replacing $(E-E_c)$ with (E_v-E) , where E_c is the energy at the bottom of conduction band and E_v the energy at top of valence band. All properties are given near the Γ point for a direct-bandgap semiconductor, which allows us to take the approximation of parabolic bands with an effective mass m^* . Figure 2-5 shows the density of states for different confinement dimensions. We will ignore excitonic effects and the 1D case.

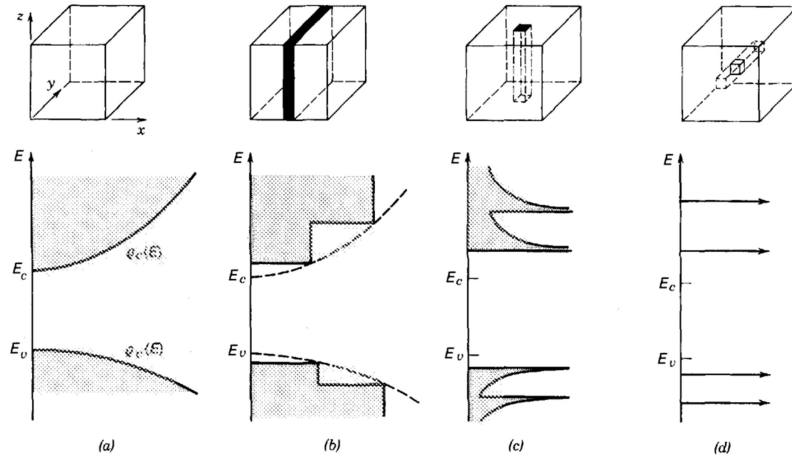


Figure 2-5. Density of states in a semiconductor for structures of decreasing dimensionality: a) bulk, b) quantum well, c) quantum wire, d) quantum dot. (figure taken from [92]).

Fermi Golden Rule

The transition rates between two states under the perturbation induced by a monochromatic plane wave are given by the Fermi Golden Rule:

$$P_{1 \rightarrow 2}^0 = \frac{2\pi}{\hbar} |\langle 1|W|2 \rangle|^2 \rho(E) \delta(E_2 - E_1 - h\nu) \quad (2.18a)$$

$$P_{2 \rightarrow 1}^0 = \frac{2\pi}{\hbar} |\langle 2|W|1 \rangle|^2 \rho(E) \delta(E_1 - E_2 + h\nu) \quad (2.18b)$$

where $\rho(E)$ is the final density of states and $\langle 1|W|2 \rangle$ is the matrix element of perturbative Hamiltonian between the initial and final state (see 2.3). Note that the transition rates for absorption and emission are symmetric.

In a semiconductor, the states are occupied with a probability given by the Fermi-Dirac function:

$$f(E) = \frac{1}{1 + \exp((E_{c,v} - E_{f_{c,v}})/kT)} \quad (2.19)$$

where E_c (E_v) indicates the energy of electrons (holes) in the conduction (valence) band, and E_{fc} (E_{fv}) indicates the Fermi energy of electrons (holes).

Taking into account the probability of occupation, the transition rate due to absorption in a semiconductor is given by $P_{21}^0 \times$ (probability that the excited state is

occupied) \times (probability that the ground state is free). This is equal to $P^{0_{21}} \times f_2 \times (1-f_1)$. Similarly, for stimulated emission,

$$P_{abs} = P_{v \rightarrow c} = P_{v \rightarrow c}^0 f_v (1 - f_c) \quad (2.20a)$$

$$P_{stim} = P_{c \rightarrow v} = P_{c \rightarrow v}^0 f_c (1 - f_v) \quad (2.20b)$$

We have replaced the indices 1,2 by v,c which refer to the valence and conduction bands.

The net emission rate is then given by the difference of the two rates:

$$P_{net} = P_{v \rightarrow c} - P_{c \rightarrow v} \quad (2.21a)$$

$$= \frac{2\pi}{\hbar} |\langle c|W|v \rangle|^2 (f_c - f_v) \rho(E) \delta(E_c - E_v - h\nu) \quad (2.21b)$$

where $|c \rangle$ and $|v \rangle$ are the electronic wave functions in the semiconductors (detailed in section 3).

The gain is obtained by summing the net emission rate over energy levels:

$$\gamma(h\nu) = A \int \frac{2\pi}{\hbar} |\langle c|W|v \rangle|^2 (f_c - f_v) \rho(E) \delta(E_c - E_v - h\nu) dE \quad (2.22)$$

where A is a constant depending on the light frequency and material properties. $g(h\nu)$ can be evaluated by inserting the forms of $\rho(E)$ from (2.17) into (2.22).

Bulk case

For a bulk semiconductor, (2.22) takes the form

$$\gamma(h\nu) = (f_c - f_v) \alpha(h\nu) \quad (2.23a)$$

$$= (f_c - f_v) \alpha_0 \sqrt{h\nu - E_g} \quad (2.23b)$$

where α_0 is the material absorption coefficient at $h\nu$ (its explicit form can be found in [75]).

The gain is positive if $f_c - f_v > 0$. Given the form of the Fermi-Dirac functions (2.19), we find that the difference of Fermi levels must be higher than E_g for amplification to occur:

$$E_{fc} - E_{fv} = E_g \quad (2.24)$$

This is known as the *Bernard-Duraffourg condition* and it corresponds to the transparency threshold of the material. Equation (2.24) is illustrated in [figure 2-6](#).

Note that in a p-n junction, the difference in Fermi levels is equal to the voltage applied outside the junction. As the voltage is increased, the difference in Fermi level is raised, and the quantity $(f_c - f_v)$ designating the inversion of population penetrates deeper into the parabola defined by $+\alpha(h\nu)$. Here the frequency of maximal gain increases with $(f_c - f_v)$. This is due to the specific form of the density of states in bulk, but it is not the case in confined heterostructures.

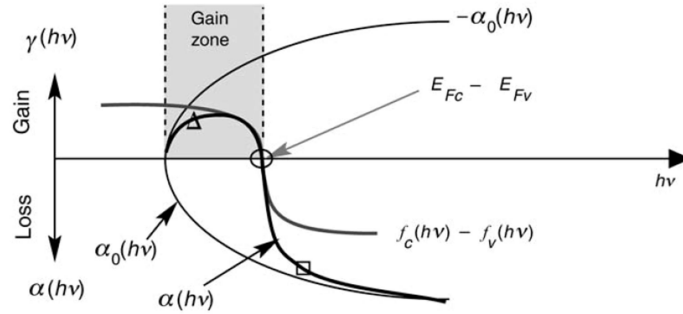


Figure 2-6. Gain diagram of a bulk semiconductor. For $h\nu > E_{fc} - E_{fv}$, the gain levels tends towards the branch $-\alpha$ (the material is absorbing). The gain (absorption) zone is marked with a triangle (square). Figure taken from [75].

In a laser, the quantity of interest is the electrical current. Current is linked to the carrier density by (2.7), and carrier density can be determined from the Fermi levels by inverting the following relations:

$$n = \int_{E_c}^{\infty} \rho_c(E) f_c(E) dE \quad (2.25a)$$

$$p = \int_{-\infty}^{E_v} \rho_v(E) f_v(E) dE \quad (2.25b)$$

Figure 2-7 shows the calculated position of $E_{fc} - E_{fv} - E_g$ for a range of carrier densities in GaAs. (See [75] for a calculation of this quantity with a Mathematica program). Transparency is achieved for a carrier density of $1.2 \times 10^{18} \text{ cm}^{-3}$.

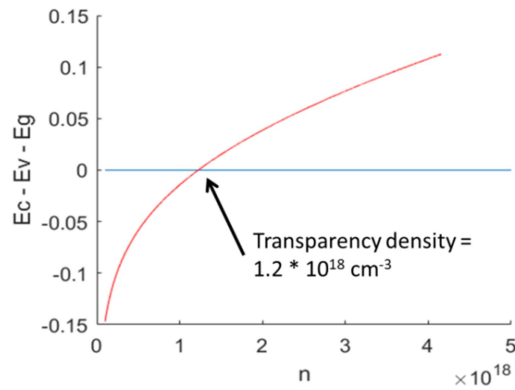


Figure 2-7. Position of quasi-Fermi levels difference – gap vs. electron concentration for GaAs

Injecting the relation between carrier density and position of Fermi levels into (2.23) allows us to calculate the gain for various current levels. Figure 2-8 shows the gain in bulk GaAs for different carrier densities. The dashed curve corresponds to the transparency density $n = 1.2 \times 10^{18} \text{ cm}^{-3}$ pointed on the previous figure. At higher densities, the gain takes positive values. Note that the position of gain maximum shifts linearly with n above threshold, and that the maximum available gain follows the useful phenomenological relation:

$$\gamma_{max} = \gamma_0 \left(\frac{n}{n_{transparency}} - 1 \right) \quad (2.26)$$

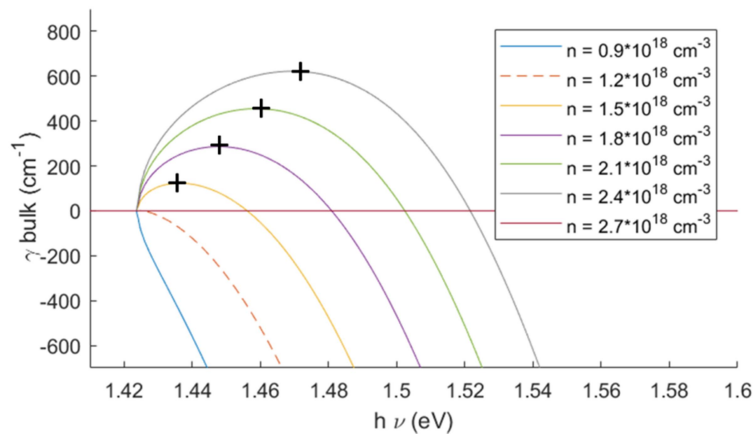


Figure 2-8. Gain in bulk GaAs. The dashed red curve corresponds to the transparency density ($n = 1.2 \times 10^{18} \text{ cm}^{-3}$). The crosses mark the maxima of gain curves.

Quantum wells

For a quantum well, the gain takes the form

$$\gamma(h\nu) = \alpha_{2D} \Theta(h\nu - E_g - e_1 - h_1) \quad (2.27)$$

where α_{2D} is the absorption coefficient of the quantum well (see [75] for its explicit value), Θ is the Heaviside or door function and e_1 (resp. h_1) is the position of the first energy level in the well in the conduction band (resp. valence band). If we assume that other energy levels are well separated in energy from the fundamental one, and do not participate in the transition, the Bernard-Duraffourg condition becomes

$$E_{fc} - E_{fv} = E_g + e_1 + h_1 \quad (2.28)$$

Equation (2.27) is illustrated in [figure 2-9](#). Unlike the case of a bulk material, the transition between null and positive gain is extremely sharp at the energy ($E_g + e_1 + h_1$). Another difference is the position of maximal gain. In a quantum well, maximal gain always occurs at the transition energy ($E_g + e_1 + h_1$), regardless of the position of Fermi levels.

These differences in the spectral gain illustrate the advantage of quantum wells over unconfined⁸ structures for their use in laser diodes. In a quantum well, the emission wavelength is less sensitive to temperature, since the gain maximum always occurs at the same energy. This wavelength is determined by the position of energy levels in the well, so it can be engineered by control of the well size and composition. Furthermore, the gain spectrum is sharper and less spread around its maximal value, so that a higher proportion of excited carriers contribute to the laser effect and population inversion is reached more quickly. More generally, we have seen in the previous section that the density of carriers in a junction can be described by

⁸ We call “unconfined” the homojunction and heterojunction structures that provide no confinement at the quantum scale (this corresponds to the de Broglie wavelength, in the range of 10 nm for a semiconductor). A homojunction indicates the junction of two materials of same composition (typically a p-doped and a n-doped layer), while a heterojunction indicates the junction of two materials of different compositions. A quantum well is technically a heterojunction, but the term “double heterojunction laser” usually refers to structures that provide only optical guiding (on the scale of a few μm) and not confinement on the quantum scale.

(2.7). In a p-n junction with no confinement, d is the size of depletion region, ranging from 1 to 10 μm . In a deep quantum well all carriers are trapped in the well of size typically ~ 10 nm. Thus a major advantage of confinement is to trap carriers in a tiny active area and reach transparency densities much more quickly.

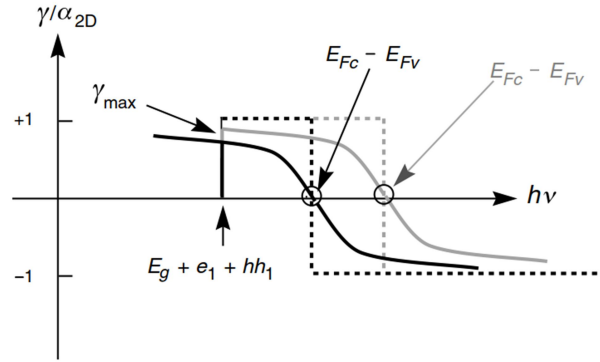


Figure 2-9. Gain diagram in a quantum well. The black (grey) curve shows gain at low (high) pump currents. Dotted curves show gain at null temperature. Figure taken from [75]

As in the bulk case, we show the gain curve for different levels of electronic density in figure 4-12. Densities are now indicated in cm^{-2} . The position of first interband transition ($E_g + e_1 + h_1 = 1.45$ eV) is marked with a vertical line. For energies under this value, $\gamma = 0$ because $\rho = 0$, and $(f_2 - f_1)$ is marked with dashed lines. For energies above this value, the normalized $\gamma = f_2 - f_1$ is plotted with full lines. The transparency density ($1.205 \times 10^{12} \text{ cm}^{-2}$) corresponds to the thicker curve. Note that the maximal gain always occurs at the energy of the first interband transition, and that the variation of maximal gain with density is not linear.

Figure 2-11 shows the maximal gain vs. 2D carrier density. This variation is often described in the literature by a logarithmic function of carrier density, where γ_0 is obtained with a fitting procedure.

$$\gamma_{max} = \gamma_0 \ln\left(\frac{n}{n_{transparency}}\right) \quad (2.29)$$

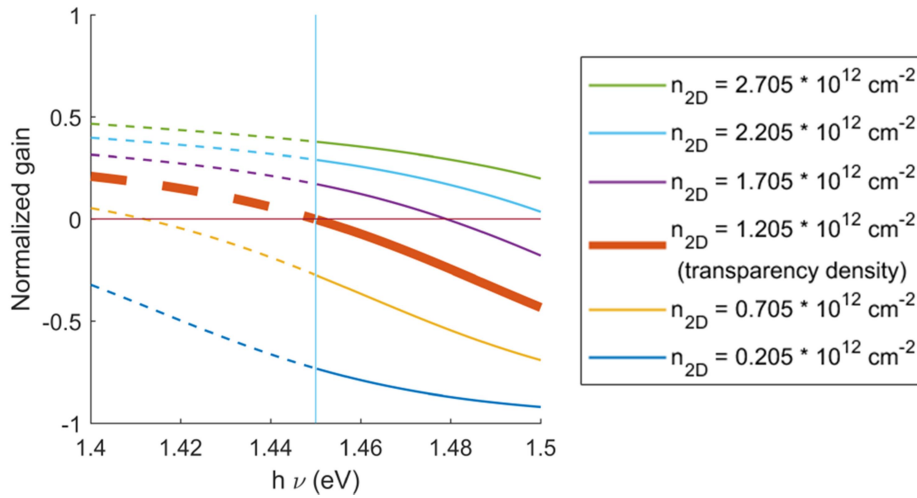


Figure 2-10. Gain in a quantum well vs. 2D carrier density. The vertical line marks the position of first interband transition ($E_g + e1 + \hbar h_1 = 1.45$ eV). Dashed (solid) lines mark energies for which the gain and density of states are null (non null).

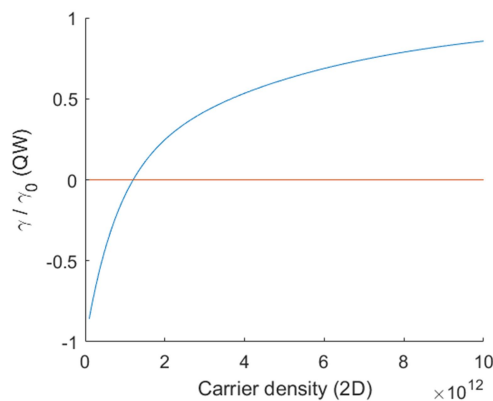


Figure 2-11. Normalized maximal gain vs. 2D carrier density in GaAs.

Quantum dots

In the simplest description of a quantum dot, the density of state is formed by a series of Dirac peaks. This particularity has earned quantum dots the name of “artificial atoms”. Early publications studying confined heterostructures predicted more attractive characteristics at increasing confinement levels: lower dependence of threshold current with temperature, sharper spectra and higher material gain [92,93]. Indeed, in unconfined and quantum well lasers, the effect of temperature increase is to spread the occupation function over a wider range of states, which decreases the value of maximal gain. This causes an augmentation of threshold current at high temperatures. In contrast, in an ideal quantum dot, there is in theory

zero spreading of the gain spectrum due to temperature. As a consequence, threshold current should be independent of temperature. Furthermore, the density of states is sharply concentrated on the level of laser emission so population inversion is reached more rapidly. The emission spectrum is also expected to be sharper and insensitive to temperature.

In practice, the quantum dots size distribution causes inhomogeneous broadening. SK-grown quantum dots layers contain on average 10^{10} to 10^{11} dots per cm^2 following a Gaussian size distribution. In SK-grown InAs/GaAs dots, this causes an average inhomogeneous broadening of 50 meV. For this reason, a significant part of early research on quantum dots was focused on the growth of homogenous layers, with pre surface patterning.

Additionally, it has been shown that the intrinsic limit for homogeneous broadening at room temperature in QDs is in the range of 20 meV [95]. As a consequence, collective lasing and mode competition tend to occur in quantum dots lasers. This has been observed in [96]: as temperature is increased from cryogenic to room temperature, the lasing spectra that was initially made of a dense ensemble of lines narrows down to a handful of modes (figure 2-12). Authors explain this by the onset of homogeneous broadening at room temperature. As the FWHM of inhomogeneous broadening expands, more QDs interact and start lasing collectively. The same mechanism has been proposed as an explanation for the local minimum in threshold current vs. temperature in [95,96]. This can be interpreted as the outcome of two effects: on one hand, the shift from individual to collective lasing tends to lower threshold current as temperature is increased. On the other hand, nonradiative recombinations cause threshold to increase with temperature.

While early theoretical calculations [94] predicted a material gain one order of magnitude higher in quantum dots than in quantum wells, broadening lowers the maximal material gain. Furthermore, mode overlap with the dots is poor in a typical QD layer, making this material gain difficult to harness. Modal gain provided by a single QD layer is only ~ 10 to 20 cm^{-1} on average, vs. several hundreds of cm^{-1} for a QW (typical thicknesses of QDs being $\sim 3 \text{ nm}$ vs. 10 nm for a QW).

Today quantum dots lasers have not replaced quantum wells as it was predicted they would, mostly because of these intrinsic limitations on broadening and modal gain. Their interest lays in particular characteristics covering niche applications.

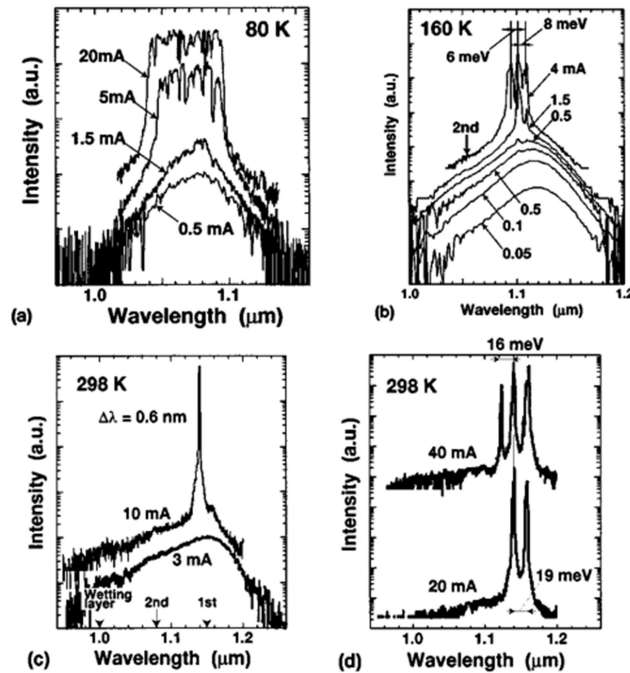


Fig. 11. Light emission spectra of the columnar-dot laser with $n = 2$, $L_{ca} = 300 \mu\text{m}$ and HR coating on both facets at (a) 80 K, (b) 160 K, and (c) and (d) 298 K.

Figure 2-12. Light emission spectra of a quantum dot laser at (a) 80 K, (b) 160 K, and (c) and (d) 298 K. Figure taken from [96].

The gain provided by a QD layer depends on inhomogeneous broadening mechanisms, on its morphology and on waveguide geometry, so making general assessments on QD gain is delicate. QD lasers tend to provide lower thresholds than QW lasers, but arrive at gain saturation more quickly. The record threshold current densities to this day have been achieved in QD lasers, reaching a one order of magnitude improvement with respect to their QW counterparts [98]; however, this result can only be achieved for low-loss cavities, e.g. for several mm long laser diodes. Figure 2-13 shows the typical gain spectrum of a QD layer vs. QW. At saturation, gain provided by a QD layer is more symmetric than in the QW case, and it can be tailored through QD morphology and mode overlap to reduce the linewidth enhancement factor [99], be extra-wide in the case of a tunable source [99,100] or provide wavelength stability at different currents [99].

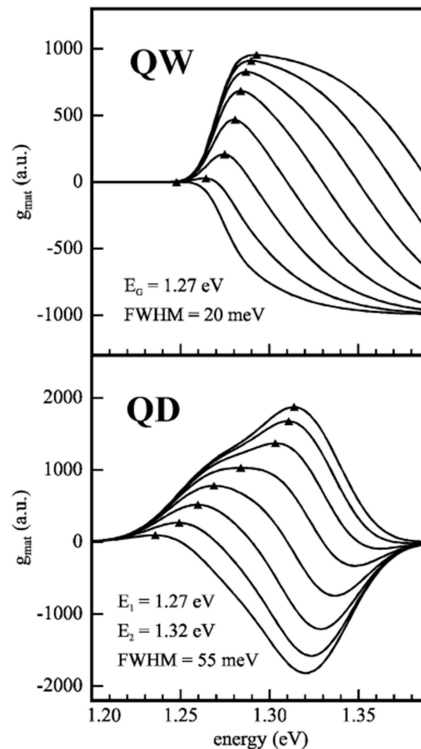


Figure 2-13. Calculated material gain for different quasi-Fermi levels, i.e., different carrier densities, in case of a QW (top) and QD active layer (bottom). Figure taken from [99]

Contrarily to predictions [93], T_0 values for QD lasers were initially poor at room temperature [97]. The introduction of changes like the dot-in-a-well (DWELL) design and p-doping [97] has increased characteristic temperatures to levels where they now exceed QW lasers performance. This makes them promising candidates for use in extreme environments, or in low-consumption networks since the temperature control stage can be removed.

Another interest of quantum dots is their ability to trap carriers and prevent nonradiative sidewall recombinations, an effect demonstrated in the 90's [62]. On the sidewalls of a QW laser, when the lattice is terminated, atoms take local configurations corresponding to energy states in the middle of the gap. These states provide pathways through which carriers may recombine nonradiatively. In QD lasers, the strong 3D confinement of carriers reduces their diffusion length and prevents their exploration of nonradiative states. This effect has permitted the demonstration of narrow (2 to 10 μm) ridge lasers in which lateral diffusion and nonradiative surface recombinations are reduced [102]. Other narrow, deeply etched quantum dots lasers have been demonstrated, in which threshold currents are comparable to large area devices [101–104]. This effect also makes QD natural

candidates for heterogeneous epitaxy of III-V dots on silicon [107]. Another interest of carrier trapping in QD lasers may be the reduction of facet overheating and catastrophic optical damage [98], although no clear demonstration of this exists to our knowledge.

Optical selection rules

Here we derive the matrix element present in (2.22). To obtain the Fermi Golden Rule, the incident monochromatic plane wave is treated as a perturbation of the Hamiltonian:

$$\begin{aligned} H &= H_0 + H_p & (2.30) \\ H_p &= \frac{q}{m_0} \vec{A} \cdot \vec{p} \\ &= \frac{q}{m_0} A \vec{e} \cdot \vec{p} \cos(\omega t - \vec{k} \cdot \vec{r}) \end{aligned}$$

where \vec{A} is the vector potential and \vec{e} is the polarization direction of light. We also use the envelope-function approximation. At semiconductor interfaces, the potential can be described as a product of a slowly varying part with a periodic atomic potential. The particle wave function ϕ is then described by:

$$\phi = \chi(r) u(r) \quad (2.31)$$

where χ is a slowly varying or envelope wave function and u is a wave function of same periodicity as the atomic potential. This is represented in figure 2-14. The envelope satisfies the Schrödinger equation for the slowly varying part of the potential, which is why the periodic part is often dropped in the description of particles in semiconductors. If the macroscopic potential is constant, the particle wave function is the product of a plane wave with a periodic function: we fall back to the case of a Bloch wave.

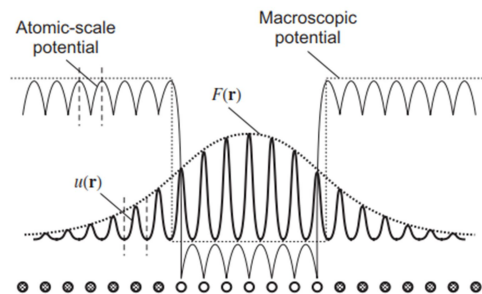


Figure 2-14. Potential and particle wave function in the envelope function approximation. $F(r)$ indicates the envelope function. Figure taken from [86].

The matrix element in (2.21) then takes the form:

$$\begin{aligned}
\langle f|W|i\rangle &= \frac{qA}{m_0} \vec{e} \langle f|\vec{p}|i\rangle \\
&= \frac{qA}{m_0} \vec{e} \langle \chi_f u_f | \vec{p} | \chi_i u_i \rangle \\
&= \frac{qA}{m_0} \left(\underbrace{\vec{e} \langle \chi_f | \vec{p} | \chi_i \rangle \langle u_f | u_i \rangle}_{\text{Intraband}} + \underbrace{\langle \chi_f | \chi_i \rangle \vec{e} \langle u_f | \vec{p} | u_i \rangle}_{\text{Interband}} \right) \quad (2.32)
\end{aligned}$$

To pass from the second line to the third, we have used the fact that \vec{p} acts on a product and that

$$\int f(x)g(x)dx = \int f(x)dx \int g(x)dx \quad (2.33)$$

if $g(x)$ is a rapidly-varying and periodic function.

The matrix elements are conveniently separated into products that contain either the envelope wave functions, dependent on bandgap variations, or the periodic wave function, dependent on the material symmetries.

In the first underlined term, $\langle u_i | u_f \rangle = \delta_{if}$ where i,f indicates the band number⁹. As a consequence, this term only applies to transitions within the same band. The product $\langle \chi_f | \vec{p} | \chi_i \rangle$ couples states of opposite parity.

In the second underlined term, $\langle \chi_f | \chi_i \rangle$ vanishes unless the transition couples levels of different bands since the wave functions of one well are orthogonal. So this term applies to interband transitions (transitions between different bands). $\langle \chi_f | \chi_i \rangle$ vanishes if the envelope functions have different parities, and if the wells are symmetric the product reduces to δ_{mn} (where m,n indicate the m^{th} / n^{th} levels in the electron/hole well). The term $\vec{e} \langle u_i | \vec{p} | u_f \rangle$ dictates the selection rules on the polarization of light and depends on the momentum of wavefunctions uif . Introduction of a quantum well breaks material symmetry, which lifts the

⁹ The functions $u(i,j)$ are orthogonal at equal \mathbf{k} , and during an optical transition \mathbf{k} can be considered constant because the photon wave vector of light is negligible with respect to electronic wave vectors.

degeneracy over band energies at the Γ point. As a consequence, most of the optical transitions occur with the heavy-hole band because it is more populated. Conservation of momentum then imposes that emitted or absorbed light is TE-polarized [108].

In SK-grown quantum dots, the fundamental interband optical transition is TE-polarized [109]. A hand-waving explanation for this behavior is that this growth technique creates flat, lenses-shaped dots. Confinement is most important in the growth direction, similarly to the QW case. Compressive strain tends to favor emission on the heavy-hole band. As a consequence, emission is TE-polarized. In dots grown in nanowires, no such constraints on morphology exist and the ground state hole band transitions from heavy-hole to light-hole like as aspect ratio is increased [110].

3. Diode-OPO: concept and design

In this chapter, we illustrate the principle and design of waveguides heterostructures operating both as diode laser and OPO. The diode-OPO or DOPO project was developed in the MPQ laboratory, after two demonstrations: 1) a twin-photon laser diode based on modal phase matching [57]; and 2) a micro-OPO based on form birefringence in a passive semiconductor waveguide pumped optically by an external laser [53]. The DOPO project proposed to combine wavelength generation and conversion in the same micrometric cavity, to reach the ambitious goal of an electrically injected and widely tunable coherent source. This design requires no alignment or epitaxy regrowth, and is extremely compact. Furthermore, it promises to harness high intracavity powers. The proposal, detailed in [61], is based on mature QD diode technology at 1 μm for down conversion around 2 μm . To this end, waveguides based on form birefringence cannot be used since they require a TM-polarized pump, while QD and QW emission is TE-polarized. As a consequence, the proposed design is based on modal phase matching. The laser is optimized to emit on a higher order mode of the waveguide, with SPDC to fundamental modes. In order to favor lasing on a higher order mode, the index is lowered in the center of waveguide core (see section 3.2.3). As a consequence, the active area is set inside a local maximum of the conduction band, which is an unusual design for laser diodes. To facilitate carriers injection towards the recombination area, composition gradients are introduced and the waveguide core is lightly doped.

Phase matching puts stringent requirements on conformity to the target structure. Conversion efficiency decays as $\text{sinc}^2(\Delta\beta L/2)$ where L is the waveguide length. For a 1 mm waveguide at pump wavelength 1 μm , this corresponds to an allowed index mismatch of 3×10^{-4} at degeneracy. This precision is typically not achieved even by state of the art molecular beam epitaxy. While temperature can be used as a control of phase mismatch during operation, wafers often have to be grown multiple times until perfect agreement with the target structure is achieved. Therefore [61] proposes to use the ridge width as an additional degree of freedom, to correct for variations of epitaxy. Waveguides are therefore narrow and deeply etched. To limit non-radiative recombination on sidewalls, quantum dots and dashes are proposed as active medium, since they have proven to efficiently trap carriers in this type of geometry [103].

Here we recall the concept of a GaAs-based diode based on the DOPO design [61] and recalculate values whenever necessary. Then we transpose this concept to InGaAsP/InP, to exploit the mature technology of 1.55 μm InP laser diodes and achieve SPDC around 3 μm . These calculations rely on index measurements of InGaAsP at 3 μm , which are presented in chapter 5. We discuss GaAs and InP-based sources side by side in this chapter.

The proposed concept is based on narrow QD laser diodes, including high-reflectivity integrated mirrors at signal and idler wavelengths. However, to validate the epitaxial structure and its impact on the modal selection, the first diodes are fabricated with a wider (~ 100 μm), uncoated guiding ridge, and are based on quantum wells. Indeed, decreasing modal gain and adding technological complexity to a validated structure is easier than starting from unconventional lasers. The laser diodes fabricated in this first batch also present relatively high dopant concentrations, which should be lowered in the future to reach OPO threshold. We focus our attention on a single vertical structure and describe various types of active area. We put emphasis on QW lasers, in order to compare expected characteristics to measurements in the next chapter, but we also describe some specific properties of QD lasers.

As 2-in-1 devices, the DOPO sources must be simultaneously efficient lasers and low-threshold OPOs. This double requirement imposes compromises in the design. We choose in priority to optimize conversion efficiency, have access to a convenient range of index mismatch and favor lasing on a higher-order mode. The impact on electrical characteristics is then estimated.

Phase-matching bandwidth and quantum dots laser spectrum

Modal and material dispersion set a limit on the range of pump wavelengths satisfying phase-matching, which is defined as the *phase-matching bandwidth*. Let us consider the simple case of degeneracy. In a medium that satisfies type-II phase matching ($\Delta k = 0$) at λ_0 , the mismatch Δk at $\lambda = \lambda_0 + \delta\lambda$ takes the form

$$\Delta k = \frac{2\pi}{\lambda} \left\{ n_{TE}(\lambda) - \frac{1}{2} n_{TE}(2\lambda) - \frac{1}{2} n_{TM}(2\lambda) \right\} \quad (3.1a)$$

$$\begin{aligned} \approx \frac{2\pi}{\lambda} \left\{ n_{TE}(\lambda_0) + \delta\lambda \frac{dn_{TE}(\lambda_0)}{d\lambda} \right. \\ \left. - \frac{1}{2} n_{TE}(2\lambda_0) - \delta\lambda \frac{dn_{TE}(2\lambda_0)}{d\lambda} \right. \\ \left. - \frac{1}{2} n_{TM}(2\lambda_0) - \delta\lambda \frac{dn_{TM}(2\lambda_0)}{d\lambda} \right\} \end{aligned} \quad (3.1b)$$

$$\approx 2\pi \frac{\delta\lambda}{\lambda_0} \left\{ \frac{dn_{TE}(\lambda_0)}{d\lambda} - \frac{dn_{TE}(2\lambda_0)}{d\lambda} - \frac{dn_{TM}(2\lambda_0)}{d\lambda} \right\} \quad (3.1c)$$

We have used the fact that the medium is phase-matched at λ_0 to eliminate terms in the second line. SPDC efficiency varies like $\text{sinc}^2(\Delta kL/2)$ if we ignore effects of mirror phase shift. The phase-matching bandwidth then becomes

$$\delta\lambda_{FWHM} = 0.88 \frac{\lambda_0}{L} \left| \left\{ \frac{dn_{TE}(\lambda_0)}{d\lambda} - \frac{dn_{TE}(2\lambda_0)}{d\lambda} - \frac{dn_{TM}(2\lambda_0)}{d\lambda} \right\} \right|^{-1} \quad (3.2)$$

In guided optics, modal dispersion and long propagation distance make the phase-matching bandwidth very narrow. For the 1mm-long waveguides presented here, the three dispersion terms are estimated around $-0.5 \mu\text{m}^{-1}$ at the pump wavelength, and from -0.1 to $-0.05 \mu\text{m}^{-1}$ at twice the pump wavelength. Thus the phase matching bandwidth is in the range of 1 nm, which sets a severe constraint on the laser emission wavelength.

Quantum dot lasers tend to provide a wider spectrum than QW lasers due to their inhomogeneous broadening. A common misconception (partially valid at low temperature) is to ignore homogeneous broadening and describe the QD layer as a collection of non-interacting dots. Each lasing line appears when a subset of dots of similar size has enough gain to overcome losses. Lasing spectrum reflects directly the size distribution and there is no mode competition. This favors wide lasing spectra, unfavorable to three-wave mixing since all optical power outside the phase-matching bandwidth is lost. Fortunately, actual QD lasers show an homogeneous broadening of the order of 20 nm at room temperature [106], causing mode competition. As a consequence, laser emission spectrum can be contained within a few nanometers [106]. See the section ‘‘Modal selection’’ for discussion of laser spectra in narrow ridge QD lasers.

Choice of epitaxial structure

Both designs presented here (on GaAs/AlGaAs and InGaAsP/InP) satisfy phase-matching between a higher-order mode of the waveguide at the pump wavelength and fundamental modes at signal and idler wavelengths. TE-polarized emission of quantum dots and wells impose type-II phase matching: $TE_{20}(\lambda_p) \Rightarrow TE_{00}(\lambda_s) + TM_{00}(\lambda_i)$. This is shown in [figure 3-1](#) at degeneracy. Pump wavelength is $0.98 \mu\text{m}$ in the GaAs/AlGaAs diode and $1.55 \mu\text{m}$ in the InGaAsP/InP diode.

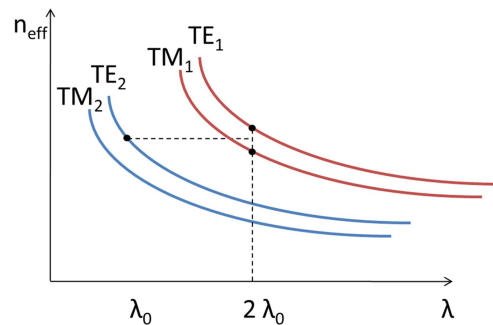


Figure 3-1. Type-II phase matching in the DOPO waveguides at degeneracy

The epitaxial structure must permit phase-matching, maximize modal overlap and favor lasing on the higher-order mode. For this last point, a camelback is introduced in the center of the waveguide.

The range of materials used is limited by the following constraints:

- Material gap should be distant enough from pump wavelength to limit absorption. This requires at least 10% Al in AlGaAs and at most 70% As in InGaAsP.
- Al fraction is capped at 80% to prevent oxidation.

Refractive index model

The refractive index model for AlGaAs is taken from [\[111\]](#). It includes the effect of temperature.

For InGaAsP, the refractive index model used is based on the measurements presented in chapter 5. Depending on the wavelength range considered, I used two different models. To calculate phase-matching conditions at degeneracy, index values are only needed at the discrete wavelengths $1.55 \mu\text{m}$ and $3.1 \mu\text{m}$. While one could use a theoretical model to fit data between these values, my measurements

are limited to three wavelengths ($\lambda = 1.55, 2.12$ and $3.1 \mu\text{m}$). This only allows for a one-oscillator fit, which may deviate from actual data at extreme wavelengths (see the discussion in [112]). It seems more precise to use measured index values whenever possible. In this case, index data at $\lambda = 1.55 \mu\text{m}$ is taken from the most precise model to my knowledge [113]. At $\lambda = 3.1 \mu\text{m}$ I used a linear interpolation of refractive index vs. As fraction based on published data for InP [114] and on my experimental values. Data presented in this chapter is calculated this way, unless otherwise specified. Since the DOPO sources will first be operated at degeneracy, this provides a starting ground to find the correct phase-matching conditions.

To estimate the source tunability outside of degeneracy, however, knowledge of the index on a larger wavelengths range is needed. In that case, I use a one-oscillator fit interpolation [109,112] presented in chapter 5. The effect of temperature on the refractive index is presented alongside.

Phase matching

The index mismatch at degeneracy, $\Delta n = n(\text{TE}_{20}, \lambda_p) - [n(\text{TE}_{00}, 2 \lambda_p) + n(\text{TM}_{00}, 2 \lambda_p)]/2$, is first calculated in a 1D waveguide, neglecting lateral confinement. We target a mismatch $\Delta n = -0.02$ since it corresponds $\Delta n = 0$ for a ridge width of $\sim 3 \mu\text{m}$. The growth structure is then modified in 2D.

Figure 3-2 shows the epitaxial structure and the interacting modes in degenerate SPDC for the GaAs-based diode. The same is shown in figure 3-3 for the InP-based diode. The calculated normalized conversion efficiencies (gain coefficients) are $740 \% \text{ W}^{-1}\text{cm}^{-2}$ (0.85 cm^{-1} if $P_{\text{pump}} = 100 \text{ mW}$) for a GaAs/AlGaAs waveguide and $300 \% \text{ W}^{-1}\text{cm}^{-2}$ (0.55 cm^{-1} if $P_{\text{pump}} = 100 \text{ mW}$) for an InGaAsP/InP waveguide, both with a ridge width of $3 \mu\text{m}$.

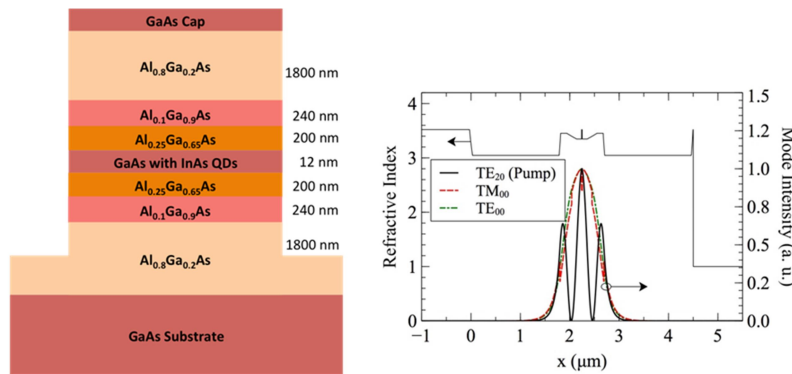


Figure 3-2. Left: epitaxial structure of the GaAs-based diode. Right: Interacting modes in degenerate SPDC [61].

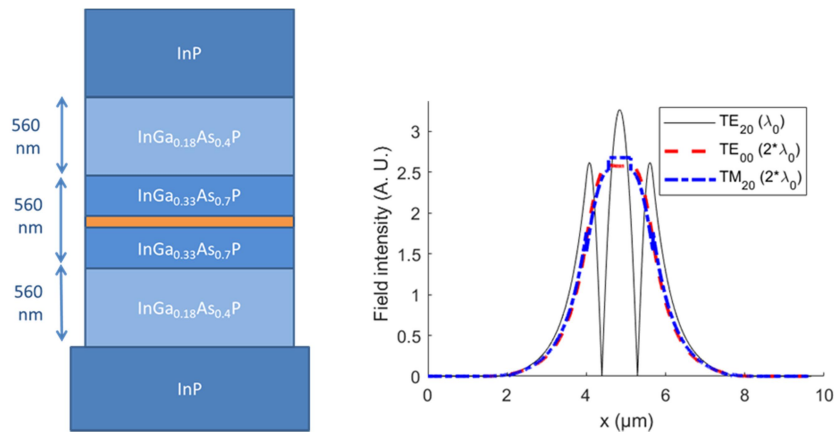


Figure 3-3. Left: epitaxial structure of the InP-based diode. Right: Interacting modes in degenerate SPDC.

Figures 3-4 and 3-5 show Δn at degeneracy vs. ridge width and pump wavelength. Index mismatch varies more slowly with ridge width in the case of the GaAs-based diode. Compensating an index mismatch is more readily achievable by modifying the pump wavelength, either by control of temperature or by growing wafers with laser emission at different wavelengths. For the InP-based diode, we tried to access a broader range of Δn at constant λ_p . At $\lambda_p = 1.55 \mu\text{m}$, Δn varies from 0.03 to -0.015 as the ridge width is varied from 2 to 8 μm , whereas in the GaAs-based diode it varies from ~ 0.002 to ~ -0.002 at a pump wavelength of 980 nm on the total ridge width range. As a consequence, tolerance on the width is decreased, as we will show in the next section.

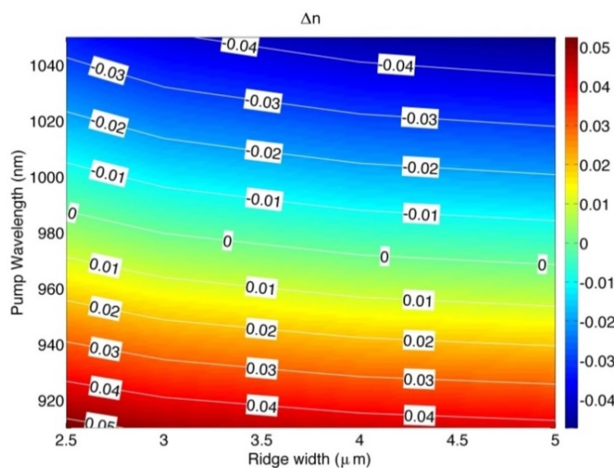


Figure 3-4. Index mismatch as a function of ridge width and pump wavelength in the GaAs-based diode [61]

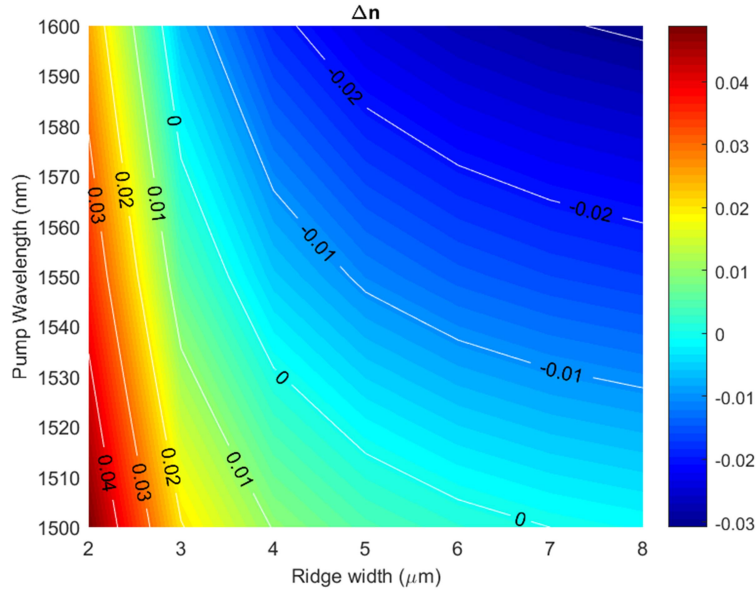


Figure 3-5. Index mismatch as a function of ridge width and pump wavelength in the InP-based diode

We present in [figure 3-6](#) the tunability of the GaAs-based diode-OPO out of degeneracy. The left graph shows tunability vs. pump wavelength at room temperature. The right part presents the temperature-controlled tunability, where we have taken into account both the temperature dependence of the refractive indices and the temperature-induced shift of the QD emission wavelength (0.5 nm/K, according to [\[116\]](#)). [Figure 3-7](#) shows equivalent data for the InP-based source, where the variation of index with temperature is neglected since no experimental data exists for the thermo-optic effect of InGaAsP at these wavelengths and since we assume that tunability arises mostly from the pump wavelength variation. As signal and idler wavelengths shift further from degeneracy, the conversion efficiency is affected by a factor $(1/\lambda_i\lambda_s)$, as seen in chapter 2.

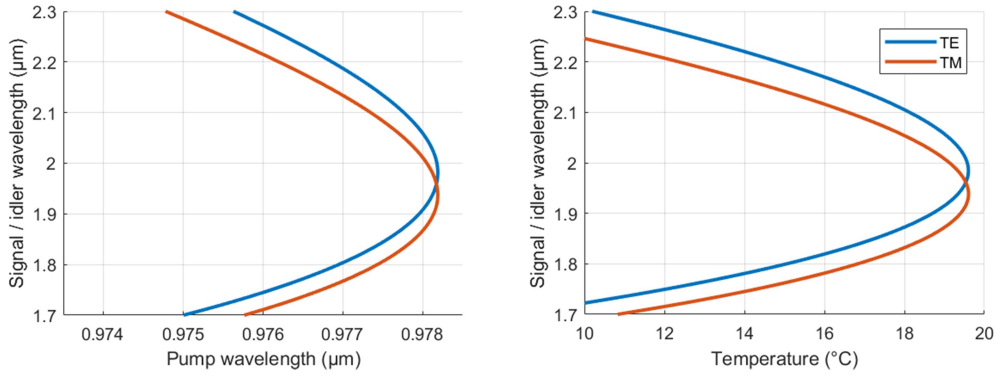


Figure 3-6. Tunability out of degeneracy of the GaAs-based diode. Left: pump wavelength varies and temperature is constant (20°C). Right: temperature-controlled tunability, where we assume a wavelength variation of 0.5 nm/K for the QD emission [116] and an index variation with temperature [111].

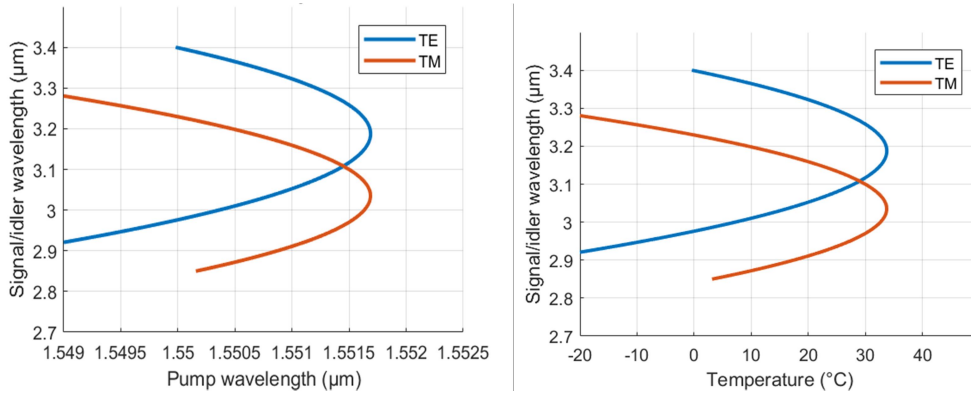


Figure 3-7. Tunability out of degeneracy of the InP-based diode. Left: pump wavelength varies and temperature is constant (20°C). Right: temperature-controlled tunability, where we assume a wavelength variation of 0.5 nm/K for the QD emission [117]. Variation of index with temperature is ignored.

Modal selection

Modal dispersion is important enough that the pump mode pattern must be precisely controlled in order to fulfill phase-matching. Our epitaxial structures are designed to satisfy phase matching with a in TE₂₀ pump, of second order in the growth direction and fundamental in the lateral direction. Optical power funneled in other lasing modes is lost.

Despite the lateral multimode nature of the waveguides dealt with in this thesis, which is due to their large width/height aspect ratio, not all lateral modes are likely to lase. QD lasers at room temperature undergo mode competition through homogeneous broadening [95]. Impact of homogenous broadening on mode

competition is highlighted in [96], where threshold current decreases and emission spectrum is narrowed as lasers are brought from cryogenic to room temperature. In [106], spectrum of ridge lasers shows lateral single mode emission over wide current and temperature ranges (~ 200 mA and 100°C), even though waveguides are $5\ \mu\text{m}$ large and deeply etched. Lateral monomode emission is also verified for deeply-etched QD microring lasers of wall thickness $3\ \mu\text{m}$ [103]. [104] finds emission on the lowest lateral modes in QD laser ridges of width $5\ \mu\text{m}$, where 30 lateral modes could be sustained.

For modes of different order in the propagation direction, modal dispersion is vanishing. Free spectral range is around $0.1\ \text{nm}$ for $2\ \text{mm}$ waveguides, so 10 longitudinal modes fit inside the phase-matching bandwidth. While several dozens of modes may lase simultaneously in a typical QD laser, only one or two lasing lines are usually above the -3dB limit [105,106]. The lasing line(s) may however not correspond to the wavelength satisfying pump-matching. In the future, this can be controlled with a DFB grating.

In the vertical direction, two factors influence modal selectivity: modal reflection and individual confinement factors.

Modal reflectivities can be calculated from the epitaxial layer structure. Using a FDTD solver, we find the following values for uncoated facets. Higher-order modes present higher modal reflectivities. A hand-waving explanation for this behavior is that reflectivity at a semiconductor / air interface increases with incidence angle, and higher-order modes have higher bouncing angles and higher divergence of emission on the fast axis. This increase of reflectivity with mode order has been described in in [118] and can lead to lasing on higher-order modes in multimode waveguides [119]. Conveniently, this effect favors lasing on TE_{20} in our structures.

	$R(\text{TE}_{00})$	$R(\text{TE}_{20})$
GaAs-based diode	0.33	0.58
InP-based diode	0.33	0.67

Table 3-1. Modal reflectivities of the first even modes in the structures presented earlier

We also favor lasing on TE_{20} by introducing a camelback in the waveguide core to maximize its overlap with the active area. Figure 3-8 shows the profiles of first symmetric modes supported by the GaAs and InP-based waveguides at the pump wavelength, in the presence of 1 to 4 quantum wells. In both waveguides, overlap of

TE_{20} with the active area is higher than that of TE_{00} if only one quantum well is present. This selectivity is more important in the InP-based diode. Inserting more wells increases index in the center, which balances the effect of camelback and as a consequence decreases modal selectivity. This effect is more pronounced in the GaAs-based diode, because of the higher well index and narrower waveguide core.

Figure 3-9 shows the confinement factor of each mode in the wells and the ratio of confinement factors. For both diodes, increasing the number of wells decreases the ratio of confinement factors. However, this effect is more pronounced in the GaAs/AlGaAs one: after 4 wells, confinement factor is the same for TE_{00} and TE_{20} . Fortunately, the impact of this effect is limited: GaAs-based lasers are grown with only one quantum well in our case, and modal reflectivity also favors lasing on the higher-order mode.

We use the following refractive index values in these calculations: on GaAs/AlGaAs, quantum wells emitting at 980 nm are usually strained InGaAs wells with 20% indium. We use a refractive index value of 3.65, given by the III-V Lab. On InP, we use the refractive index of lattice-matched InGaAsP with bandgap 0.8 eV ($y_{As} = 0.9$). The actual composition commonly used is 80% As with a 1% strain [120]. Our calculations may overestimate the index in the well, as a consequence we may underestimate the preference in modal gain given to TE_2 . Impact on confinement factor is limited (less than 0.1%).

Confinement factor and mirror losses favor the higher order mode. However, to calculate which mode lases first we also need to know the level of propagation losses, which is influenced by the doping profile. This is studied in section 4.

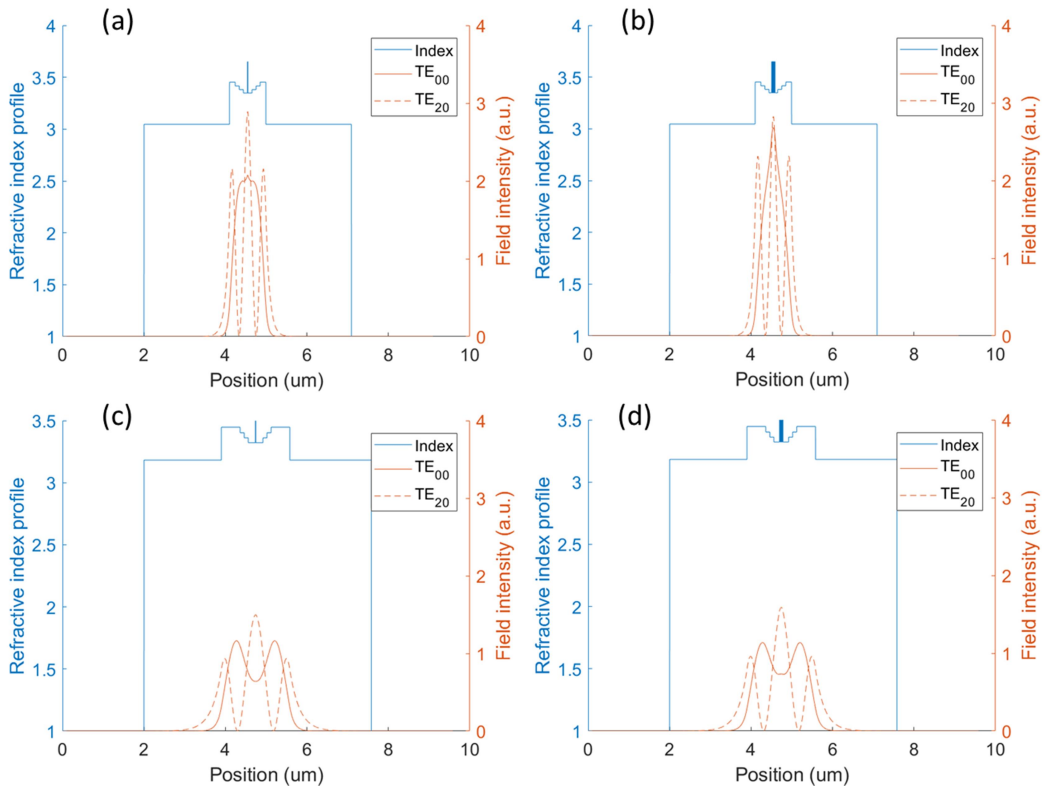


Figure 3-8. First symmetric modes supported by the waveguides in the GaAs and InP-based diodes for different numbers of quantum wells. Mode intensities are plotted against the refractive index profile. (a) and (b) show the first symmetric modes supported by the waveguide at the pump wavelength (0.978 μm) in the GaAs-based diode, if 1 and 4 quantum wells are present respectively. (c) and (d) show the same in the InP-based diode at a wavelength of 1.55 μm. Wells are 10 nm thick and spaced by 15 nm.

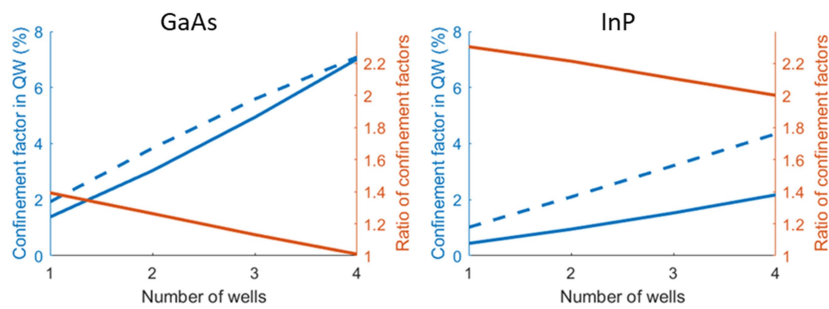


Figure 3-9. TE₂₀ (blue dotted line) and TE₀₀ (blue solid line) confinement factors for multi QW DOPOs (left axis) and their ratio (red line, right axis), as a function of the number of QWs. The lines are guides for the eyes.

Phase-matching tolerances

The proposed designs must be robust against non-nominal effective index values, which can be due to an imperfect knowledge of material index or to variations during epitaxy. Possible causes of index shifts and their impact on effective-index mismatch Δn are summarized in [table 3-2](#). Values therein are calculated for the structures presented above, with a ridge width of 3 μm . We also estimate the impact of a low-index ($n = 1.5$) cladding replacing air on the sidewalls, since filling and planarizing is a common method to contact deeply-etched ridges.

Source of effective-index change	Impact on Δn at degeneracy	
	GaAs/AlGaAs structure	InGaAsP/InP structure
$\pm 2.5\%$ thickness variation of all layers	$\pm 10^{-2}$	$\pm 3 \times 10^{-3}$
3% variation of the molar fraction in the alloy	1.5×10^{-3}	$< 10^{-2}$
Constant offset on material indices at all wavelengths	10^{-3}	10^{-3}
Offset of Δn_0 on the material indices at either λ_p or $2 \times \lambda_p$	Δn_0	Δn_0
Air is replaced with a low-index material ($n=1.5$) on the sidewalls	10^{-3}	10^{-3}
Doping	10^{-3}	-

Table 3-2. Sources of variations in the effective index mismatch for the structures presented earlier

The impact of dopant concentration on Δn is calculated in the next section for GaAs/AlGaAs only, because the index dependency on dopants for InGaAsP at 3 μm is not known at the moment. However, it will be calculated once refractive index measurements of doped InGaAsP layers are available.

The most important source of error in epitaxy is the thickness variation. A constant offset of material indices at pump and signal/idler wavelengths has a limited impact at degeneracy, since the error is mostly cancelled in the index difference. However,

an error in the estimation of material index at either pump or signal/idler wavelengths is immediately passed on the index mismatch. While AlGaAs index is well known at the relevant wavelengths, the only measurements of InGaAsP index at 3 μm are the ones presented in chapter 5 of this thesis. Precision on these measurements is limited to 10^{-2} to 2×10^{-2} , mostly because of variations in individual samples compositions. As a consequence, we propose a structure that allows for a variation of $\pm 2 \times 10^{-2}$ in effective indices (see figure 3-5).

Tolerance on the ridge width is shown in figures 3-10 and 3-11. There is an interplay between the tolerances of Δn on the pump wavelength and the ridge width, as is apparent from the slope of constant- Δn curves in figures 3-4 and 3-5. In the GaAs-based diode, tolerance on the ridge width is better but Δn must be compensated by larger variations of λ_p . In the InP-based one, the lower precision on material indices motivated us to propose a design in which a wider range of Δn is accessible at constant λ_p . As a consequence, tolerance on the ridge width is poorer. Note also that narrow waveguides provide higher conversion efficiencies, but that they result in more stringent tolerances on ridge width.

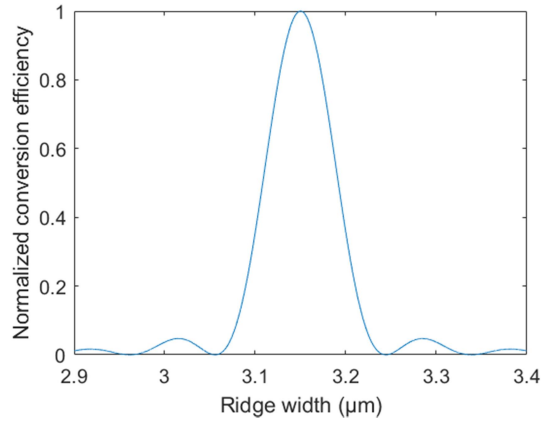


Figure 3-10. Variation of the normalized conversion efficiency with ridge width for the GaAs-based diode. Waveguide length is 1 mm and pump wavelength is 0.978 μm . FWHM of the curve is 90 nm. [61]

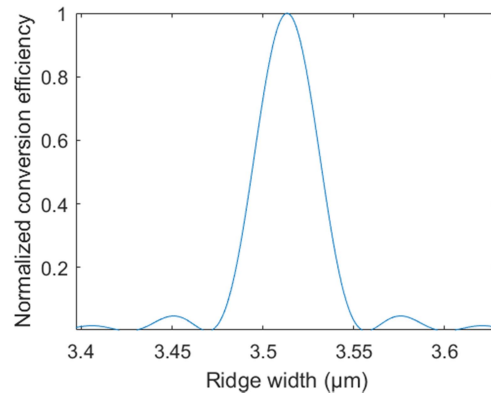


Figure 3-11. Variation of the normalized conversion efficiency with ridge width for the InP-based diode. Waveguide length is 1 mm and pump wavelength is 1.55 μm . FWHM of the curve is 40 nm.

Choice of the doping profile

The choice of the doping profile stems from a critical compromise between laser and OPO performances. Dopants lower the laser diode series resistance, but also introduce FCA losses which increase OPO threshold. We show in [figure 3-12](#) the intracavity power at OPO threshold as a function of signal / idler propagation losses. Thresholds are indicated in the best (high reflectivity¹⁰, long cavity) and worst scenario (lower reflectivity, short cavity). Losses / gain for the pump mode are supposed null, since we have shown in chapter 1 that their impact on the OPO threshold is negligible for values of reflectivities considered here.

¹⁰ The high-reflectivity case corresponds to the deposition of dielectric mirrors on the facets, as in [\[54\]](#).

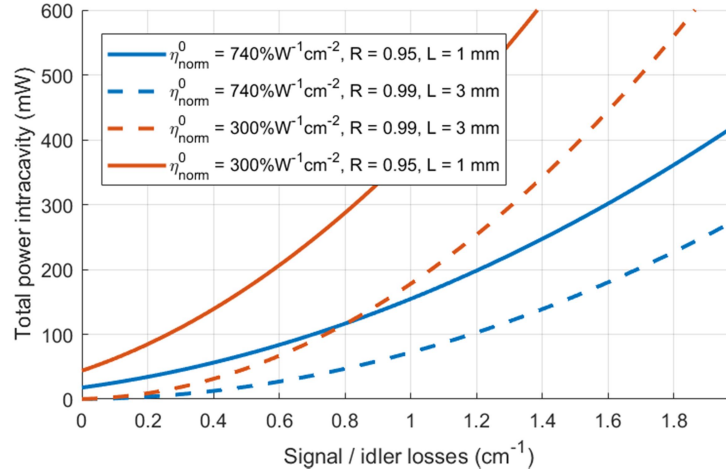


Figure 3-12. OPO threshold as a function of signal/idler propagation losses, for several values of normalized conversion efficiency, resonator length and reflectivity. Losses at the pump wavelength as assumed null.

We have simulated several doping profiles with the software Nextnano, estimating the impact on laser and OPO operation. Simulations assume a quantum well in the active area, like the first fabricated diodes based on this design.

Doping profiles in the GaAs-based diode

Figures 3-13 and 3-14 show three doping profiles in the GaAs/AlGaAs structure and the corresponding current-voltage curve. The first doping profile (in blue) is the same as in [61]. For the others, doping is reduced to decrease FCA losses. In all cases, the differential resistance is equal to $0.1 \text{ m}\Omega\text{cm}^2$ at a surface current of 600 A/cm^2 . This corresponds to a resistance of $50 \text{ m}\Omega$ for a $100 \mu\text{m} \times 2 \text{ mm}$ laser, or 1Ω for a $5 \mu\text{m} \times 2 \text{ mm}$ laser.

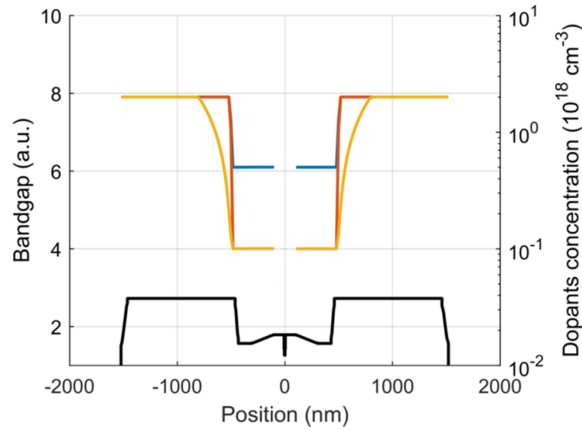


Figure 3-13 Bandgap (left axis) and three doping profiles (right axis) of the GaAs-based structure. Blue: profile 1, red : profile 2, yellow : profile 3. The gap is shown in black in arbitrary units.

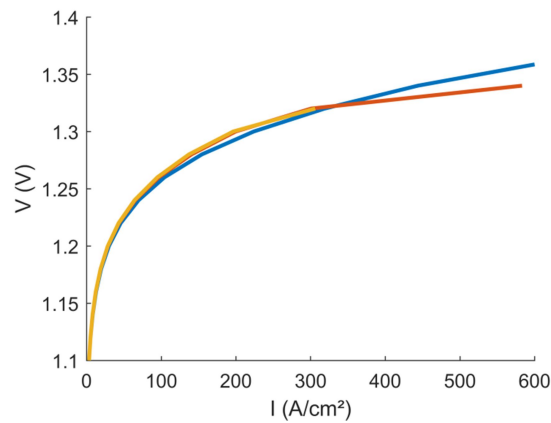


Figure 3-14. Voltage-current curves corresponding to the different doping profiles presented in [figure 3-13](#).

[Table 3-3](#) shows the corresponding FCA-induced losses at λ_p and $2 \lambda_p$. Loss coefficients, which we have defined in the previous chapter, are assumed to be $3 \times 10^{-18} \text{ cm}^2$ for electrons and $11 \times 10^{-18} \text{ cm}^2$ for holes at both wavelengths (these values are commonly used for the elaboration of AlGaAs laser diodes in the III-V Lab).

Doping profile	Losses for TE ₀₀ ($\lambda = 0.978 \mu\text{m}$) (cm ⁻¹)	Losses for TE ₂₀ ($\lambda = 0.978 \mu\text{m}$) (cm ⁻¹)	Losses for TE ₀₀ ($\lambda = 1.96 \mu\text{m}$) (cm ⁻¹)
Profile 1	2.6	3.2	3.0
Profile 2	0.6	1.5	1.1
Profile 3	0.5	0.73	0.67

Table 3-3. FCA-induced losses for the first two even modes of the waveguide at λ_p and the fundamental TE mode at $2\lambda_p$ in the GaAs-based diode. FCA losses in the active area are neglected.

Doping profiles in the InP-based diode

Different doping profiles in the InP structure are shown in [figure 3-15](#). The difference of density of states between conduction and valence band is larger in InGaAsP/InP than in GaAs/AlGaAs, which is why p-doping is usually higher in InP-based diodes. However, FCA-induced loss is higher for holes, which would push us to lower p-doping. We used for calculations of FCA losses the following values:

At $\lambda = 1.55 \mu\text{m}$, $\alpha_n = 2 \times 10^{-18} \text{ cm}^2$ and $\alpha_p = 25 \times 10^{-18} \text{ cm}^2$ [\[121\]](#)

At $\lambda = 3 \mu\text{m}$, $\alpha_n = 2.5 \times 10^{-18}$ and $\alpha_p = 35 \times 10^{-18}$ [\[122\]](#)

The two doping profiles shown here correspond to two extreme cases. In the first case, doping is high enough for efficient laser operation, but OPO threshold is in the range of 1W. In the second case, doping is kept under 10^{17} in the core and p-doping is lower than n-doping in the center, to limit propagation losses. The corresponding current-voltage curves are presented in [figure 3-16](#). Surface differential resistances are $0.1 \text{ m}\Omega \times \text{cm}^2$ for the first profile and $0.2 \text{ m}\Omega \times \text{cm}^2$ for the second. This corresponds respectively to resistances of 50 (100) m Ω for a laser of $100 \mu\text{m} \times 2 \text{ mm}$, or 1 (2) Ω for a laser of $5 \mu\text{m} \times 2 \text{ mm}$. FCA-induced losses corresponding to the two profiles are shown in [table 3-4](#).

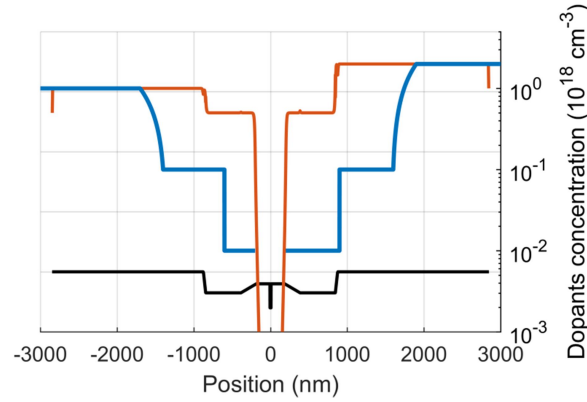


Figure 3-15. Doping profiles in the InP structure. Donors are on the left, acceptors on the right. Red : profile 1, Blue : profile 2. The gap is shown in black in arbitrary units.

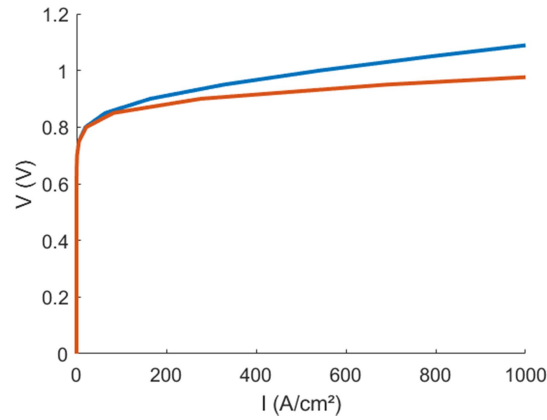


Figure 3-16. Voltage-current curve corresponding to the different doping profiles presented in [figure 3-15](#).

	Losses for TE ₀₀ ($\lambda = 1.55 \mu\text{m}$) (cm ⁻¹)	Losses for TE ₂₀ ($\lambda = 1.55 \mu\text{m}$) (cm ⁻¹)	Losses for TE ₀₀ ($\lambda = 3.1 \mu\text{m}$) (cm ⁻¹)
Profile 1	5.9	8.0	9.7
Profile 2	0.15	0.51	0.48

Table 3-4. FCA-induced losses for the first two even modes of the waveguide at λ_p and the fundamental TE mode at $2x \lambda_p$ in the InP-based diode. FCA losses in the active area are ignored.

Lowering the doping profile increases series resistance, and we can roughly estimate its impact on laser heating. Series resistance in a similar low-doped diode is 3Ω for a resonator of same length [57], albeit with Bragg mirrors. A quick

calculation from [86] gives a thermal resistance in the range of $20^{\circ}\text{C}/\text{W}$ for both diodes. Assuming a threshold of $100\text{ A}/\text{cm}^2$ (verified experimentally for quantum wells – see next chapter- and a reasonable assumption if QDs are used), total power consumption is in the range of 1 W at current 10 times threshold current. For low doping profiles, propagation losses of the pump mode are in the range of 0.7 cm^{-1} and mirror losses are 2 cm^{-1} for 2 mm long waveguides. Differential efficiency is then 25%. Depending on the threshold level, 75% to 100% of consumed power is dissipated into heat. Using the thermal resistance of $20^{\circ}\text{C}/\text{W}$ given earlier, the temperature rise is 15°C to 20°C . While this value may increase because of imperfect internal efficiency or additional thermal resistance, it is compatible with laser operation and with thermal control of the wavelength.

The first GaAs/AlGaAs laser diodes studied in this thesis have been fabricated with the highest doping profiles presented above. Results for the GaAs-based diodes are shown in the next chapter, and fabrication for InP is underway at the time of writing. As explained above, this allows us to check validity of the vertical structure before adding further modifications to the lasers. In order to reach the OPO threshold, doping should be lowered in the future, so as to follow the other profiles presented above. Modal selection of the lasing mode can be expected to be similar at other dopant levels, since doping does not alter confinement factors or ratios of propagation losses.

Modal gain necessary for laser threshold

The calculation of propagation losses at the pump wavelength allows us to calculate the material gain at laser threshold. Figure 3-17 shows the modal gain necessary to reach lasing threshold for the highest doping profiles presented, assuming an internal efficiency of 100 %. To facilitate comparison between quantum dots and wells, we do not take into account FCA losses in the active region. We consider only FCA due to dopants and mirror losses. We use the reflectivities shown in table 3-1, corresponding to uncoated facets. We take only one quantum well for the GaAs-based diode, and 4 wells in the InP-based diode since it has lower confinement in the active area and higher propagation losses. While the higher-order mode is favored at all lengths considered, discrimination is stronger for shorter waveguides. The values of modal gain required to reach lasing threshold can be compared with the value of modal gain at saturation in quantum wells and quantum dots, respectively 100 to 1000 cm^{-1} and 20 to 60 cm^{-1} (if several layers of dots are used). Lasing threshold can be achieved in both cases, but in the case of quantum wells threshold of both modes is close to the transparency current.

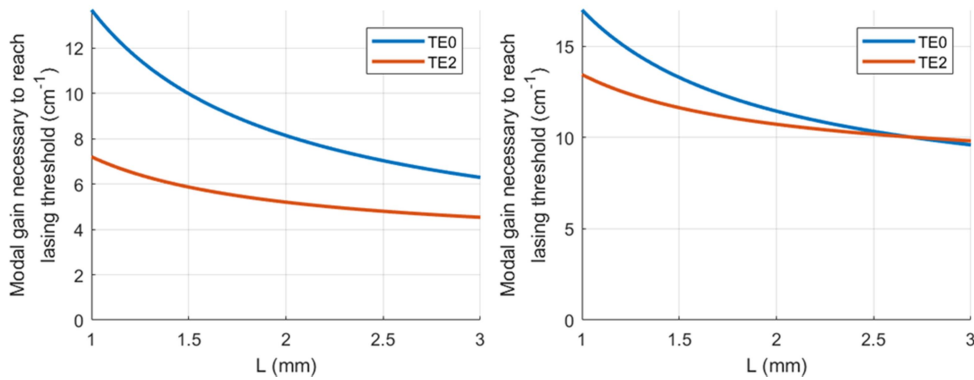


Figure 3-17. Left: (GaAs) Modal gain required to reach the lasing threshold for a single quantum well and for the doping profile 1 presented in figure 3-13. Right: (InP) Same for 4 quantum wells and for the doping profile 1 presented in figure 3-15.

Threshold current

Quantum wells

Figure 3-18 shows the material gain necessary to reach lasing threshold in the case of 1 quantum well for the GaAs-based diode and 4 wells for the InP-based one. The confinement factors used in the calculation are presented in figure 3-9.

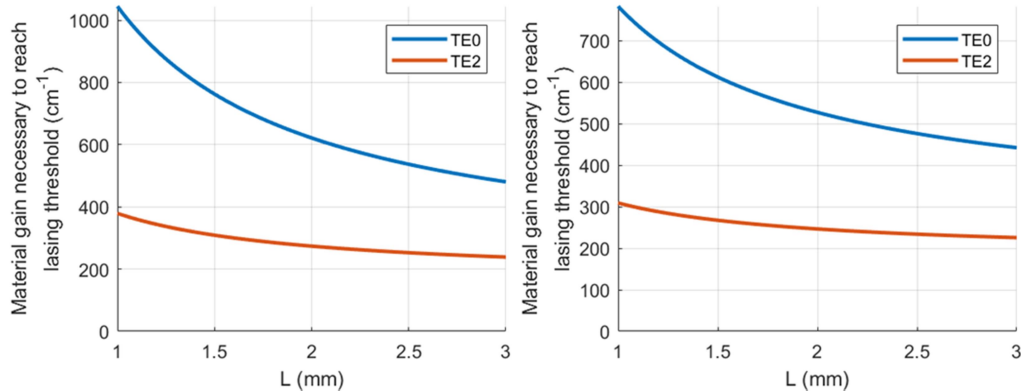


Figure 3-18. Left: (on GaAs) Material gain required to reach the lasing threshold for a single quantum well and for the doping profile 1 presented in figure 3-13. Right: (on InP) Same for 4 quantum wells and for the doping profile 1 presented in figure 3-15. The confinement factors used for the calculation are shown in figure 3-9.

Threshold current as a function of length is shown in figure 3-19. The relation between current and material gain is taken from [123] and [124] (saturated gain is 4000 cm⁻¹ for InGaAs quantum wells at 980 nm and 1500 cm⁻¹ for InGaAsP wells at 1.55 μm). Internal efficiency is assumed to be 100 % and recombination time 3 ns.

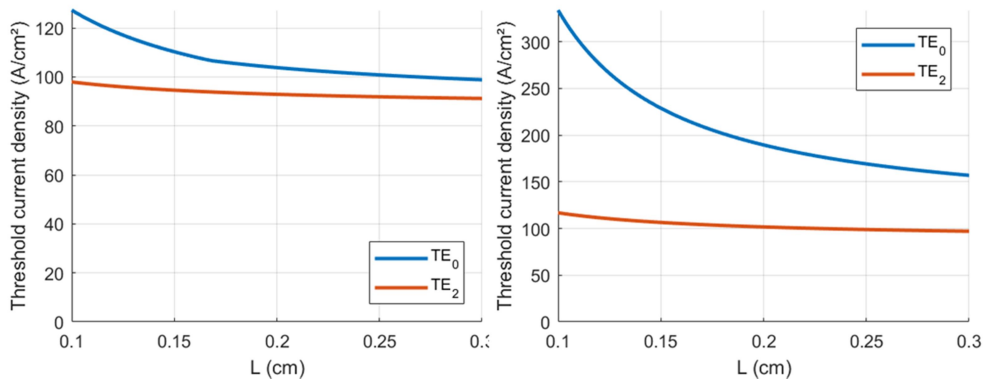


Figure 3-19. Left: (on GaAs) Threshold current density for a single quantum well and for the doping profile 1 presented in figure 3-13. Right: (on InP) Same for 4 quantum wells and for the doping profile 1 presented in figure 3-15.

Quantum dots

Calculation of threshold currents in the quantum dot case is not straightforward, since published gain values are usually given at saturation only, and when modal gain at different currents is known the amplitude of electric field in the active area is not always indicated. We present here calculated current threshold values for the GaAs-based diode (figure 3-20), from the comparison of modal gain in otherwise identical 980 nm QW/QD diodes [125]. The active area is formed of a single QD layer. Threshold currents are not calculated for the InP-based diode, but we can assume that it will fall in a reasonable range since the necessary modal gain to lase is under 15 cm^{-1} , and 1.55 μm QD lasers provide modal gain up to 100 cm^{-1} [126]. The difference between threshold currents of TE₀ and TE₂ is stronger than for QW diodes. Indeed, the gain at saturation provided by a single QW being higher than for a QD layer, threshold occurs quickly after inversion for both modes. In the case of a QD layer, threshold gains being closer to the gain at saturation, there is a larger difference in threshold current densities. Thus we can expect modal discrimination to be stronger in QD lasers.

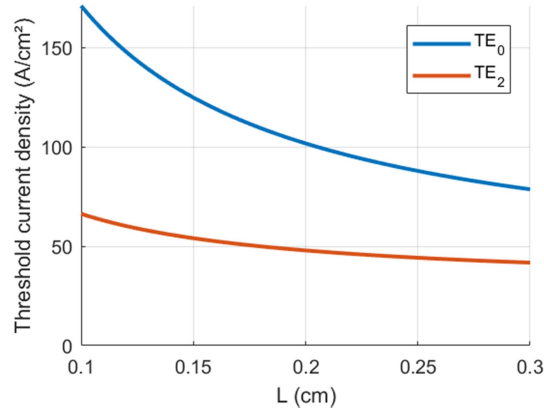


Figure 3-20. Threshold current density for a single layer of quantum dots and for the doping profile 1 presented in figure 3-13.

Additional loss sources for signal and idler

Free-carrier absorption also occurs in the active area. Table 3-5 shows the FCA-induced losses in a single quantum well for the same modes as earlier, assuming a recombination time of 3 ns and a threshold current density of 100 A/cm² (this corresponds to the threshold for the mode TE₂₀ in lasers of length 2 mm according to figure 3-19). Note that these values are calculated using the 3D absorption coefficients, that may differ from the 2D case. For the signal and idler mode, FCA absorption in the wells is not negligible compared to the nonlinear gain coefficients expected.

	Losses for TE ₀₀ (λp) (cm ⁻¹)	Losses for TE ₂₀ (λp) (cm ⁻¹)	Losses for TE ₀₀ (2 x λp) (cm ⁻¹)
GaAs-based diode	0.35	0.49	0.33
InP-based diode	0.12	0.27	0.16

Table 3-5. Losses due to FCA in a single quantum well for the structures presented above.

To calculate FCA losses in the active area (“FCA-AR losses”) for quantum dots, we consider that they are the same as for quantum wells, corrected by the threshold current: $\alpha_{\text{modal}}(\text{QD}) = \alpha_{\text{modal}}(\text{QW}) \times J_{\text{th}}(\text{QD}) / J_{\text{th}}(\text{QW})$. We do not consider that the confinement factor inside the active area (dots or wells) affects FCA-AR losses if current is constant and mode amplitude is the same in the active area. Indeed, FCA losses depend on the number of carriers encountered and not on their spatial distribution. Another way to justify this is that modal losses vary like the dots coverage fraction in their plane x 3D carrier density in the quantum dots. Carrier

density in the dots varies like the inverse of dots coverage fraction if carriers are efficiently trapped in the dots. Dots coverage fraction then cancels out. As in the case of quantum wells, we assume that absorption coefficient is the same as in three dimensions.

For the GaAs-based diode, FCA losses from absorption in the active region are then $\sim 0.15 \text{ cm}^{-1}$. This brings the total FCA-induced losses in the range of 0.8 cm^{-1} .

Conclusion

We have described waveguides providing modal phase matching at 1 and $1.55 \mu\text{m}$ and favoring laser emission on a higher-order mode. Tolerances are evaluated. Various doping profiles are proposed and their impact on laser and OPO performance estimated. Characterization of quantum well GaAs lasers based on this design are presented in the next chapter.

To reach the OPO threshold in the future, several steps can be taken. Propagation losses should be decreased by using lower doping levels and by transitioning from quantum wells to quantum dots to decrease FCA losses in the active area. Note that the lowest value of propagation loss in a laser diode is to our knowledge 0.25 cm^{-1} , demonstrated in a QD laser diode [127]. Secondly, depositing high-reflectivity mirrors at the pump wavelength can be used to reduce the threshold current and increase the intracavity optical power.

4. Laser characterizations

This chapter presents the characterizations of AlGaAs lasers based on the design presented in the previous chapter. These measurements are mainly meant to check the electrical features of the epitaxial stack, in particular series resistance, and to validate the emission on a higher-order mode. Unlike the final DOPO design, lasers from this first batch are broad area diodes (of width $100\ \mu\text{m}$) and contain a single quantum well in the active area instead of quantum dots. No mirrors or treatments are deposited on the facets. We measure light-voltage-intensity curves, far field radiation patterns and optical spectra.

Optical setup

The optical setup used for the measurement of far field radiation patterns and optical spectra is shown in [figure 4-1](#). Since beam divergence on the fast axis is large, we tilt the chips to access higher angles in the fast axis direction. Ridge direction is along x and growth axis along y . To measure light-current (LI) characteristics, we place a power meter at $0.5\ \text{mm}$ far from the exit facet at normal incidence.

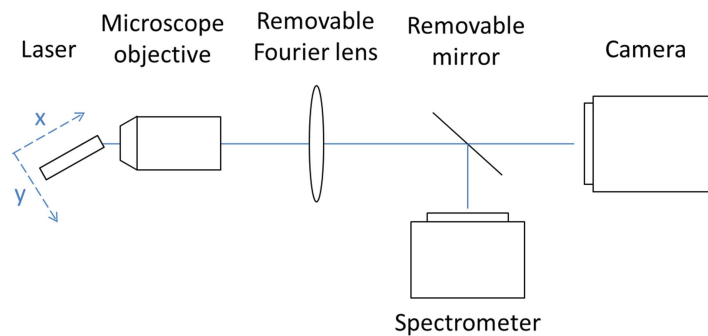


Figure 4-1. Optical setup used for lasers characterization. Light emission is along x . Growth axis is along y .

Basic characteristics

Series resistance as a function of length is shown in [figure 4-2](#). Average resistance is $0.5 \text{ m}\Omega \times \text{cm}^2$, i.e. 5 times the predicted value. [Figure 4-3](#) shows the threshold current density measured by a fit of the LI curves and by observation of the optical spectrum. The discrepancies in threshold current calculated from LI curves can be explained by slope variations due to temperature rise in lasers mounted epi-down¹¹. (A summary of which chips are mounted epi-up or epi-down is provided in [table 4-1](#)). Threshold current density ranges from 100 to 130 A/cm², as expected. [Table 4-1](#) shows a summary of laser characteristics. The values indicated are average for chips of the same length. We discuss the far-field shape and variation of differential yield in the next section.

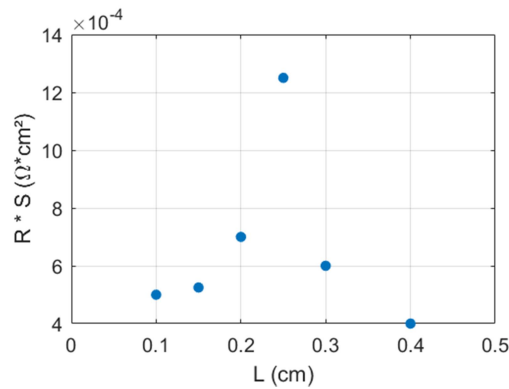


Figure 4-2. Surface series resistance as a function of laser length

¹¹ In epi-up mounting, the grown part stays on top: the bottom of substrate is attached to a laser diode mount, which is in contact with a heat sink. This is the default mounting technique, but it is not ideal in terms of heat conductivity, since the whole substrate thickness (usually $\sim 400 \mu\text{m}$) stands between the junction and the mount. If the substrate is thinned, e.g. to facilitate cleaving, it can be 100 to 150 μm thick only. In epi-down mounting, chips are flipped so the grown part is in contact with the mount. In that case, only a few micrometers of grown wafer stand between the junction and the mount, so thermal conductivity is improved.

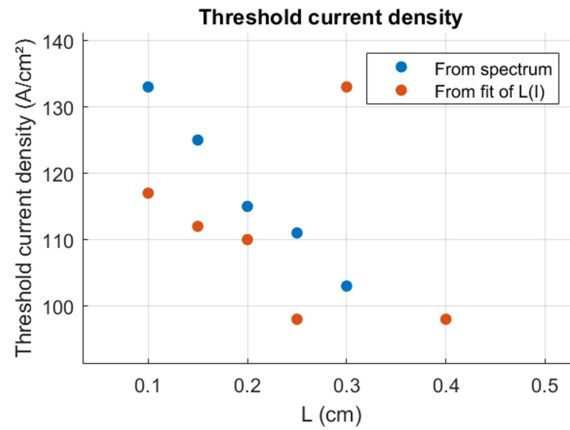


Figure 4-3. Threshold current density as a function of laser length. Blue: from observation of optical spectrum, red: from fit of light-current curves

We show an example of determination of the threshold from the light-current curve in [figure 4-4](#). Here we estimate a threshold current of 350 mA by taking the intercept of a linear fit after threshold with the horizontal axis. Total differential yield for two facets is 0.76 W/A. [Figure 4-5](#) shows the other method used for determining threshold current: observation of the optical spectrum. We consider that threshold occurs when the intensity of first laser line exceeds the spontaneous emission spectrum by a factor of 2. Here this corresponds to a threshold current of 310 mA.

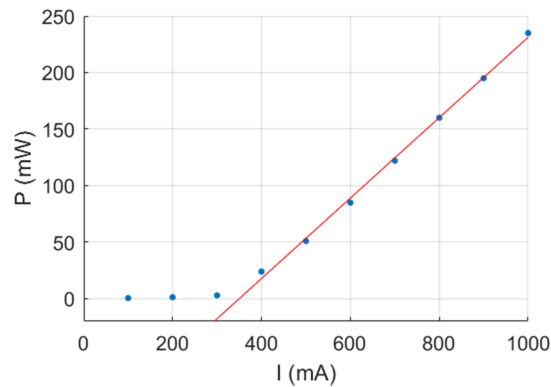


Figure 4-4. Light-current curve of laser chip n° 1402 (length 3 mm, see [table 4-1](#)), against a linear fit above threshold. We measure optical power emitted from one facet only.

	3-lobed far field			Hybrid far field	1-lobed far field	
	L = 1 mm	L = 1.5 mm	L = 2 mm	L = 2.5 mm	L = 3 mm	L = 4 mm
Chip #	1161, 1410, 1591	1412, 1477, 1636	1473, 1481	1005, 1009, 1439	1402, 1459	1234
Optical power emitted at 1A (1 facet)	120 mW	120 mW	90 mW	90 mW	220 mW	230 mW
Threshold surface current (LI fit)	117 A/cm ²	112 A/cm ²	106 A/cm ²	98 A/cm ²	117 A/cm ²	99 A/cm ²
Threshold surface current (spectrum)	133 A/cm ²	125 A/cm ²	115 A/cm ²	111 A/cm ²	103 A/cm ²	n. m.
Series resistance	0.5 Ω	0.37 Ω	0.35 Ω	0.48 Ω	0.22 Ω	0.16 Ω
Differential yield (W/A) (2 facets)	0.33 W/A	0.275 W/A	0.235 W/A	0.27 W/A	0.74 W/A	0.7 W/A

Table 4-1. Summary of laser characteristics. Grey background: epi-up (lengths 1 mm, 1.5 mm, 2.5 mm), white background: epi-down (lengths 2, 3 and 4 mm)

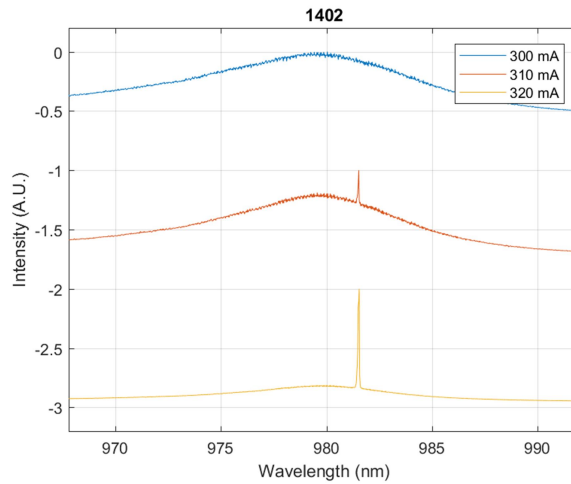


Figure 4-5. Optical spectrum of laser chip n° 1402 (length 3 mm, see [table 4-1](#)) below and above threshold.

Far field measurements

We showed in the previous chapter that the structure presented here is designed to favor lasing on the mode TE_{20} (higher-order mode in the direction of growth) from lengths 1 mm to 3 mm. [Figure 4-6](#) presents the expected far field intensity for modes TE_{00} and TE_{20} .

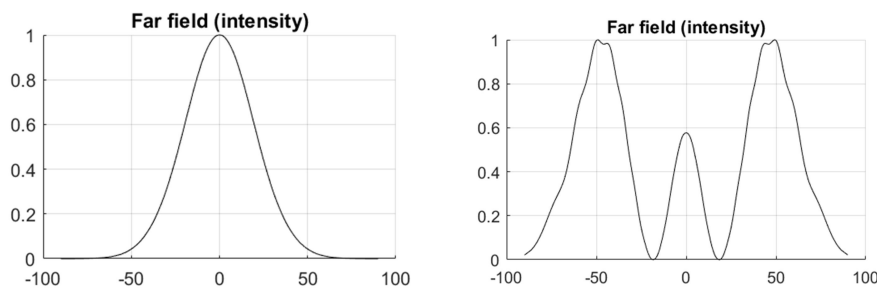


Figure 4-6. Predicted far field intensity for modes TE_{00} and TE_{20} (fundamental and first even mode in the direction of growth) vs. angle along the fast axis.

Experimental measurements show that while emission does occur on a higher-order mode for short chips ($L < 2.5$ mm), longer lasers emit on the fundamental mode. Furthermore, while the fundamental pattern of long lasers is stable and comparable to theory, the three-lobe pattern of short lasers exhibits spatial redistributions of power as current and temperature change. [Figure 4-7](#) illustrates a few examples of far fields for lasers of different lengths at several currents. We show the far field measured on a CCD, captured by a microscope objective of numerical aperture 0.8. Since divergence of the far field in the fast axis is greater than the objective aperture,

a sharp cut-off is visible in the vertical direction. For lasers emitting on a higher-order mode, we tilt the objective with respect to facet normal in order to capture a central lobe and a lateral lobe. Patterns of two different lasers are provided for $L = 1.5$ mm. While three lobes are visible for both short lasers, a comparison of the different chips does not reveal any power distribution trend set by temperature or current. Medium-length (2.5 mm) lasers emit a hybrid pattern, with different lobes but no clear node. Lasers of length 3 and 4 mm show a stable emission on the fundamental mode, regardless of temperature or current. These differences in spatial stability are highlighted in [figure 4-8](#). While the far field of a long chip shows little to no variation at different currents, it varies severely in the case of a shorter chip. Note that the objective transmission is not precisely calibrated, so comparisons are qualitative.

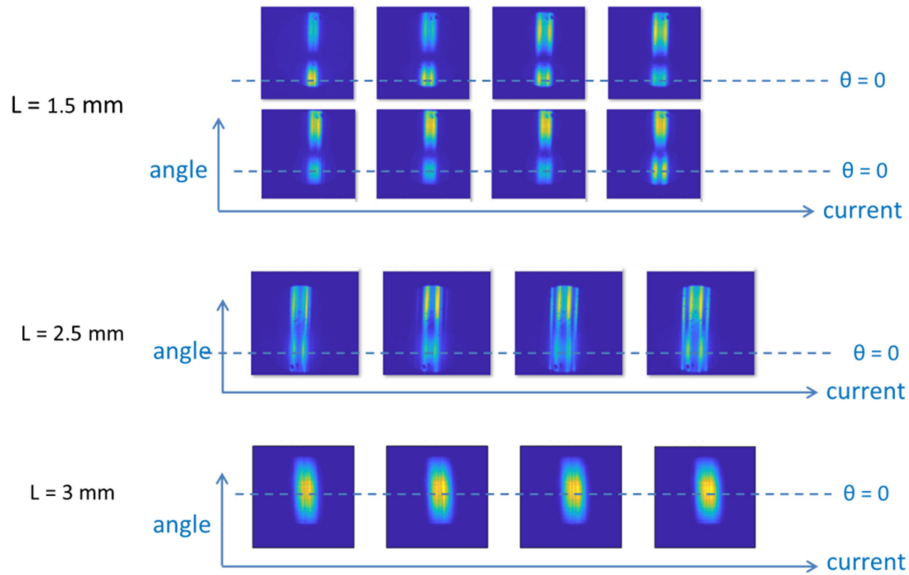


Figure 4-7. Far field of different lasers. Fast axis is in the vertical direction. Far fields of two different lasers are shown for $L = 1.5$ mm. θ denotes the angle in the growth direction with respect to the quantum well plane. Only two lobes are visible for shorter lasers because of the objective limited aperture.

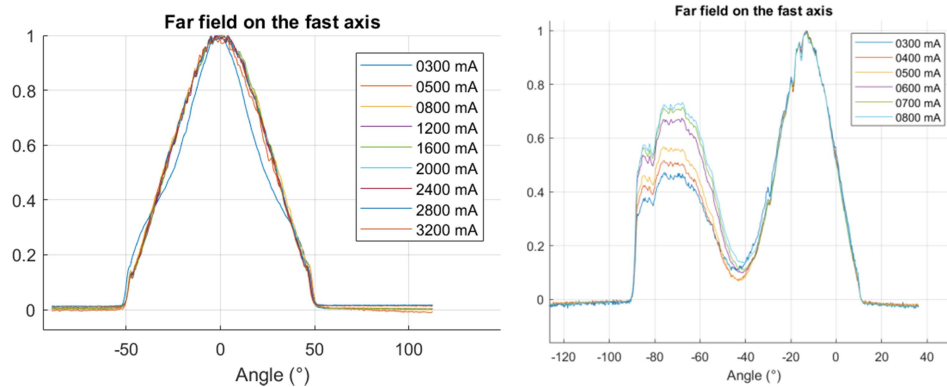


Figure 4-8. Left: far field at different currents for a laser of length 4 mm. Right: far field at different currents for a laser of length 2 mm. Intensities are normalized at the maximal value.

Figure 4-9 shows the comparison between measured and simulated far field on the fast axis for a 4 mm long laser. FWHM is 52° for the simulated pattern and 60° for the measured one. The difference may be due to lack of precise objective calibration.

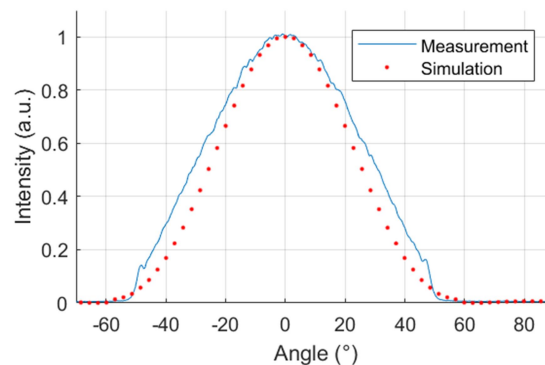


Figure 4-9. Far field on the fast axis for a 4 mm laser

Comparison of far field and internal parameters

Figure 4-10 shows the inverse of differential efficiency vs. cavity length. Two regimes are visible: low differential efficiency and high losses for lengths < 2.5 mm, and the opposite at higher lengths. This switch corresponds to the shift in far field pattern. We extract internal losses in each regime by considering in the first case a reflectivity of 0.67 (predicted for TE_{20}) and in the second case 0.33 (predicted for TE_{00}). Internal efficiencies are given by the intercept of each line with vertical axis: 45% for the first regime, 75% for the second. Internal losses are estimated as respectively 3 and 0.8 cm^{-1} . These values are comparable to predicted ones (3.7 and 3.0 cm^{-1}), albeit surprisingly low for the fundamental mode.

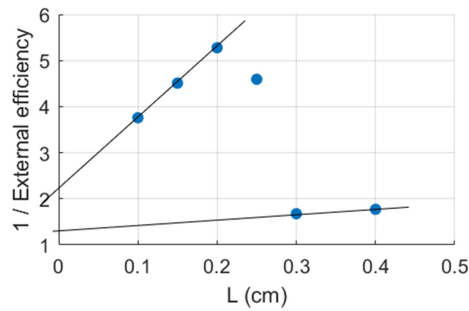


Figure 4-10. Inverse of differential efficiency as a function of length

Optical spectra show a standard variation with red shift at higher currents. As expected, the frequency spacing between different modes is in the range of 1.3 nm for lateral modes and 0.15 nm for longitudinal modes.

To determine if the far field patterns of short lasers are caused by a superposition of fundamental and higher-order modes, we compared measurements of far field and optical spectrum. There is a priori no way to identify TE_{00} and TE_{20} from spectrum, since the two modes have similar indices. However, the active area is constituted of a single quantum well, that should feed a single mode in the growth direction. In contrast, spatial hole burning is possible in the lateral direction. As a consequence, sections lasing on either TE_{00} or TE_{20} should correspond to different order modes in the lateral direction. This is testable since lateral modes are well identifiable from optical spectrum.

The alternative to this situation is that our description of waveguide index stack does not correspond to reality (for example, because of current or temperature variations) and eigenmodes take the variable shapes observed. To test this hypothesis, we measure simultaneously far field and optical spectrum. This is shown in [figure 4-11](#). At various currents, we hide either the top or the central lobe in the far field. The corresponding spectra are shown alongside far field. There is no visible correlation between lateral modes and distribution of power in different far field lobes. This tends to indicate that the observed redistributions of power do not correspond to the superposition of different sections lasing on different modes. Instead, a single mode is changing shape under environmental variations.

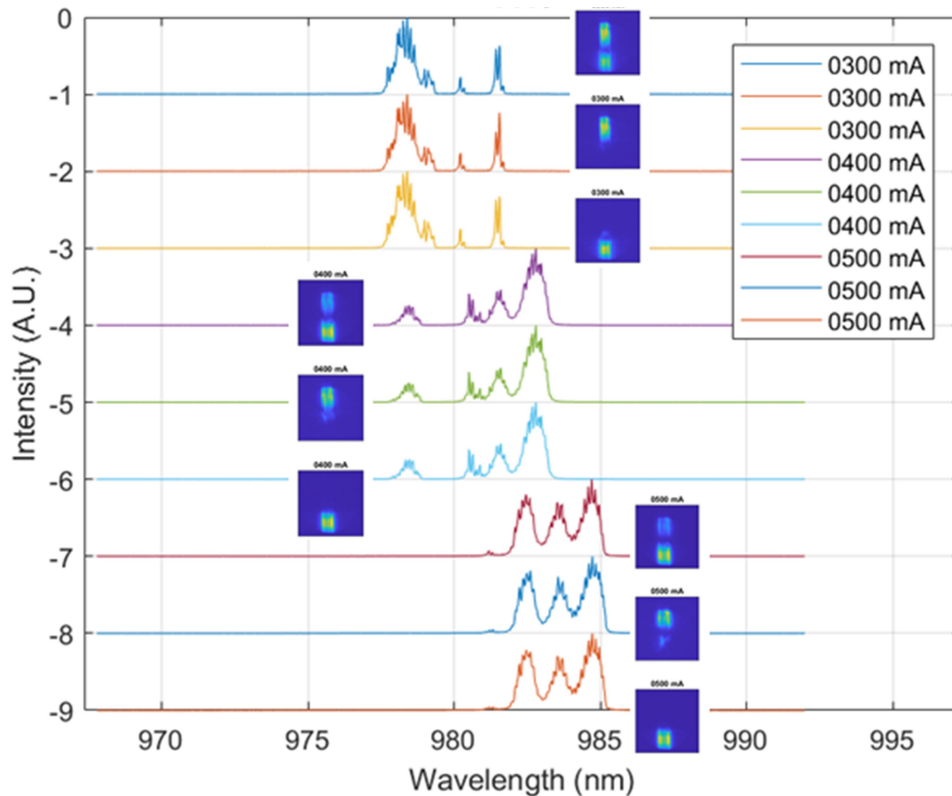


Figure 4-11. Comparison between far field and optical spectrum in a 1 mm laser. First three lines: optical spectrum taken at 300 mA, next three line: 400 mA, last three lines: 500 mA. For each current, we show from top to bottom the spectrum corresponding to a full far field, to only the top lobe and to only the central lobe.

Effect of trapped carriers outside the camelback

If, as the previous measurement suggests, variations in far field are due to modifications of the waveguide above threshold, a possible explanation is carrier accumulation. Indeed, because of the camelback in the core center, there are two local minima in the conduction band between cladding and camelback that can locally trap carriers above threshold. We simulate electrical injection after transparency threshold with the software Nextnano to evaluate the impact of these carriers on the eigenmodes. At a current 10 times above threshold, minority carriers concentration between cladding and camelback is $4 \times 10^{16} \text{ cm}^{-3}$. Impact on optical confinement due to refractive index change is negligible. In [figure 4-12](#), we show the effect of these additional carriers on propagation losses for modes TE_{00} and TE_{20} . While losses are slightly increased, no strong discrimination appears and the difference is not sufficient to explain a shift toward fundamental mode lasing.

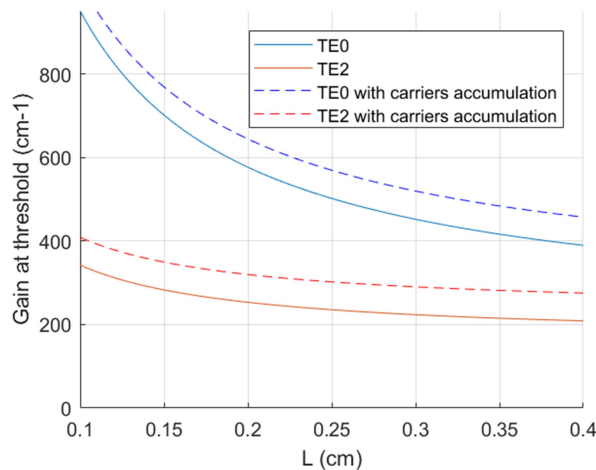


Figure 4-12. Required material gain at threshold with and without carrier accumulation between cladding and camelback.

Conclusion

The measurements presented here show that electrical performance does not suffer significantly from the unconventional vertical design of the diode-OPO. Threshold currents are in a low range for quantum well lasers (100 A/cm^2). Series resistance, however, is higher than predicted and may cause important heating in narrow geometries. At the maximal current before breakdown (ten times the threshold current), the emitted optical power is 120 mW for short ($L = 1 \text{ mm}$) cavities. Considering a facet reflectivity equal to 0.67 for the TE_{20} mode, the circulating internal power is around 700 mW. Assuming that optical power density is the same in narrow ridges (this optimistic assumption neglects thermal management issues), intracavity power would be around 35 mW in $5 \mu\text{m}$ wide cavities. This sets the maximal propagation losses for signal / idler modes under 0.2 cm^{-1} (see figure 3-12 in the previous chapter). Record propagation losses in a laser diode being 0.25 cm^{-1} , it seems like a difficult goal to achieve and OPO threshold would more likely be reached by increasing the intracavity optical power. This might be obtained through the deposition of high-reflectivity mirrors at the lasing wavelength.

Studies of the far field radiation pattern show a shift toward fundamental mode lasing for cavity lengths above 2.5 mm, which is a hindrance since the OPO threshold is lower in long cavities. The reason why we see larger differences than expected in loss levels between the two regimes is not well understood. However, measured internal losses in short lasers are in the range of predicted values (3 cm^{-1} vs. 3.7 cm^{-1} predicted) and could be further reduced by the use of lower doping levels in the waveguide, which could lead to losses as low as 0.6 cm^{-1} as shown in

chapter 3. Doping could likely be lowered under the range of values presented since the predicted series resistance does not vary significantly in the range of values tested. Deviations for the calculated TE₂₀ radiation pattern are not well understood, and might be clarified by repeating measurements on narrow ridge lasers, since modal competition can be expected to select only one lateral mode in these geometries (see the discussion on modal selection in the previous chapter).

Hence, future studies aiming at demonstrating a DOPO device as designed in chapter 3 should focus on narrow ridge waveguides with low doping levels and higher reflectivities at the laser wavelength, to reach the OPO threshold. One should note however that lowering the doping level will increase series resistance and laser heating under operation. Heating can also be expected to be more important in narrow geometries, as the thermal resistance increases because of lower contact area with heat sink. Furthermore, the operation as a laser-OPO diode will require to define a triply resonant cavity, for the pump, the signal and the idler. In an attempt to circumvent these two limitations related to the initial DOPO design, we present in chapter 7 an alternative design for an integrated diode-OPO device, based on two separated cavities linked by a vertical coupler.

5. Refractive index measurements

In this chapter, we report on refractive index measurements of InGaAsP lattice-matched to InP in a range of wavelength from 1.55 to 3 μm , based on an m-lines setup (the latter, being based on effective index measurements, might also be useful in the future to know the effective index of a planar waveguide before setting the ridge width). These measurements provided us with the design parameters for the modal phase-matched waveguide presented in chapter 3.

Justification

Nonlinear processes are extremely sensitive to index mismatches. The efficiency of spontaneous parametric down-conversion (SPDC) at degeneracy is given by

$$\eta = \eta_0 \left(\text{sinc} \left(\frac{\Delta n \pi L}{\lambda_0} \right) \right)^2 \quad (5.1)$$

where $\Delta n = n(\text{pump}) - n(\text{signal}) - n(\text{idler})$ is the index mismatch and L is the length of propagation. This function's FWHM is 0.8×10^{-3} . For device design a precise knowledge of the refractive indices is critical at pump, signal and idler wavelengths.

Our goal is to make use of mature sources existing at 1.55 μm on InGaAsP/InP and to exploit SPDC with signal and idler around 3.11 μm . While the index of InGaAsP lattice-matched to InP is well known at 1.55 μm [113,128–131], to date only one publication deals with its measurement at longer wavelengths [132], and none exists at 3 μm . This makes it crucial to accurately characterize its refractive index up to 3.14 μm , outside of the scope covered by literature data.

Principle of measurement

The evaluation of refractive indices was performed through an m-lines setup. This measurement provides a precise measurement of effective index in planar or ridge waveguides. It was proposed as early as 1986 [133], and was used for the determination of material index in various semiconductors [134,135] as well as stratified structures like multi-QW and oxidized multilayers AlGaAs waveguides [136,137]. The measurement relies on the determination of the coupling angle inside a slab waveguide of the material of interest.

Our samples consist of a layer of $\text{In}_{1-x}\text{Ga}_x\text{As}_y\text{P}_{1-y}$ lattice-matched grown over InP. As a result of the index contrast, the quaternary alloy acts as a planar waveguide. A diffraction grating is deposited or etched on the surface, the samples are mounted on a rotating mount and a laser is shone on the grating. Whenever the angle of light diffracted into the surface layer matches the bounce angle of a guided mode, coupling occurs (figure 5-1). Guided light is collected by a detector end-fire coupled at the exit facet of the sample. Coupling angles are given by the conservation of momentum

Refractive indices have been estimated with an m-lines setup, which relies on the measurement of grating-assisted coupling angles of a collimated beam into a slab waveguide of the material of interest. Since our samples consist of a layer of $\text{In}_{1-x}\text{Ga}_x\text{As}_y\text{P}_{1-y}$ lattice-matched grown over an InP substrate, and the latter has a lower index, the quaternary layers acts as a planar waveguide. A diffraction grating is deposited or etched on the surface, the samples are mounted on a rotating mount, and a laser is shone on the grating. Whenever the angle of light diffracted into the surface layer matches the bounce angle of a guided mode, coupling occurs (figure 5-1). Guided light is collected by a detector end-fire coupled at the exit facet of the sample. Coupling angles are given by the conservation of momentum:

$$\vec{k}_{in} \sin(\theta) = \vec{k}_m + m\vec{k}_g \quad (5.2)$$

where \vec{k}_{in} is the wave vector of the incident light, \vec{k}_m is the wave vector of the m-th guided mode and \vec{k}_g is the vector associated to the grating, of amplitude $2\lambda/\Lambda$ (Λ being the period) and direction perpendicular to the grating lines, in the grating plane.

This equation leads to

$$N = \sin(\theta) + m\lambda/\Lambda \quad (5.3)$$

where N is the effective index of the m-th propagating mode. This measurement therefore estimates precisely the effective indices of the guided modes, as long as the period, wavelength and coupling angles are known. Any effective index can correspond to an infinite number of {slab refractive index, slab thickness} pairs. To remove this uncertainty, at least two effective indices must be measured, or the waveguide thickness must be known with precision.

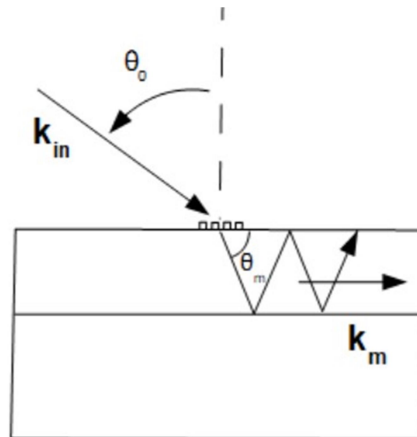


Figure 5-1. Coupling condition

In order to determine the grating period, the visible laser was shone on the sample. Under the Littrow condition, the diffracted beam exits through the entrance slit and is collected through a beam splitter on a photodiode. The grating period is retrieved through the equality

$$2\sin(\theta) = m\lambda/\Lambda \quad (5.4)$$

Sample fabrication and characterization

Growth

Samples were grown in the III-V Lab by molecular beam epitaxy. This growth technique provides the best control of composition, allowing for an accuracy of 1% on the atomic ratios. All samples consist of 1.5 μm thick layer of InGaAsP lattice-matched to InP, grown over InP. M-lines measurements require at least two guided modes to remove the uncertainty over thickness and waveguide composition. At the expected InGaAsP indices, the above planar waveguide is thick enough to sustain several modes at $\lambda = 1.55$ or 2 μm , but is single mode at $\lambda = 3$ μm . The quaternary thickness was in fact set by the maximal growth time the chamber could run without composition drifts. As a consequence, in order to infer the quaternary index at 3 μm , we combined the effective indices measured at 3 μm with the thickness estimated at 1.55 μm on the same sample.

Composition measurement

A set of samples was characterized with nominal As fractions of 0.6, 0.7, 0.75 and 0.8. The compositions with 80% As, resulting in too high absorption for clear measurements at 1.55 μm , are not included in results.

Since the precision depends critically on the composition knowledge, we characterized all the samples with X-ray diffraction and photoluminescence (the results are summarized later on, in [table 5-1](#)).

Parameters of quaternary alloys (Q) of the form $A_xB_{1-x}C_yD_{1-y}$ are commonly interpolated from those of binary alloys (B) with Vegard's law:

$$Q(x, y) = (1 - x)yB_{BC} + (1 - x)(1 - y)B_{BD} + xyB_{AC} + x(1 - y)B_{AD} \quad (5.5)$$

This interpolation only applies to additive quantities, as they can be averaged spatially (like lattice parameter or optical susceptibility). It does not hold true for the refractive index, even though in practice the difference may be negligible.

A more precise relation for the gap and composition of InGaAsP is given in [\[138\]](#). This article relates lattice parameter measured by X-ray diffraction to atomic fractions directly measured by electron probe microanalysis:

$$\begin{aligned} \frac{\Delta a}{a} &\equiv \frac{a(x, y) - a(\text{InP})}{a(\text{InP})} \\ &= 0.03227y - 0.07128x + 0.002214xy \end{aligned} \quad (5.6)$$

For $\Delta a/a = 0$,

$$x = 0.4527y / (1 - 0.0311y) \quad (5.7)$$

Since x and y are linked, the quaternary is commonly referred to only by its As (y) fraction. [Figure 5-2](#) shows the difference in Ga fraction in InGaAsP lattice-matched to InP according to different models [\[138–140\]](#). The maximal variation, 4×10^{-3} , is below the precision of epitaxial growth ($\sim 1\%$).

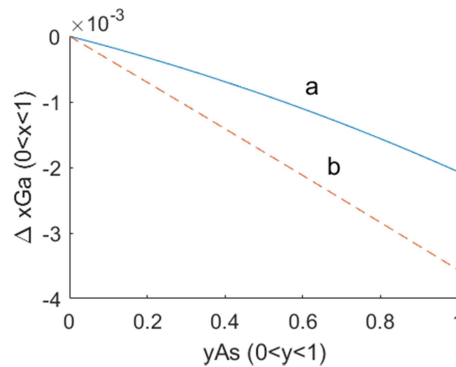


Figure 5-2. Difference to the formula proposed by [\[139\]](#), for the relation between Ga and As fraction in InGaAsP lattice-matched to InP. a : difference to [\[140\]](#). b : difference to [\[138\]](#).

Several models of the energy gap as a function of individual atomic fractions exist. A review and the most precise relation to date can be found in [138]:

$$E_g = 1.35 + 0.668x - 1.068y + 0.758x^2 + 0.078y^2 - 0.069xy - 0.332x^2y + 0.03xy^2 \quad (5.8)$$

Equations (5.6) and (5.7) can be inverted to find x and y from the lattice parameter and photoluminescence wavelength.

Choice of grating period

We estimate uncertainties in measurements of period and index by deriving (5.3) and (5.4):

$$d\Lambda = m\lambda \frac{\cos(\theta)d\theta}{2\sin(\theta)^2} \quad (5.9)$$

$$dN = d\theta \cos(\theta) + \frac{m\lambda}{\Lambda^2} d\Lambda \quad (5.10)$$

The coupling angle increases with the grating period, so both uncertainties decrease for an increasing grating period. However, measurements are noisier at higher coupling angles, as more scattered light reaches the detector. We found that angles of about 20° offered a good compromise.

As explained earlier, characterizations at $3 \mu\text{m}$ were accompanied by measurements at $1.55 \mu\text{m}$ to deduce the waveguide thickness. The modes involved, 2nd order diffracted mode at $1.55 \mu\text{m}$ and 1st order at $3.11 \mu\text{m}$, are diffracted roughly in the same direction. In order to couple light at an angle of approximately 20° , the period chosen for these samples was about $1 \mu\text{m}$.

For measurements at $\lambda = 2.12 \mu\text{m}$, we also adopted grating periods that allowed coupling at $\lambda = 1.55 \mu\text{m}$, to facilitate measurements (see section 2.4.2). The chosen period was about 600 nm , to couple a $1.55 \mu\text{m}$ beam around 30° and a $2.12 \mu\text{m}$ one around -20° .

Gratings fabrication

I fabricated the gratings by e-beam lithography, since the required feature size (0.5 to $1 \mu\text{m}$) is too small for the optical lithography available in our clean room. Fabrication parameters are chosen so as to stay as close as possible to the approximation of homogeneous planar waveguides. For this, gratings should be of uniform depth, and thin enough to be only weakly perturbative. Patterns are

fabricated by two methods. Either gratings are patterned in resist and the samples can be used as such, or I proceed to etch samples and removed any remaining resist. The first method is guaranteed to provide an even profile, but it leads to lower coupling rates and delicate sample manipulation. Furthermore, resist contributes to effective index while its material index is unknown (see section 2.6.1 for an empirical estimation of this perturbation). Shallow etching patterns is more convenient and removes uncertainty on material index, but can produce uneven rates along the surface.

Since detail of the lithography process is available in chapter 6, I only briefly explain here the choices made for these specific patterns. I spin-coat the thinnest resist available (MAN 2401) at maximum speed (6000 rpm) on samples of ~ 5 mm of side. This yields a resist thickness of ~ 80 nm. Patterns of 1 mm^2 are lithographed by e-beam. To expose all area within a reasonable duration, I use a $30 \text{ }\mu\text{m}$ aperture for periods of $1 \text{ }\mu\text{m}$. This imposes low dose and acceleration voltage (10 kV and 60 C/cm^2) to avoid overexposure. Beam speed is between 2 and 3.5 mm/s ¹², and current around 130 pA. For smaller periods ($\sim 600 \text{ nm}$), proximity effects lead to overexposure, so I lower the aperture to $15 \text{ }\mu\text{m}$ and use a 15 kV acceleration. The exposure duration is then in the range of 2.5 hours, and current is about 33 pA.

Patterns are exposed in fixed stage moving beam (FSMB) mode. The zone is divided in a set of working areas. In each one of them, the stage remains still while the electron beam is deflected to cover the area. The maximum possible value of working area in our SEM is 1 mm^2 , so all pattern can be exposed from a central position, or smaller working areas can be set. In the latter case, better homogeneity can be reached, but offsets may occur between zones, depending on the quality of alignment and calibration. After testing working areas of length 1 mm^2 and $100 \text{ }\mu\text{m}$, I would recommend using $100 \text{ }\mu\text{m}$. If the microscope is correctly calibrated, areas mismatch can be virtually eliminated, and the pattern is more homogeneous. This is visible by camera during a coupling measurement: with a uniform period, the

¹² Beam speed should be kept under 4 mm/s on this microscope for the lithography to be reproducible.

whole exit facet lights up and darkens evenly as the sample is rotated. Irregularities or illumination traveling from top to bottom indicate an inconsistent pattern.

After exposure, the samples are developed in MIF 719 and observed every 8 seconds of development until their aspect is satisfactory. Then either the samples are used as such or they can be etched. For etches, samples are attacked with highly diluted piranha sauce (H_2O_2 : H_2SO_4 : H_2O 1:1:35) for approximately 30 seconds. Remaining resist is removed with acetone and isopropanol. Grating depth is between 20 and 60 nm, depending on the etch duration. SEM and AFM observations show good homogeneity of period, filling factor and depth along the surface, with variations within the measurement accuracy.

Measurement

Optical setup

The optical setup is sketched in [figure 5-3](#). Three laser beams are combined with a precision of 0.01° : 1) a visible one at $\lambda = 543$ nm for alignment and period measurements; 2) a fibered laser at $\lambda = 1.55$ μm ; and 3) a free-space laser diode at $\lambda = 2.12$, 3.14 or 3.17 μm . Polarization is controlled with a fiber polarization controller and/or a half-wave plate. The sample is placed on the axis of a rotating stage driven by a stepper motor. The detection setup rotates with the sample.

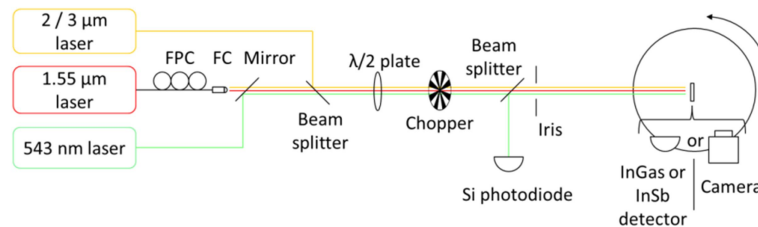


Figure 5-3. Optical setup for index measurement. FPC: fiber polarization controller, FC: fiber collimator. A detailed view of the alignment and detection setup on the rotating mount is presented in [figure 5-4](#).

[Figure 5-4](#) presents a detailed view of the alignment and detection apparatus on the rotating mount. A first translation stage (1) brings the rotation axis on the optical axis. Elements (2) and (3) are an automatic and a manual rotation stage, respectively. A tilt platform (4) is used to make a grating line coincident with the rotation axis. Translation stages (5) and (6) ensure that the sample (7) lies on the point of incidence of the laser. A photodiode is mounted on a translation stage (10). It is preceded by a focusing lens (9) set in a translation mount to adjust the focal

length, and a slit (8) to diminish stray light in the detector. A microscope (11) is placed on the vertical axis. It is mounted on translation stages not shown here.

Measurement procedure

The setup shown in [figure 5-4](#) ensures that the sample lies on both rotation and optical axis and that grating lines are vertical. This is established with the following steps.

- With microscope (11), check that the rotation axis of manual (3) and motorized (2) stages are coincident.
- Check that rotation axes are vertical: the reflection from the sample's surface should stay at the same height as stages are rotated.

After these steps, rotation and vertical axis should be coincident and remain so. In order to align stages, we follow this procedure:

- Mark the position of the rotation axis by setting a sharp object like a needle close to the sample and bringing it on the rotation axis with stages (5). Using a reticle, center the microscope on the rotation axis.
- Make the rotation axis cross optical axis: adjust stage (1) to center the needle in the laser spot of incidence. Adjust position of the microscope.
- Bring the diffraction grating on the crossing point of rotation and optical axis: adjust (5) and (6) to bring the sample in the spot marked by the reticle, while maximizing the diffracted beam intensity.
- Correct the angle of the sample: with tilt (4), ensure that grating lines are vertical (reflected and diffracted beams should arrive at the same height as the incident beam)
- Modifying the angle may bring the grating out of rotation or optical axis, so repeat the last two steps until they are both satisfied.

To align the detector (10), we replace it with an InGaAs camera and shine a 1.55 μm laser on the sample. Then we sweep angles around the expected coupling position until the exit facet lit up. Once the position of coupling at 1.55 μm is known, we replace the camera with a photodiode receptive at both 1.55 μm and the wavelength of interest. The positions of photodiode and lens are finally adjusted to maximize intensity.

To find the angle of normal incidence, measurements are done in a single long scan, with symmetric angles. Whenever θ_1 is a coupling angle, the light couples as well at

$\theta_2 = -\theta_1$, reflects on the back facet and registers in the detector. Thus the angle of normal incidence is taken to be $(\theta_1 + \theta_2)/2$. This reduces the error bar due to a possible misalignment of the beams and to the motor backlash.

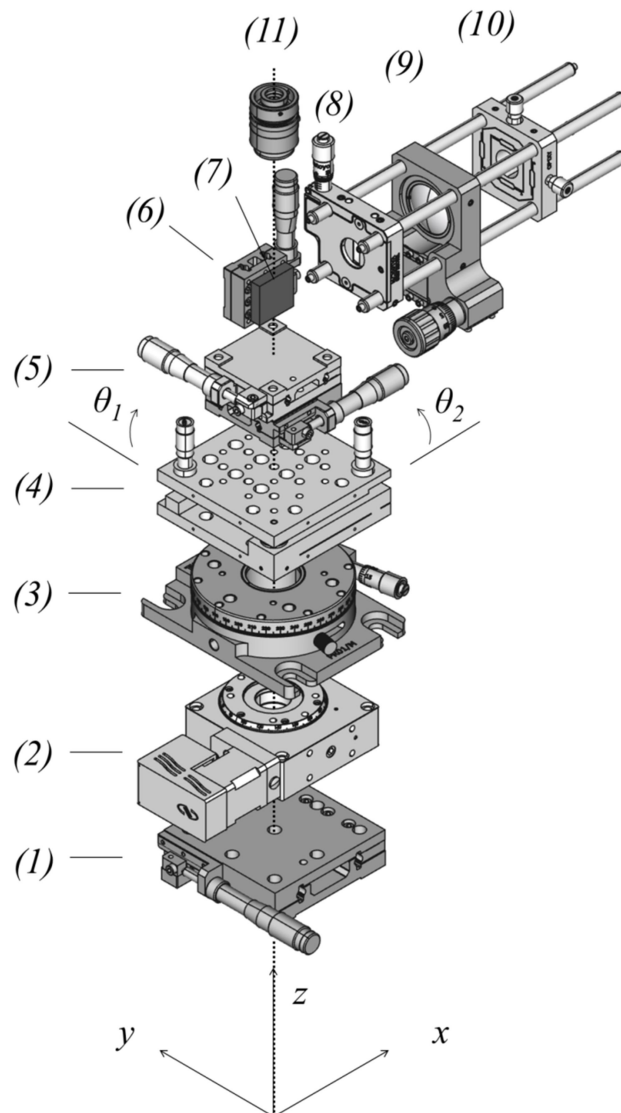


Figure 5-4. Elements of the rotating setup: (1) translation stage, (2) stepper-motor rotation stage, (3) manual rotation stage, (4) tilt platform, (5) x-y translation stage, (6) z translation stage, (7) sample, (8) vertical slit, (9) lens in an out-of-plane translation mount, (10) photodiode in an in-plane translation mount, (11) microscope objective, fixed on translation stages not shown here. Elements (5) to (10) are rigidly connected and rotate together.

Results

A typical result of coupling measurement is shown in [figure 5-5](#). The position of peaks is determined with a precision of 0.01° . Ignoring the impact of photoresist, the effective indices are a function of three parameters: InP index, InGaAsP index and thickness of the guiding layer. Of these three parameters, only the first (InP index) is known. As a consequence, each measured value corresponds to a range of possible {InGaAsP index, thickness} pairs. To find the correct index and thickness, we use the technique presented in [\[48,141\]](#). We calculate the expected effective index for a range of index and thickness values. The points where the calculated index corresponds to the measured index form a line in this space of parameters. Since more than one waveguide mode is measured, it is possible to determine the guide thickness and material index at the crossing point. This is shown in [figure 5-6](#), where each line represents the space of parameters corresponding to one value of measured effective index. [Figure 5-7](#) shows the average difference between measured and calculated effective indices for a range of parameters.

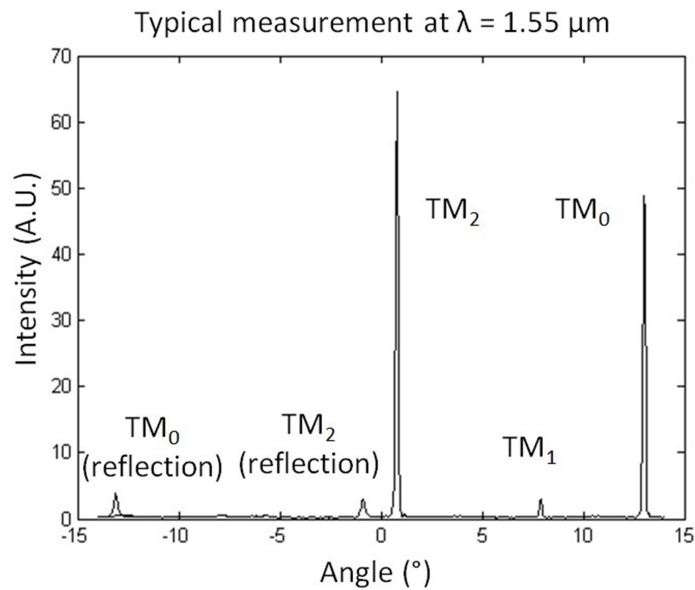


Figure 5-5. Example of coupling measurement at a wavelength of $1.55 \mu\text{m}$

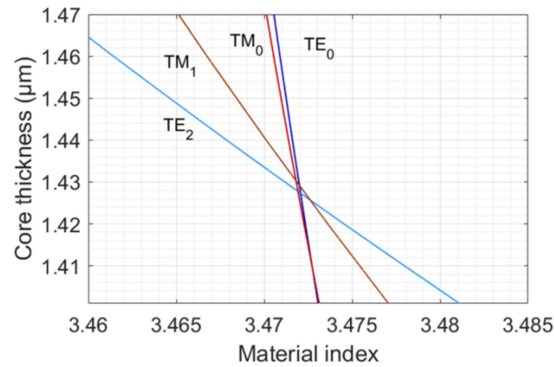


Figure 5-6. Determination of the refractive index and thickness for a slab of $\text{In}_{0.67}\text{Ga}_{0.33}\text{As}_{0.72}\text{P}_{0.28}$ at $\lambda = 1.55 \mu\text{m}$. Each line shows the possible range of data corresponding to the measured value of effective index of a particular guided mode

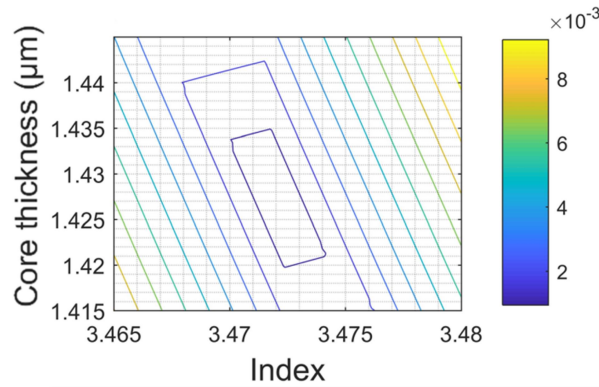


Figure 5-7. Determination of the refractive index and core thickness for a slab of $\text{In}_{0.67}\text{Ga}_{0.33}\text{As}_{0.72}\text{P}_{0.28}$ on InP at a wavelength of $1.55 \mu\text{m}$. This figure shows the mean of deviations between calculated and measured effective indices for the modes shown in [figure 5-6](#)

[Figure 5-8](#) shows the material indices measured as a function of As fraction, at wavelengths of 1.55, 2.12 and $3.14 \mu\text{m}$. Data for InP was taken from [\[114\]](#). We plot these data against the most precise model to our knowledge at $\lambda = 1.55 \mu\text{m}$ ([\[113\]](#), from the Tanguy model [\[142\]](#)). At $\lambda = 2$ and $3 \mu\text{m}$, no precise model being available, we plot data against a linear regression versus the atomic fraction of As (y), since previous publications show that this approximation is valid [\[113,128–132\]](#).

[Table 5-1](#) is a summary of material parameters and measured material index values for all samples considered. We show the peak of photoluminescence, lattice mismatch measured by X-ray diffraction, Ga and As fraction inferred from this data (through the model presented in [\[138\]](#)), and material index measured at diverse wavelengths. Samples of same composition come from the same wafer. Lattice

mismatch was assumed to be homogeneous along each wafer. Photoluminescence was measured on all samples and was found to be homogeneous along each wafer.

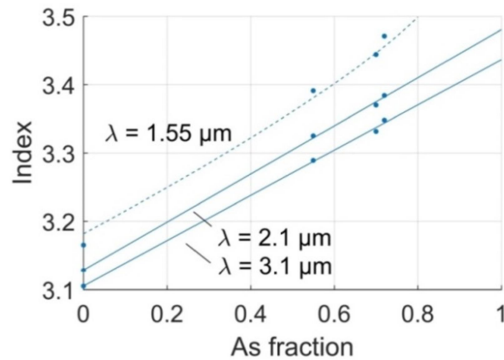


Figure 5-8. Refractive index measured at 1.55, 2.12 and 3.1 μm vs. y . Experimental data (dots) are plotted against the model from [113] for $\lambda = 1.55 \mu\text{m}$ (dashed line) and a linear fit for $\lambda = 2.1$ and $3.1 \mu\text{m}$ (full lines). Points for $y = 0$ are taken from [114].

Discussion

Experimental accuracy

Random errors

The uncertainty on grating period is given by (5.9). The position of diffraction peaks were determined by a Gaussian fit, with a precision of 0.01 to 0.001° , depending on the peaks size and quality. This corresponds to an uncertainty on grating period $d\Lambda = 0.01 \text{ nm}$ for the first diffracted order of a grating of period $1 \mu\text{m}$ (assuming $d\theta = 0.001^\circ$), and $d\Lambda = 0.06 \text{ nm}$ for the second diffracted order (assuming a smaller, noisier peak, $d\theta = 0.01^\circ$). All measurements were repeated, and the actual standard deviation was in the range of 0.1 nm . This discrepancy between expected and actual uncertainty may be explained by inhomogeneity of pattern along the surface. This leads to a 0.3×10^{-3} error bar on the effective index according to (5.10).

The coupling angle was determined in each measurement with a precision of 0.01° , which leads to an uncertainty of 9×10^{-4} on the effective index. The comparison of repeated measurements yields an uncertainty of 0.5×10^{-3} . This may be explained by local variations of the grating filling factor and depth.

#	PL (nm)	da/a	x Ga	y As	N (λ = 1.55 μm)	N (λ = 2.12 μm)	N (λ = 3.1 μm)
1	1395	-0.0025	0.33	0.72	3.470		3.348 ^{13,14}
2	1395	+0.0020	0.33	0.72	3.472		3.349 ¹³
3	1395	n.m.	0.33	0.72		3.384	
4	1346	n.m.	0.35	0.70	3.445		3.333 ^{13, 14}
5	1346	-0.0170	0.35	0.70	3.444		3.330 ¹³
6	1346	n.m.	0.35	0.70		3.370	
7	1266	n.m.	0.24	0.55	3.391		3.289 ¹³
8	1266	+0.00078	0.24	0.55		3.325	

Table 5-1. Physical properties and measured indices of the studied samples. The lattice mismatch was measured by X-ray diffraction. Ga and As fractions are deduced through the model presented in [138]. Samples of same composition come from the same wafer. Lattice mismatch was assumed to be homogeneous along each wafer. Photoluminescence was measured on all samples and was found to be homogeneous along each wafer.

Systematic errors

In order to estimate the impact of the thin layer of photoresist on the effective indices, we performed a set of measurements on a sample covered with a thin photoresist grating. Then we etched it shallowly, removed the resist and took a new set of data. The estimated thickness diminishes by 11 nm. This is in agreement with a profilometry of the etched grating depth, yielding 15 nm. The estimated core index is raised by 0.7×10^{-3} , i.e. less than the possible variation of twice the experimental error. Thus we conclude that the resist has negligible impact on the effective indices.

Finally, the uncertainty due to the composition prevails. This point is developed further in the next section.

¹³ Measurement taken at $\lambda = 3.14 \mu\text{m}$

¹⁴ Measurement taken at $\lambda = 3.17 \mu\text{m}$

Comparison with literature

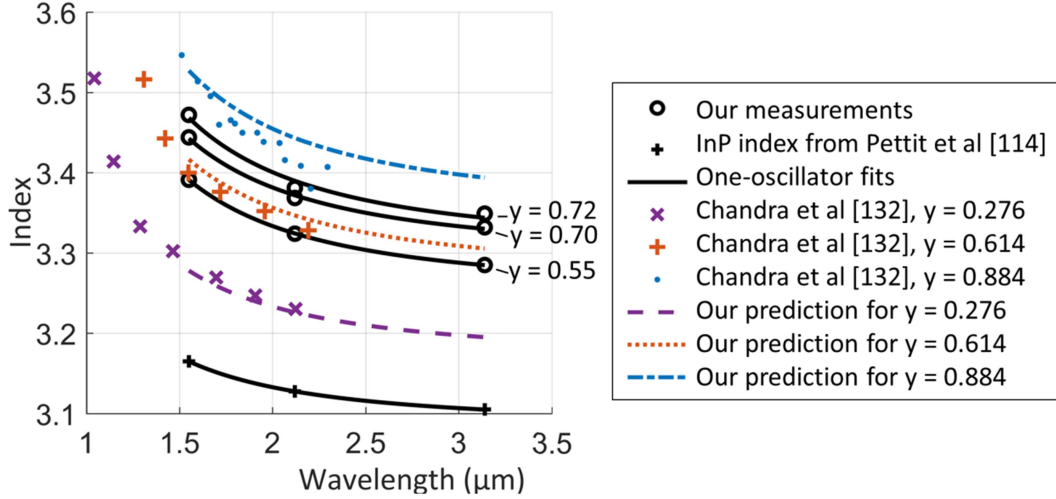


Figure 5-9. Refractive index of InGaAsP lattice-matched to InP vs. wavelength. Besides displaying our experimental data and those reported in literature, we linearly interpolate all of them with a one-oscillator fit for $y = 0, 0.276, 0.55, 0.614, 0.70, 0.72,$ and 0.884 .

Figure 5-9 shows the refractive index versus wavelength. We interpolate data as a function of wavelength and composition and show that our interpolated model is in agreement with previously measured values of index up to $2 \mu\text{m}$ [132]. The black circles indicate our experimental data for $y = 0.55, 0.70$ and 0.72 , plotted against a one-oscillator fit [112,115]:

$$n^2 - 1 = \frac{E_0 E_d}{E_0^2 - E^2} \quad (5.11)$$

where E is the wavelength energy in eV, E_0 is the position of absorption line in eV and $\pi E_d/2$ its strength. Fit parameters, presented in table 5-2, are extracted by a linear regression between $(n^2-1)^{-1}$ and E^2 . In order to expand the range of compositions in our interpolation, we add to this dataset the index of InP ($y = 0$), known from [114]. It is also plotted against a one-oscillator fit (parameters are also in table 5-2). We linearly interpolate between our one-oscillator fit models as a function of As molar fraction, from InP ($y = 0$) to the highest As fraction in our data ($y = 0.72$). Then we compare this interpolation to published index values between 1.55 and $2.1 \mu\text{m}$ [132]. Series of points in color show experimental values from [132], where $y = 0.884, 0.614$ and 0.276 (blue dots, orange +, purple x respectively). Curves of the same colors show the refractive index for these compositions predicted from

our interpolation. For data inside the extreme values of As fraction used in this model, our calculation is in agreement with published values.

y (As)	E_0 (eV)	E_d (eV)
0.72	2.550	25.36
0.70	2.648	26.12
0.55	2.759	26.52
0	3.434	29.29

Table 5-2. Parameters of the one-oscillator fit [112,115] inferred from the index measurements. Parameters are extracted by a linear regression from $(n^2 - 1)^{-1} = (E_0^2 - E^2) / (E_0 E_d)$, where E is the wavelength energy in eV. Data for InP ($y = 0$) is taken from [114].

The deviation of our measurements with respect to literature and to a linear fit is in the range of 1×10^{-2} to 2×10^{-2} . Variations of the same magnitude can be observed between [132] and [113] (figure 5-9), and in previous publications [129]. These differences are most likely due to deviations from the ideal lattice-matched case, inducing variations in composition as observed by [128].

This remaining uncertainty is not so much due to lack of information on composition as to the lack of comparable data in literature. Individual atomic fractions of samples may be known accurately, but refractive index has only been measured as a function of As fraction. By plotting and comparing values against this parameter only, we intrinsically lose information. No precise measurement of index with respect to all atomic parameters exists to our knowledge. To increase accuracy of our work, the best strategy would be to have access to a wider range of lattice-matched compositions in order to increase the precision of a linear fit, assuming that variations in compositions of individual samples are random.

Conclusion

We have measured the material index of InGaAsP for a range of compositions and wavelengths, outside of the scope covered by literature. In the range where data has already been published, agreement between our measurements and known values is good. Experimental error is estimated to be in the range of 1×10^{-3} . The highest uncertainty comes from samples composition, and could be decreased statistically by repeating measurements on a larger collection of nominally identical alloy layers.

These measurements allowed us to establish the waveguide structure presented in chapter 3.

6. Fabrication

This chapter reports on the fabrication efforts made during my PhD, aiming at developing key building blocks for the DOPO. Clean room processes depend on physical understanding as well as on a myriad of experimental details, so this chapter is kept as concise as possible while providing useful pointers for future developments. I tried to maintain a balance between a presentation of fabrication choices and improvements, explanations of the physical processes involved and a practical manual. The main fabrication objective of my PhD was etching and contacting ridge waveguides to obtain diode-OPO structures. At variance with common laser diodes, this design requires deep etching (3 to 5 μm) and perfectly controlled ridge width. This pushed us to develop ICP-RIE processes (Inductively Coupled Plasma – Reactive Ion Etching) with important etching depths and good control of verticality. Such work was undertaken in the Plateforme Technologique Amont (PTA) in the CEA Grenoble. These processes had not been developed in this clean room before my arrival, and they build a strong foundation for future fabrication of waveguides or other optical structures at the PTA. Fabrication of grating couplers on InGaAsP/ InP was performed at Paris Diderot University and is presented in chapter 5.

Fabrication overview of ridge lasers

The general fabrication process of ridge lasers is shown in [figure 6-1](#). Firstly a mask is defined with lithography and metal deposition (a), then pattern is transferred to the epitaxial layers (b), after which the insulator is deposited and opened either by planarization or lift-off (c). Finally contacts are deposited (d). If the ICP-RIE mask can be used as a contact, steps (c) and (d) can be skipped. After ridges are defined, the chip is cleaved so the structure acts as a Fabry-Perot resonator.

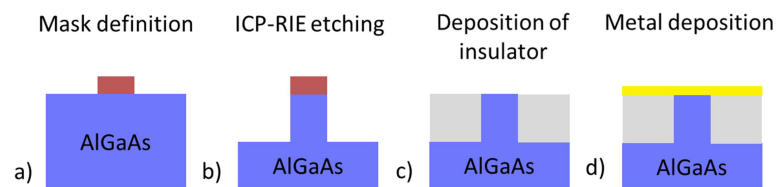


Figure 6-1. General overview of ridge lasers fabrication. a) Deposition and definition of a mask, b) Structure etching, c) Deposition of insulator, d) Deposition of contacts. Lithography and lift-off steps are not shown.

Choice of etch mask

Since this procedure was new in the PTA cleanroom, we explored various possibilities for ICP-RIE etching. The different types of etch masks that we experimented are presented in [figure 6-2](#), along with the related fabrication processes. The simplest way to define an ICP-RIE mask is to use patterned resist (a). Resolution and roughness are optimal, since theoretically they are only limited by the resist profile that is transferred to the material during the etching. Furthermore, limiting the number of fabrication steps lowers the probability of pattern degradation. However, the etching depth is limited by the resist thickness and etch selectivity. A metal mask (b) provides higher etch depths, but is intrinsically rougher since metal clusters in grains of diameter dictated by temperature during deposition, around 30 nm in our case. Amorphous materials do not have this intrinsic limitation. A SiN mask defined with resist (c) is in principle the best candidate for smooth masks usable in our depth range. A SiN mask defined with metal (d) allows one to achieve even greater etch depths, but potentially at the expense of on profile quality.

Only by using metal as a mask (b) can we directly contact the structures after etching. In the long term, the ideal candidate to minimize propagation losses in deeply etched structures would be to define ridges with resist (a) or SiN defined by resist (c). But even though we experimented with all processes shown here, we focused on metal masks (b) in order to contact structures more quickly in the short term. We will focus on this process, straying away from it to present other options from time to time.

Optical lithography

In clean room fabrication, lithography is the step that requires the most careful manipulation and knowledge of experimental tricks. A complete guide of lithography processes is out of the scope of this chapter, but we will warn against common mistakes and explain how to adjust a process for similar requirements. Resists usually contain polymer chains dissolved in solvent, able to crosslink under the influence of light, an electron beam, or temperature. In order to define ridges, we

used optical resists AZ1512HS or AZ5214E. They soften around 120°C and start cross-linking around 140°C. Solvent evaporates around 100°C.

Most positive¹⁵ photoresists have a null or positive¹⁶ profile. Physically, this originates in the absorption of the resist layer: the deeper the propagation of light, the weaker its effect. This can be used to achieve negative profiles with image reversal (IR) photoresists. As a consequence, the weaker the exposure dose, the more slanted the profile will be, whether in positive or negative mode. The slope is also affected by baking steps and development times.

The fabrication steps of lithography go as follow.

Samples of 5 mm to 1 cm of side are cut from the wafer. They are cleaned in an ultrasonic bath of acetone, then isopropanol, for 5 minutes. Rinsing in water is not necessary. All fluid, whether evaporating quickly or not, should be evacuated with a nitrogen gun to avoid contamination on the sample. If traces of resist from a previous lithography remain, cleaning them may prove difficult. Generally speaking, a SEM observation, a baking step or the plasma in a dry etch can cause unwanted cross-linking or burning, after which the resist may undergo dark erosion or not be dissolvable. To eliminate resist before a new deposition, one can use an O₂ plasma or remover.

Samples are then placed on a hot plate at 120°C for at least 3 minutes, to desorb water on the surface. This step is optional if samples are just leaving an isopropanol bath, but we recommend it systematically to improve reproducibility, since water is re-adsorbed in 5 to 20 minutes in a clean room environment. We do not recommend dehydration at higher temperature if the sample has already undergone lithography: any trace of remaining resist would burn and become virtually impossible to remove.

¹⁵ A resist is positive if the exposed part disappears at development and negative otherwise.

¹⁶ We call A-shaped profiles positive, and V (or re-entrant) profiles negative.

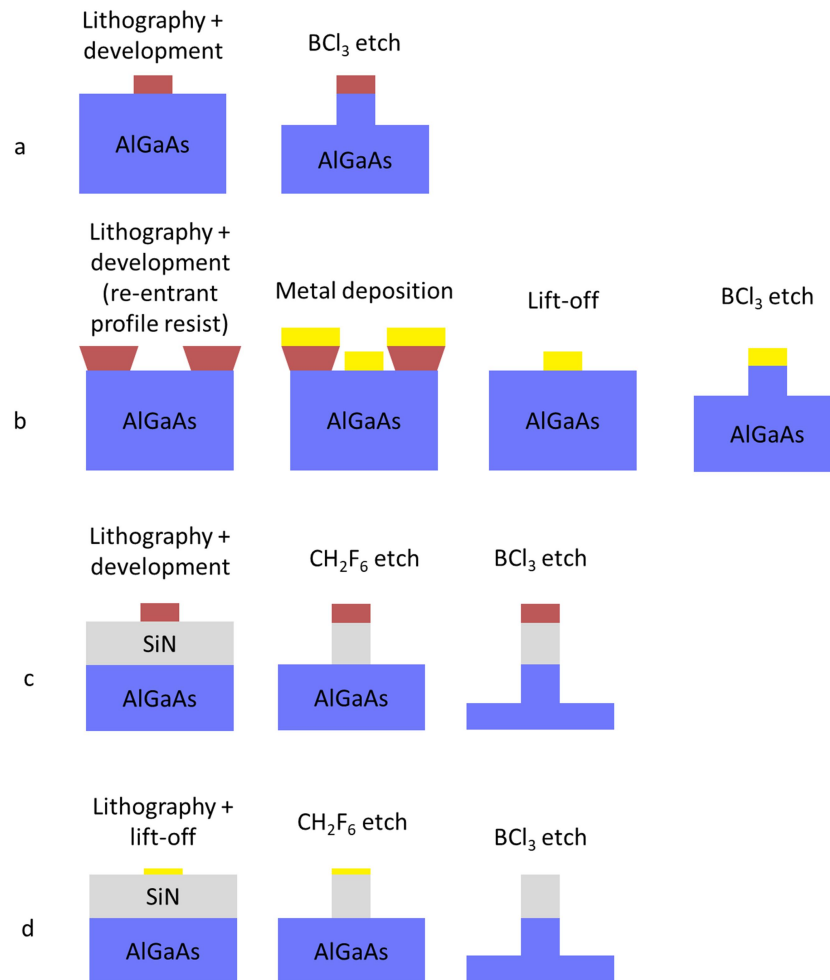


Figure 6-2. General view of the processes used to define AlGaAs structures. (a) Resist mask, (b) Metal mask, (c) SiN mask defined with resist, (d) SiN mask defined with metal.

After dehydration, an adhesion promoter is spin-coated on the surface in order to make it hydrophilic. The choice of promoter is crucial: among the various types available to us (HMDS, Ti prime, VM632), only one (Ti prime) was effective enough to prevent the delamination of our long and thin patterns (meant for the definition of waveguides). Furthermore, we would like to point out that HMDS is not meant to be spin-coated: liberation of NH_3 at the sample surface can cause local cross-linking and impede complete development. However, this is likely less of a problem with thin resists. We normally spin-coated resists AZ1512HS or AZ5214E at speeds yielding a thickness of $1.2 \mu\text{m}$. The choice of resist thickness is usually a compromise. Pattern quality and resolution improve with smaller thickness and shorter exposure wavelength, but later steps may impose a minimal thickness. In

our case, optical resists need to be at least 1 μm thick to either withstand an ICP-RIE of 3 to 4 μm or allow the lift-off of 250 nm of metal without residues.

Many problems can arise during spin-coating, the most common being the formation of “comets” on the sample surface: local defects cause a deformation of resist around them and form lines leading away from the sample center. This can be due to residual particles on the sample surface, bubbles in the resist (if it was shaken) or particles in the resist (if it is expired or contaminated). To diagnose the problem, one should carefully observe the sample under a microscope before and after each step of lithography. Even without defects, thickness variations occur since resist accumulates on the sample edges during spin-coating. Resist is thicker on the edges, where an especially heavy bead appears. This effect can be mitigated with the choice of adequate speed ramps, but it is always present and particularly marked on small, non-circular samples. During contact lithography, this edge bead creates a gap between mask and resist surface on the sample center, which deteriorates the quality and resolution of pattern. It can be removed by selective lithography and development, or manually with a dry cotton swab, but solvents should be avoided since they can affect the remaining resist. For non-contact lithography, edge bead is not a problem but one should be aware of thickness variations when adjusting the focus.

After resist deposition, we soft bake the sample at 110 °C during 90 seconds for AZ5214 and 100°C during 50 seconds for AZ1512HS. The solvent evaporates, which has the effect of increasing resist adhesion, limiting sticking to the mask, minimizing dark erosion during development and preventing bubbling by evaporation.

Photoresists are exposed with a MJB4 aligner. We also experimented with laser lithography (Heidelberg μPG 101), but found that even with optimal resolution settings, striations corresponding to laser passages were visible on the exposed resist. Furthermore, focal depth is extremely limited and the smallest protuberance or trace of resist on the back side brings the sample out of horizontal plane and out of focus.

The correct dose for photolithography depends on the sample reflectivity, so there may be small variations between Si and AlGaAs/GaAs wafers. Substrate reflectivity has important effects on exposure. In the case of a transparent top layer, light can be reflected between the resist and the underlying layers, effectively exposing the resist from below, which leads to delamination during development. On the contrary, highly reflective substrates can lead to the formation of standing waves which give

a staircase appearance to the developed resist. The exposure dose is chosen to provide the clearest-looking pattern after development and the most useful profile: negative profile for a lift-off, straight flanks for an ICP-RIE. We exposed all samples in hard contact mode and set the distance between mask and sample manually, by observing interference fringes in the resist through the aligner microscope. We carry out firstly an inversion bake of AZ5214E for 2 minutes on a hot plate at 120°C, and then a flood exposure¹⁷ during 33 seconds.

Samples are developed for 40 seconds in AZ developer diluted in water (1:1) and rinsed abundantly.

Mask roughness

Resist roughness is critical in fabrication of ridge lasers since they cause propagation loss by scattering at sidewalls. It is determined by a number of factors. An intrinsic noise limit is set by the size of polymer chains: typically this minimal roughness is about 50 nm for optical resists of thickness in the μm range, and 15 to 20 nm under optimal conditions for the MAN family of electronic resists. Last generation resists like HSQ achieve resolution and roughness in the nm range. However, the choice of lithography parameters can degrade the pattern. The quality of mask used for contact lithography also has a direct effect on minimal feature size and quality. Optical masks progressively degrade and should be changed after a few years, depending on their frequency of use.

Figure 6-3 shows resist (AZ5214) and metal mask roughness, and the resulting dry etches. The observed roughness of optical resist (figure 2.a) is in the range of normal values for this family. Metal masks (b) show a granularity with roughness of 20 to 50 nm. Variations in the direction of propagation seem to be directly due to the transfer of pattern roughness (d). (c) shows the result of an etch using a resist mask. The sidewall is observed at a steeper angle, so irregularities appear more pronounced. Flanks observed from the same angle (c, d right) show lower roughness with resist masks.

¹⁷ Exposure of the whole sample.

Figure 6-4 shows a resist mask on SiN and the resulting SiN mask after a dry etch. A roughness of a few tens of nm is visible, seemingly directly transferred from the pattern in resist. Heating the resist over its softening point after exposure (“reflow”) can smooth out irregularities. Sidewall profile is modified: the resist maximizes its surface of contact with the substrate and minimizes the surface exposed to air, which leads to flat lens shapes. Unfortunately, we have observed undulations of the resist provoked by thermal reflow (figure 6-5). Plasma reflows have been proposed as an alternative to avoid undulations [143], although our attempts did not show significant improvements.

ICP-RIE etching

Requirements

As said before, our goal when developing ICP-RIE protocols was to achieve etching depths over 3 μm and vertical sidewalls with controlled angles. We aimed for smooth sidewalls to limit propagation losses. We also tried to achieve low selectivity between AlAs and GaAs. Indeed, the DOPO waveguides contain layers of high Al content (80 %) and a core made of various compositions (10% to 25% Al). Unequal horizontal etches would create waveguides that deviate from the ideal vertical etch that allows us to reach phase matching. They would also create a staircase profile in the vertical direction. In principle, variations in the vertical direction do not result in propagation losses, however they increase the waveguide surface and might increase mechanical fragility. Both these effects can increase propagation losses. Furthermore, the protocols developed will also be used by the INAC team for vertical Bragg resonators. In these structures, light propagates in the vertical direction and any selectivity of AlAs over GaAs induces important losses.

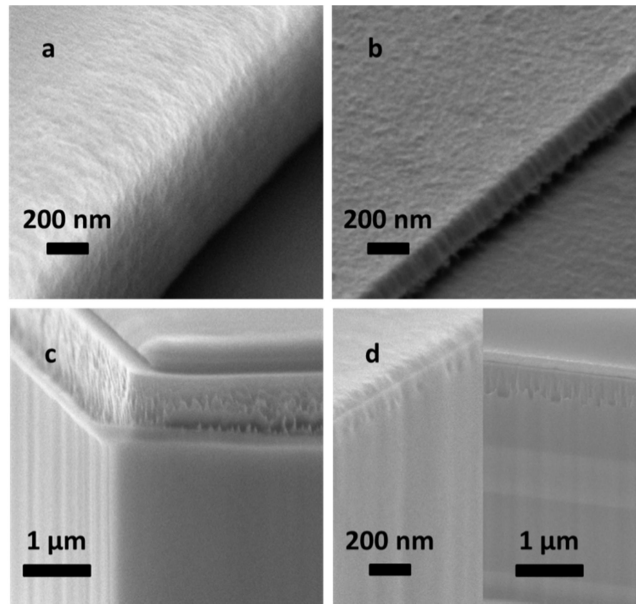


Figure 6-3. Masks used for AlGaAs dry etching and resulting structures. a) Sidewall of a photoresist mask on substrate before etch. b) Sidewall of a metal mask on substrate before etch. c) Result of ICP-RIE etching with a photoresist mask (we see from top to bottom : the remaining re-entrant photoresist, the attacked sidewalls of etched substrate, the vertical sidewalls of etched substrate). d) Outcome of ICP-RIE etching with a metal mask (in the two photographs shown side by side, one at grazing incidence with respect to the sidewall, one facing the sidewall, we see from top to bottom : the remaining metal mask, slight asperities on the top of the etched substrate, the vertical sidewall; color differences in the vertical sidewall are due to composition variations).

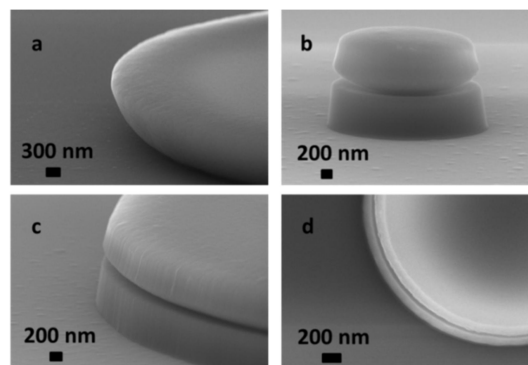


Figure 6-4. SiN dry etching: a) photoresist on SiN, b) to d): SiN etched mask. Photoresist is not removed and GaAs not etched. The gap between resist and SiN is due to the re-entrant profile of the photoresist before etching.

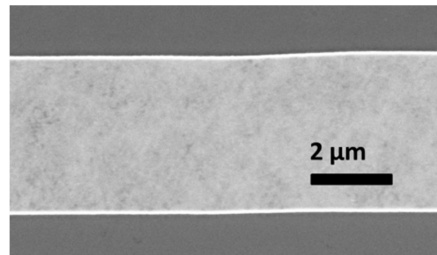


Figure 6-5. Metal mask undulation, observed after a thermal reflow of the resist and a lift-off

Principle

ICP descends from Reactive Ion Etching. Both schemes are presented in [figure 6-6](#). In a RIE chamber, reactive gas is injected between two electrodes. The sample is placed on the lower one. An RF signal is applied between electrodes, and chemicals in the gas ionize under this field. Electrons strike the bottom electrode more quickly, charging it negatively. Ions are therefore accelerated towards the bottom electrode where the sample is placed. At equilibrium, the system reaches a potential between electrodes called the self-bias. Literature often reports self-bias rather than imposed RF voltage, since the ions acceleration depends on the former. In an ICP chamber, ions are placed inside a RF coil which dissociates them. The sample is placed on an electrode that can be biased independently. In this scheme, plasma density and acceleration can be controlled independently, providing a better control of the etch mechanism. The coil voltage is usually called ICP and the bottom electrode RF for historical reasons.

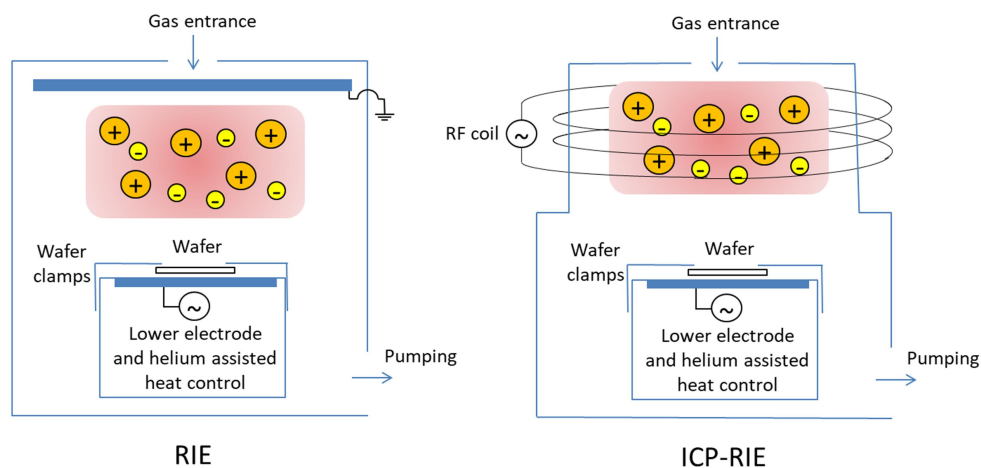


Figure 6-6. RIE and ICP-RIE chambers

Etching mechanisms

Etching is the result of both physical and chemical processes. Four main etch mechanisms have been identified (figure 6-7) [144]. They are global descriptions that entail many different physicochemical reactions, and the reality of a RIE is usually a mixture of all 4 processes. In a simple description, physical and chemical etching would be independent. On one side, ions accelerated to the substrate dislodge atoms in a purely physical and anisotropic way (sputtering). On the other side, species in the plasma chemically react with the sample. Like in every chemical etching, profiles can be anisotropic, dependent on composition, or proceed along crystal planes. Two other etching mechanisms are commonly considered, involving an interaction of physical and chemical processes in ion-enhanced chemical etching. In an ion-enhanced energetic process, impinging ions modify the surface by various mechanisms, raising its temperature or modifying atomic configurations. These modifications make the surface more sensitive to chemical attacks and, as a consequence, etching proceeds mostly in the vertical direction. Lastly, in an inhibitor protected-sidewall process, a protective layer forms on exposed surfaces. Impinging ions destroy this layer only on horizontal surfaces, making the etch reaction proceed mostly vertically. In both ion-enhanced etch processes, etching is mostly anisotropic, but sidewall quality can be as high as in a purely chemical process and etch rates larger than for a purely physical etch. As a consequence, most RIE gas etchants are a mixture of chemically reactive species and inert gas. Adjusting the ratio of individual gas provides a control over the nature of the etch.

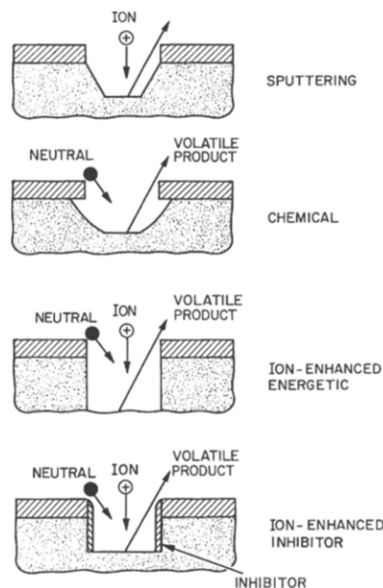


Figure 6-7. Main processes involved in RIE etching.

Choice of chemistry

We used a $\text{BCl}_3/\text{SiCl}_4/\text{Ar}$ mixture for all AlGaAs etches. Chlorine chemistries, commonly based on Cl_2 , are used since the late 90's to etch GaAs/AlGaAs [145–148]. BCl_3 is often added to Cl_2 in order to lower chemical selectivity between AlAs/GaAs [149,150]. This effect originates in the high sensitivity of AlAs (or AlGaAs with high Al content) to oxidation. A resistant aluminum oxide layer, only removable by sputtering, can form on its surface while the rest of the structure stays vulnerable to chemical etching. The final result is rough walls with abrupt variations. BCl_3 prevents this by acting as a strongly reducing agent [151]. Water and air are common oxidizers, and to prevent contamination ICP-RIE chambers often have a load-lock system to protect chamber walls from room atmosphere. SiCl_4 is often used as a replacement of Cl_2 , since it has been demonstrated to offer lower roughness, more anisotropic etching and residue-free surfaces [152]. Being more recent, $\text{SiCl}_4/\text{BCl}_3$ mixtures haven't been as studied as Cl_2/BCl_3 . In a BCl_3/Cl_2 mixture, BCl_3 and Cl_2 don't have strictly equivalent roles. BCl_3 provides less reactive species and seems to have an intermediate role between chemical etchant and activator for Cl_2 [146]. Unfortunately, no similar study of the roles of BCl_3 vs. SiCl_4 exists to our knowledge. Argon, as an inert gas, acts as a purely physical etchant. Under-etching decreases with higher Ar content in similar chemistries [146,149], indicating its origin as a chemical process.

Results

The optimal parameters that I found for AlGaAs dry etches are presented in table 6-1. Etch rate under these conditions is in the range of 250 nm/min. We achieved, as desired, deep etches with controlled verticality. Sidewalls are smooth and chemical selectivity is low or inexistent. Figures 6-8, 6-9 and 6-10 show the result of ICP-RIE etching on wafers of various compositions. We achieve etching depths up to 20 μm , with a control of sidewall angles of 1° . Etch rate under these conditions is approximately 250 nm/min. The parameters used for SiN etches are presented in table 6-2. Figure 6-4 presents SiN masks obtained by these means. Etch rate under these conditions is approximately 150 nm/min.

RF power	ICP power	BCl_3 flux	SiCl_4 flux	Ar flux	Pressure	Temperature
150 W	50 W	5	10	5	5 mT	30°C

Table 6-1. Typical parameters used for ICP-RIE etches of AlGaAs.

RF power	ICP power	CH ₂ F ₂ flux	SF ₆ flux	Ar flux	Pressure	Temperature
50 W	250 W	25 sccm	5 sccm	40 sccm	5 mT	20°C

Table 6-2. Typical parameters used for ICP-RIE etches of SiN.

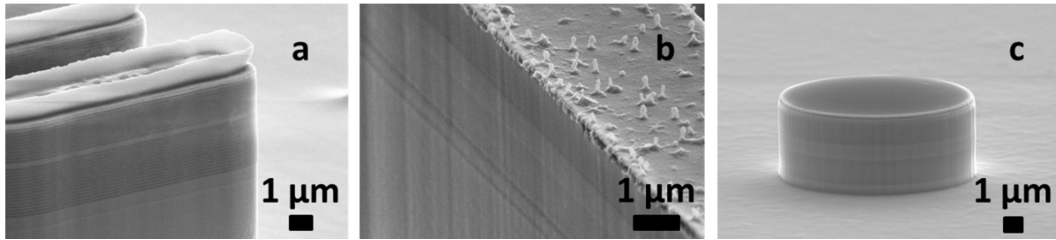


Figure 6-8. Examples of large (>1 μm) structures etched by ICP-RIE. (a) GaAs cavity between AlAs/GaAs Bragg mirrors, (b) DOPO structure, (c) DOPO structure.

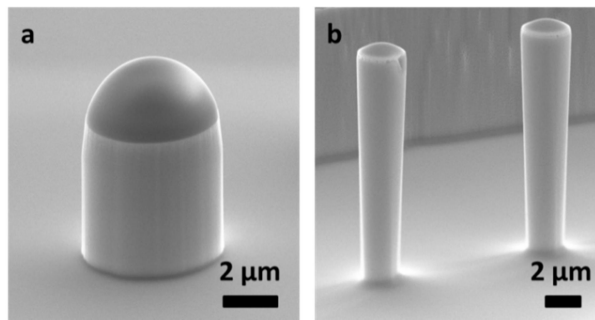


Figure 6-9. Results of ICP-RIE etching of GaAs with the parameters given in table 6-1. (a) Etching temperature: 30°C; angle: 0°; depth: 5 μm. (b) Etching temperature: 45°C; angle: 1.5°; depth: 15 μm.

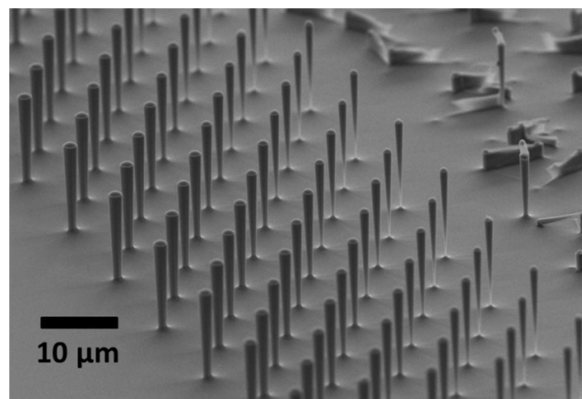


Figure 6-10. Example of structures etched by ICP-RIE. Total height is 12 μm. Mask size decreases from left to right.

Choice of parameters

As mentioned above, the ratio of individual gas fluxes provides an adjustment between chemical and physical etching. We experimented with different values according to physical intuition and chose optimal parameters empirically. The low ratio of Ar to other gases seems to indicate a mostly chemical process in nature, likely helped by an ion-enhanced inhibitor process according to SEM observations (see section 6.5.7). The total flux was chosen to be comparable to other processes. A flux too low would make the plasma sensitive to residues on the chamber walls and decrease reproducibility. Pressure is in the middle to low range of typical values for this process. It was set that way to reduce the number of ion collisions in the plasma, which yields more vertical etches. The effect of pressure on the etching rate depends on the nature of the etching [153]. Temperature has a marked influence on our process, particularly on etching rate and under-etching. Figure 6-9 shows the result of otherwise identical etches performed at 30°C (a) and 45°C (b). Both vertical etching and attack of sidewall passivation layers are activated by temperature: the etching rate increases from 160 to 460 nm/min and under-etching goes from 0 to 1.5°. Sidewalls are smooth on both structures. Temperature offers a fine control of verticality. With the high aspect ratios and low roughness achieved, my protocol might also be used to reproduce photonic trumpets in the PTA cleanroom. Figure 6-10 shows trumpet-like structures etched in similar conditions. Sidewall roughness improves with lower ICP power but lowering it further makes plasma onset difficult. Future users might implement a longer procedure: initialize the plasma at high power then progressively adjust values. Bias stabilized around 360 V with the conditions presented in table 6-1. Sidewall roughness worsens at lower RF power, which goes against a qualitative understanding and comparable results in literature. Surface quality would probably benefit from gentler etching under lower bias [154]. We observe higher chemical selectivity at lower RF powers, which sets a lower boundary on this value. Qualitatively speaking, this corresponds to an etching more chemical in nature at low ion accelerations.

Control of the environment is critical in a RIE chamber. The etching result is not only determined by set parameters but also by the whole chamber chemistry and geometry. Processes can be greatly impacted by residual species on chamber walls, which is why a conditioning of the same duration as the actual etching is recommended to improve reproducibility. The sample size and the nature of the supporting wafer impacts the available chemical species in the chamber. This is especially true for III-V processes where samples are often cut in tiny pieces because

of their high price. We used crystalline Si wafers during conditioning and SiO₂ wafers during etches. The nature of the supporting wafer is critical, as is shown by the change in results when we replace a SiO₂ wafer with a Si one: sidewalls slant go from 0 to 30°, Al-rich layers start to lift off and the bias goes from 350 to 420 V. Heat control is also crucial. As shown earlier, etching results depend strongly on temperature. Samples are exposed to a flux of He on their lower side. This gas provides a good thermal contact to a cryogenic liquid kept at controlled temperature. Clamps maintain samples in place and prevent He from escaping into the chamber. A simple modification of the clamping mechanism can allow some He to mix with the plasma, modifying the nature of the etch. Figure 6-11 shows the result of an etching in similar conditions on the same sample, with (a) and without (b) a small He leak in the chamber.

Lastly, it is commonly known in the field of dry etching that results depend on feature sizes and that a process should be developed for a certain pattern size. We observe indeed an effect of feature size on surface quality (figure 6-12). Variations are not due to local inhomogeneities. All structures shown are part of the same sample, etched in one run, and are distant of 100 μm at the most. Smaller (diameter < 2 μm) pillars show excellent sidewall aspect, while on bigger (diameter > 15 μm) pillars notches and drips have developed. While this effect is well known, we haven't found a theoretical justification for it.

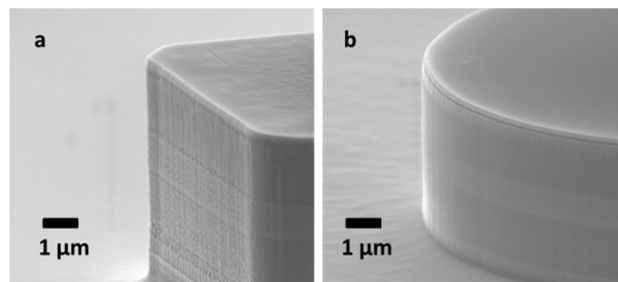


Figure 6-11. Etch in typical conditions with (a) and without (b) helium leak in the chamber.

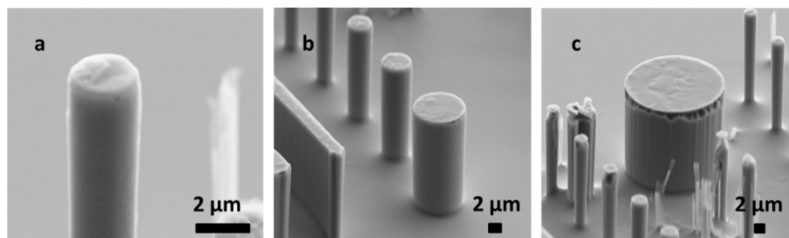


Figure 6-12. Result of a single ICP etching on pillars of various sizes. All observed structures are located in a zone of radius 100 μm. Notches and drips are visible on the bigger pillars.

Passivation layer

Several research groups have reported an ion-enhanced inhibitor process during chloride chemistry etches, by promoting a passivation layer with the addition of N₂ [155–158], O₂ [159,160] or H₂ [161]. This etching mode can provide extremely vertical and smooth sidewalls with high etch rates. Several elements indicate that this mechanism occurs during our ICP process. SEM observations show an external layer present on sidewalls, disappearing at high temperatures or whenever access to reactants is inhibited (figures 6-13 and 6-14). In addition, anisotropy and etch rate fall abruptly whenever the SiO₂ supporting wafer is replaced with a crystalline Si one. We see a clear dependence of the passivation layer quality on etch temperature. Figure 6-13 shows the impact of temperature on etch depth and sidewall aspect. At low temperature (a and d), a thick layer is present, especially visible at the structures feet. At higher temperature (c and f), the outer layer is attacked in places. Its attack and removal may be chemically activated with temperature. The local availability of reactants also seems to be a factor. This is visible in figure 6-14, an early ICP of AlAs/GaAs Bragg mirrors, where the external layer is not present between two close pillars. The origin and nature of passivation layer depend on the chemicals present in each process, and they are most often not well understood in literature. Early work has proposed that it may originate in carbon from resist masks [147]. More recently, analysis for O₂-promoted sidewall passivation points to a SiO_x layer [158,162]. [151] and [163] suggest the formation of polymers in N₂-promoted passivation. [157] suggests the formation of resistant Ga-N and As-N bonds on the surface. Comparison between individual processes is delicate. The exact surface composition likely depends on residues on chamber walls, etch gas, wafer composition and environment. In our case, a SiO_x layer is most likely, since reactants are readily provided by the SiCl₄ gas and the SiO_x wafer. Another indication is the sharp modification of etching mode when switching to pure Si wafers.

Removal of mask residues

After etching, the remaining metal mask is removed with nitric acid. If resist was used as a mask, it is cleaned with acetone and isopropanol. Samples are then cleaved in chips of 1 to 3 mm of width. A SEM observation of a cleaved facet is shown in figure 6-15.

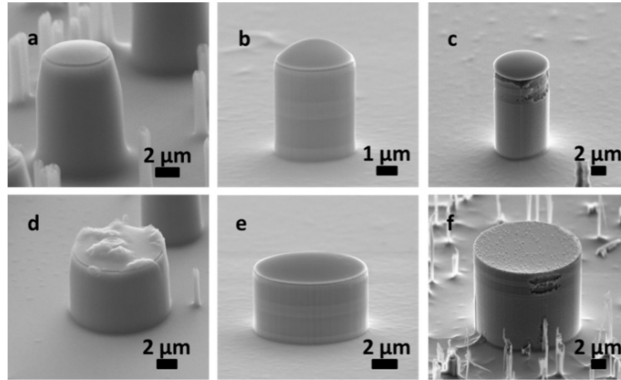


Figure 6-13. Result of ICP etches in typical conditions, at temperatures of 20°C (a-d), 30°C (b-e), 45°C (c-f)

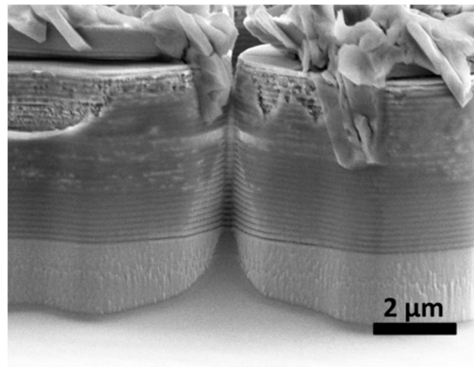


Figure 6-14. Early example of ICP etch. Two disks are etched with a near 0 gap between them. Availability of reactants influences the etch rate and formation of passivation layer. Indeed, the etch does not proceed until the bottom of the trench and the difference in color between center of the trench and exposed sidewalls indicates a variation in sidewall composition.

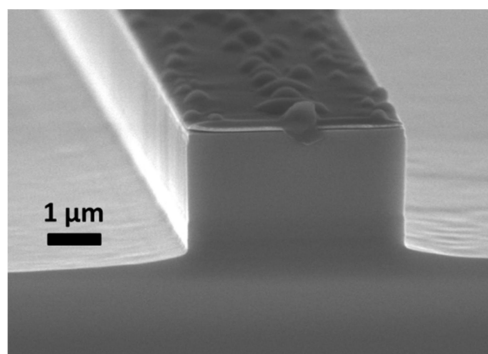


Figure 6-15. View of a cleaved waveguide facet before mask removal

7. Double-cavity DOPO

In the DOPO design presented earlier, laser and OPO cavities are one and the same. However, the best design parameters for efficient laser behavior often degrade nonlinear light conversion, and vice-versa. The choice of doping profile is particularly critical. In order to achieve an efficient electric injection in the laser, the dopants concentration should be high. But this introduces FCA losses for the signal and idler beams, reducing the conversion efficiency and generated power. As a result, dopants-induced losses are a bottleneck to reach the OPO threshold. Furthermore, wide variations of temperature provide tunability for the OPO, but the laser efficiency is expected to degrade with increasing temperatures.

To get rid of these problems, we can separate the two cavities. One way to go about this approach is to build separately the laser and nonlinear material and to bring them together using heterogeneous integration. However, this method requires extensive work in order to fix and align the two components. Other methods exist like selective-area epitaxy [164].

Since the AlGaAs platform already provides efficient lasers and nonlinear conversion, an all-integrated design is also practicable, with no subsequent alignment necessary. This orients our choice towards vertical coupling: cavities are grown on top of each other and coupled so that light can pass from laser to nonlinear medium.

Vertical couplers are typically used for the integration of lasers or detectors on an underlying chip. At the upper level, a material of smaller gap is used for light generation or detection, while the lower levels comprise a material of higher gap for light transmission and analysis. This scheme is also used for the integration of III-V laser on silicon chips, since Si lasers have yet to be demonstrated. Both systems are very analogous to our proposal: an efficient laser must be coupled to another waveguide, which cannot function as a laser itself, in our case because of absorption losses.

Choice of coupling method

The choice of the coupling method depends on the material used and on the modes supported by the structure. In this study, we explore the range of possibilities opened by the GaAs/AlAs/InAs system, and we base the design of the laser part on

already existing, high performance AlGaAs lasers at 1 μm (table 7-1). The detail of layers thickness and composition is not shown here for confidentiality reasons. In this structure, the fundamental mode at 1 μm has an effective index of about 3.36.

Layer type	Material
Top cladding	AlGaAs
Optical confinement (laser core)	InGaAsP
Quantum Well	InGaAs
Optical confinement (laser core)	InGaAsP
Bottom cladding	AlGaAs
Substrate	GaAs

Table 7-1. Data sheet of a typical AlGaAs laser

Regarding the waveguide where parametric conversion is to take place, the conversion efficiency is higher if the pump mode is of order 2 in the vertical direction. Additionally, high conversion efficiency is favored by high cladding / core index contrasts. This, coupled with the fact that we have to work with a higher-order mode, sets the maximum value of effective index in the waveguide at approximately 3.2.

Considering these constraints, we can examine different types of coupling and assess their compatibility with our system.

Evanescent couplers

In evanescent couplers (figure 7-1), light is mostly confined in the underlying waveguide. Its evanescent tail explores the area above it where a p-n junction has been brought to the gain regime. This scheme implies that the effective index in the laser part (p-n junction) is lower than in the buried part, otherwise the mode would predominantly stay in the top area. Unfortunately, in our case this is incompatible with indices ~ 3.36 in the laser and ~ 3.2 in the buried waveguide. Furthermore, the modal gain is limited by the small mode overlap with the gain region. This seems restricting, given the high intracavity powers necessary to reach the OPO threshold (~ 100 mW). Therefore, it appears that evanescent coupling is not the ideal choice for our system.

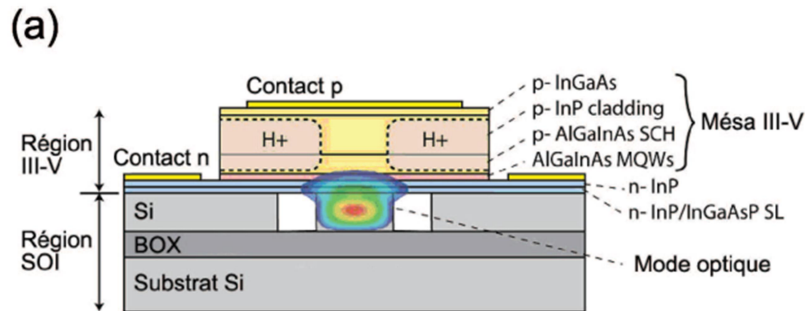


Figure 7-1. Example of evanescent coupling [165]

In other coupling schemes, light is transferred from one guide to the other, either by a grating (Bragg-exchange lasers) or by a variation of effective indices (adiabatic couplers).

Bragg-exchange

Bragg-exchange lasers have been extensively studied at CEA in Grenoble (figure 7-2). In these systems, a III-V gain material is coupled to an underlying silicon chip by a grating. Light propagates back and forth between the two waveguides. Compared to evanescent coupling, this method provides higher gain since the mode is fully inside the gain material half of the time. The grating also allows us to compensate for the mismatch in propagation constants between the two waveguides. It is a viable scheme, although transfer efficiency may suffer from variations in effective indices.

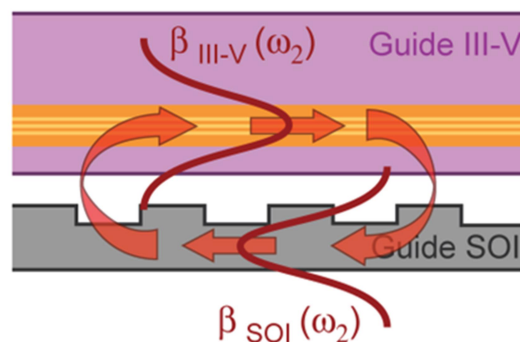


Figure 7-2. Bragg-exchange coupler [121]

Adiabatic couplers

Finally, in adiabatic couplers, the waveguides indices change along the direction of propagation (figure 7-3). Before the transfer region, the two effective indices are

different, and the mode sits mostly in the waveguide of higher index. Then they are modified along the direction of propagation, usually by changing the waveguides width: either the top waveguide's effective index is reduced or the bottom one is increased, so that the two effective indices become equal and mode coupling occurs. After the power transfer to the bottom waveguide, the initial situation is reversed: the buried waveguide has the higher index and contains most of the mode.

The laser modal gain is maximum, since light is fully confined in the active region before transfer. This design is also compatible with our indices: after an effective index of 3.36 in the laser section, index is brought down to ~ 3.2 or with a progressive width reduction. Furthermore, this design is very tolerant to variations of effective index due to fabrication, temperature changes or current injection. For these reasons, we chose to design a coupler based on this scheme.

Table 7-2 shows the summary of different coupling systems and their compatibility with our project.

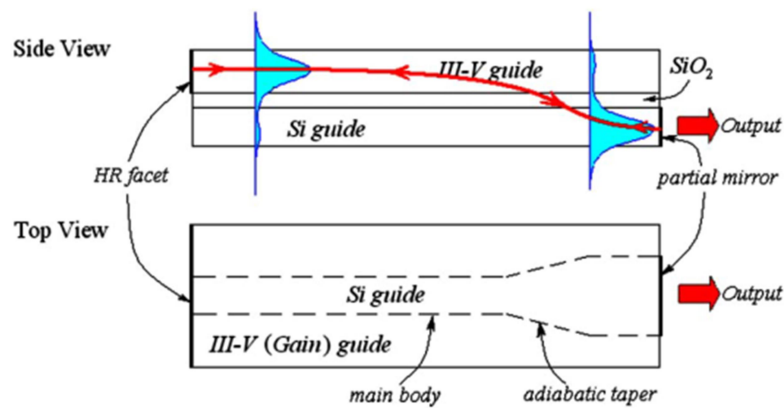


Figure 7-3. Adiabatic coupler. [166]

Type of coupling	Evanescent	Adiabatic	Bragg-exchange
Modal gain	☹️	☺️	☺️
Compatibility with the effective indices in DOPO	☹️	☺️	☺️
Tolerance	☹️	☺️	☹️

Table 7-2. Compatibility of different coupler types with the DOPO project

Adiabatic couplers physics in a nutshell

The above qualitative description is obviously incomplete, and the reader curious about the physics of this system can be interested in a quick explanation. The adiabatic coupler is a modification of the well-known directional coupler (or “resonant coupler”). In the latter, when two waveguides are brought together, the eigenmodes of the system are modified: instead of two individual modes, the system supports one symmetric and one antisymmetric mode. If light is injected only in the top waveguide, a superposition of the two supermodes is excited (figure 7-4). Since they don’t propagate at the same speed, the result is a back and forth propagation of the electric field between the two waveguides, at a period determined by the beat frequency between the supermodes propagation constants.

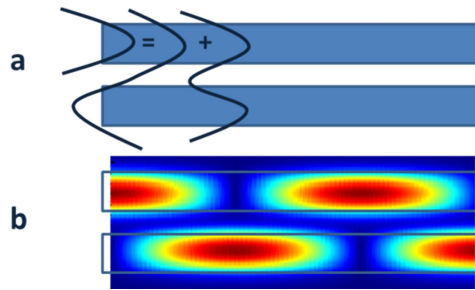


Figure 7-4. Resonant coupling. a) Introduction of light in a single waveguide. 2) Electric field intensity after the introduction of a Gaussian wave in the top waveguide

In the case of a 2D directional coupler, we can define a transfer length as [92]

$$L = \frac{\pi}{2\rho} \quad (7.1)$$

$$\rho = \sqrt{\rho_{21}\rho_{12}} \quad (7.2a)$$

$$\rho_{21} = \frac{1}{2}(n_2^2 - n^2) \frac{k_0^2}{\beta_1} \int_a^{a+d} \phi_1(y)\phi_2(y)dy \quad (7.2b)$$

$$\rho_{12} = \frac{1}{2}(n_1^2 - n^2) \frac{k_0^2}{\beta_1} \int_{-a-d}^{-a} \phi_2(y)\phi_1(y)dy \quad (7.2c)$$

where n_1, n_2 are the waveguide core indices, n is the index of surrounding material and $\phi_{1,2}(y)$ indicates the modal amplitudes in the transverse plane. If indices are equal, transfer between the two waveguides reaches 100% at every multiple of the transfer length (see figure 8-6).

In an adiabatic coupler, one or both guides indices are modified continuously (figure 7-5). Before (resp. after) transfer, the index mismatch δ is negative (resp.

positive) and the eigenmodes are similar to the modes of uncoupled waveguides. During transfer, as the index mismatch approaches 0, the eigenmodes approach the modes of a symmetric system. In order to transfer light from one waveguide to the other without loss of energy, the electric field should stay in the same eigenmode along the whole propagation length, with limited scattering to other modes. This description is obviously different from the resonant coupler case, where light injection necessarily excites a superposition of eigenmodes. A full description of this system is available in [167], along with quantitative criteria on the size and shape of taper length for optimal transfer.

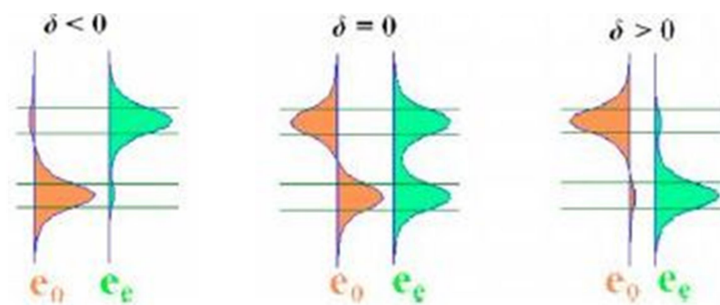


Figure 7-5. Eigenmodes in an adiabatic coupler. Index mismatch varies continuously from left to right. [167]

Adiabatic couplers offer a better tolerance, which is why they are more commonly used in III/V photonics or III/V on Si integration [166–171].

Figure 7-6 shows the fraction of light transferred from one waveguide to the other for both approaches. If their length is correctly set, resonant couplers transfer 100% of the power on a shorter distance, whereas adiabatic couplers show an asymptotic response. However, the period of a resonant coupler being determined by the effective indices of propagating modes, they are highly sensitive to variations in fabrication. As a result, they are mostly used in silicon photonics, which relies on high precision patterning of Si microstructures. Adiabatic couplers offer a better tolerance, which is why they are more commonly used in III/V photonics or III/V on Si integration [166–171].

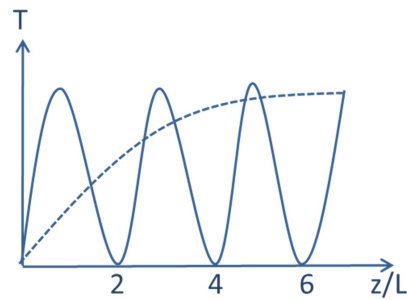


Figure 7-6. Transfer in a resonant coupler (full line) vs. adiabatic coupler (dashed line). L indicates the transfer length defined in (7.1).

Critical points

We have considered different coupling strategies and chosen an adiabatic taper as the best choice. Before designing the rest of the device in detail, we can single out some points critical to the operation of the DOPO source. These are the aspects that will dictate design choices for the rest of the device.

The first “hard point” is [spectral stability](#). Doubly resonant OPOs (DR-OPO) are more unstable than singly resonant OPOs, triply resonant OPOs even more so. To achieve a lower threshold, we choose a DR-OPO configuration, but for a more stable operation, the pump should not oscillate inside the OPO cavity. Concerning the laser, to avoid mode competition and instability, the pump should not return into the laser cavity after having explored the OPO region.

[Thermal behavior](#) and [contact geometry](#) are also expected to be critical. III/V on Si laser typically emit powers in the 10 mW range, while the pump power for OPO threshold is around 100 mW. The laser should be single-mode for stable OPO operation, which imposes a maximal ridge width and thus a minimum optical power density. Furthermore, high-power single-mode lasers are usually shallowly etched (for single-mode operation) and mounted epi-down (to limit thermal resistance) [172]. In our case, these two aspects cannot be implemented at the same time. See the discussion around [table 7-3](#): 1) if the laser is grown on top, the insulating section between laser and doped substrate makes it necessary to use lateral contacts, which requires deep lateral etching; 2) if the laser is grown under the NL waveguide, shallow etches are possible but epi-down mounting is impossible.

Fabrication tolerances should be examined carefully in the region of parametric conversion, since modal phase matching is very sensitive to variations in effective index.

Choice of geometry

To reduce fabrication complexity, we limit ourselves to a single level of etching. This implies that the bottom waveguide geometry is invariant in the direction of propagation, and that the top waveguide is narrowed. Keeping in mind the points presented in the previous section, we summarize the advantages of different geometries in [table 7-3](#). The waveguide where parametric light conversion takes places is called “NL waveguide” (for Non-Linear).

We choose the “laser on top” geometry, since it is more compatible with effective indices in our project. This geometry has two important drawbacks. To keep the underlying waveguide undoped, contact for the bottom part of the laser must be taken laterally instead of under the substrate. This implies that the gain region should be deeply etched to clear access to the contacts. This is obviously at odds with a single-mode laser operation, since the important index contrast between air and semiconductor (in the absence of an regrowth step) will cause the laser to oscillate on several transverse modes, unless it is extremely narrow, which is not desirable given the target optical power. As a solution, we propose to etch deeply only one side of the ridge. Single-mode operation can then be achieved with a contact on one side.

Proposed design

Given the design constraints presented earlier, we propose a general design. This work should be taken as a first exploration of principle and not as a fully detailed and completed design. We identified critical design aspects and estimated quality factors whenever possible. Several aspects of the device are still to be set.

	Laser on top	NL waveguide on top
Contacts	Lateral contacts are necessary to keep the NL guide undoped. This will hinder single-mode operation of the laser ☹️	Bottom contact can be taken under the substrate 😊
Thermal control	Epi-up ¹⁸ and epi-down are possible 😊	Epi-down is impossible ☹️
Laser multimodality	The laser must start in single-mode operation in a zone in shallow etching then it should taper down in the transfer zone. (Longer total length) ☹️	The laser is buried, single-mode emission is easily achieved 😊
Effective indices	Transition from a high index in the laser to a low index in the NL guide 😊	The laser index should be lower than indices in the NL waveguide, which are already low (~ 3.2) ☹️

Table 7-3. Advantages and drawbacks of different coupling geometries.

We show a general view of the structure in [figure 7-7](#). On the left, we choose a DFB cavity for the laser in order to provide longitudinal as well as transversal single-mode operation. The upper waveguide narrows in the transfer region, where the mode moves to the bottom waveguide. On the right, parametric conversion takes place in the bottom waveguide, where DBRs provide a high reflectivity at the signal and idler wavelengths. We will describe the device step by step, starting from the end because the zone of parametric conversion is the most sensitive to geometry variations.

¹⁸ See the definitions of epi-up and epi-down mounting in the footnote in page 87.

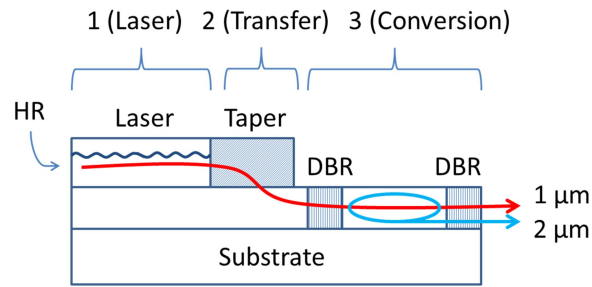


Figure 7-7. General view of the proposed coupled-cavity design.

Choice of material

To reach phase matching and a high conversion efficiency, we simulated various waveguide geometries before settling on high index contrasts and a pump of order 2 in the direction of growth. To maximize index contrast in the vertical direction, the waveguide is surrounded by $\text{Al}_{0.8}\text{Ga}_{0.2}\text{As}$ in the bottom cladding and by air above. However, in the region of transfer, the top cladding will be provided by whatever material separates laser and underlying waveguide core. We set this material to be $\text{Al}_{0.3}\text{Ga}_{0.7}\text{As}$, since it is already used as cladding in GaAs lasers (see [table 7-1](#)). This layer structure is summarized in [table 7-4](#). It is identical to the laser data sheet in [table 7-1](#), apart for the modified separation layer and added nonlinear waveguide and cladding. In the region of frequency conversion, all layers are etched, except for the last three: nonlinear waveguide, bottom cladding and substrate.

Layer type	Material
Top cladding	AlGaAs
Optical confinement (laser core)	InGaAsP
Quantum Well	InGaAs
Optical confinement (laser core)	InGaAsP
Separation layer	$\text{Al}_{0.3}\text{Ga}_{0.7}\text{As}$
Nonlinear waveguide	GaAs
Bottom cladding	$\text{Al}_{0.8}\text{Ga}_{0.2}\text{As}$
Substrate	GaAs

Table 7-4. Layer structure proposed for the coupled-cavity design, based on an Al-free active region structure. In the region of conversion, all layers are etched except the last three.

The waveguide core should hold as little aluminum as possible in order to increase its nonlinear susceptibility. We set the exact Al fraction by comparing the effective index of guided modes in the upper waveguide to the effective index of the lower waveguide as taper width is reduced ([figure 7-8](#)). For 10% Al composition, the laser

mode index crosses the index of TE_1 in the buried waveguide. We can thus expect the mode to couple to TE_1 . Using pure GaAs, the laser mode crosses only the TE_2 index, which is the desired configuration. Absorption in GaAs at $1\ \mu\text{m}$ is expected to be negligible [173]. Setting a pure GaAs waveguide has another advantage: it eliminates the uncertainty on the Al fraction.

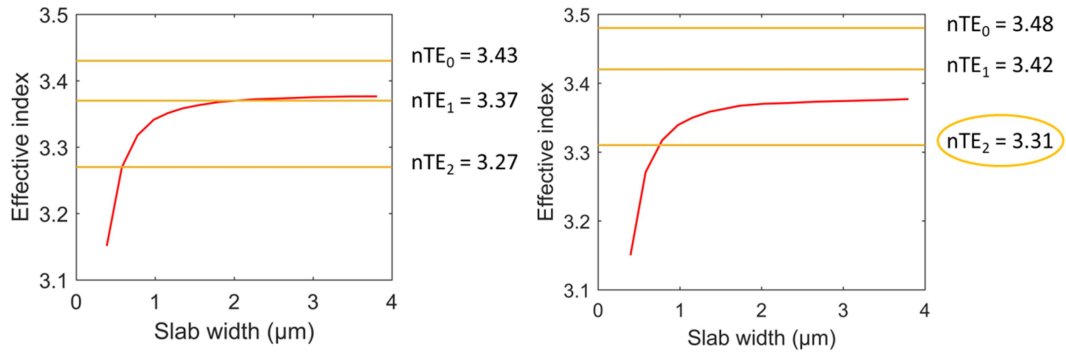


Figure 7-8. Effective indices of guided modes in the structure. Red: index of the laser mode as a function of guide width. Orange : indices of guided modes in the buried waveguide, assuming a planar waveguide of $\text{Al}_{0.1}\text{Ga}_{0.9}\text{As}$ (left) or GaAs (right) surrounded by $\text{Al}_{0.3}\text{Ga}_{0.7}\text{As}$ on one side and $\text{Al}_{0.8}\text{Ga}_{0.2}\text{As}$ on the other.

Conversion efficiency and OPO threshold

Figure 7-9 shows the nonlinear conversion efficiency as a function of ridge width for a waveguide of thickness $0.95\ \mu\text{m}$ surrounded by $\text{Al}_{0.8}\text{Ga}_{0.2}\text{As}$ and air. The corresponding pump powers necessary for an OPO threshold are presented in figure 7-10. Parasitic losses are assumed to be $0.1\ \text{cm}^{-1}$. As said earlier, the threshold pump power lies in the 10 to 100 mW range.

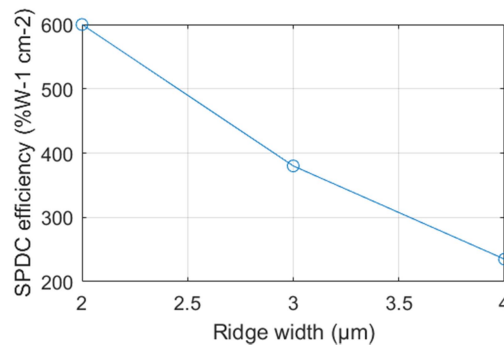


Figure 7-9. SPDC efficiency vs. ridge width in a $0.95\ \mu\text{m}$ thick waveguide surrounded by $\text{Al}_{0.8}\text{Ga}_{0.2}\text{As}$ and air.

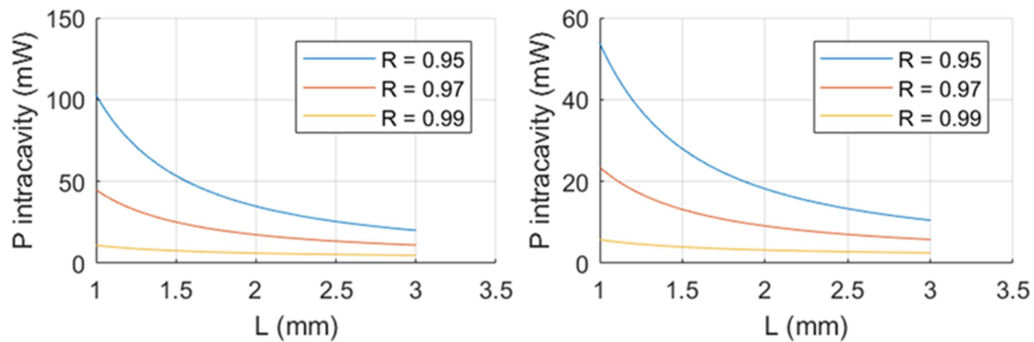


Figure 7-10. OPO pump power threshold for a ridge width of 4 μm (left) and 2 μm (right) as a function of length and signal/idler reflectivity. Guide thickness is 0.95 μm .

Tolerances

Figure 7-11 shows the SPDC normalized efficiency as a function of ridge width and thickness. The FWHM of efficiency is 200 nm for a variation in width, a value compatible with the current state of fabrication technology. The FWHM for a variation in thickness is much smaller, around 3 nm. The typical precision on thickness achieved by molecular beam epitaxy is approximately 2 %, corresponding to a variation of 2 nm in a 0.95 μm waveguide. Depending on growth systems, this value can be further increased by inhomogeneities along the wafer.

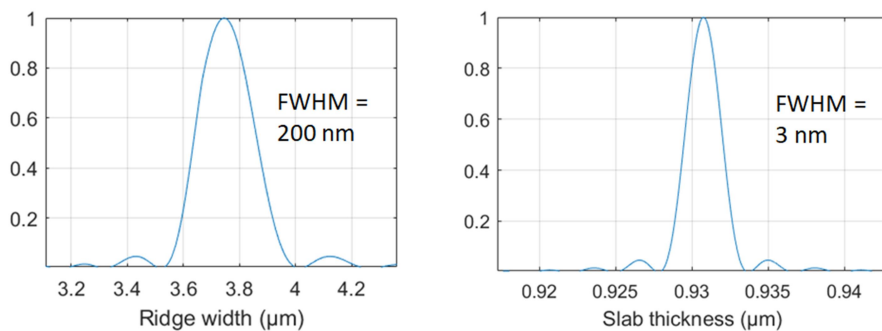


Figure 7-11. Normalized SPDC efficiency as a function of ridge width and thickness.

Fortunately, two tools allow us to shift the efficiency curve: temperature and pump wavelength. Figure 7-12 shows the normalized SPDC efficiency as a function of ridge width and thickness, for waveguide temperatures of 20°C and 50°C. A temperature shift of 30°C can compensate for a 10 nm variation of the waveguide core thickness. We stress here that the temperatures of laser and parametric conversion regions can be set separately, and that an increase of 30°C in the SPDC

area has a negligible impact on the laser temperature, assuming the two regions are separated by $300\ \mu\text{m}$ (a typical distance for adiabatic transfer).

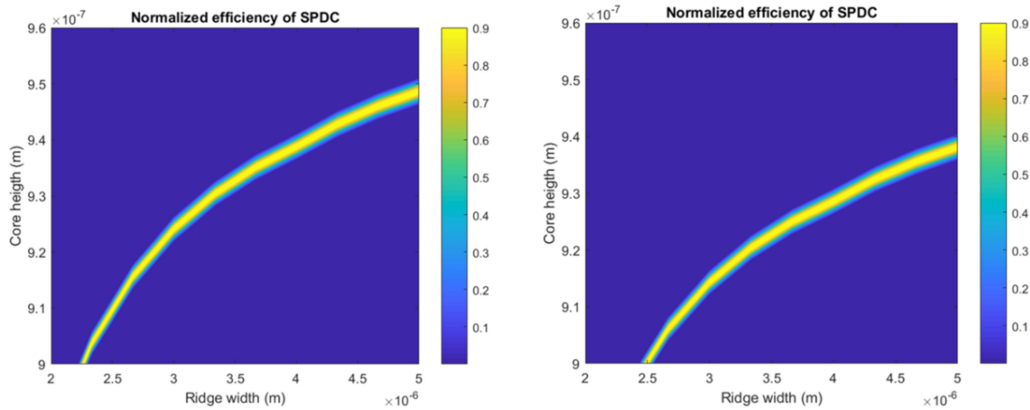


Figure 7-12. Normalized SPDC efficiency as a function of ridge width and thickness, for a waveguide temperature of 20°C (left) and 50°C (left). Pump wavelength is $1\ \mu\text{m}$ in both cases.

Figure 7-13 presents the normalized SPDC efficiency as a function of ridge width and thickness, at pump wavelengths of 990 and 1010 nm. A wavelength shift of $\pm 10\ \text{nm}$ can compensate for a variation of $40\ \text{nm}$ of the waveguide core thickness. This variation is typically accessible to a single-mode DFB laser.

As a conclusion, while efficient parametric down-conversion is only encountered in a narrow window of parameters, it can realistically be achieved by compensating variations in fabrication with a shift in temperature and pump wavelength.

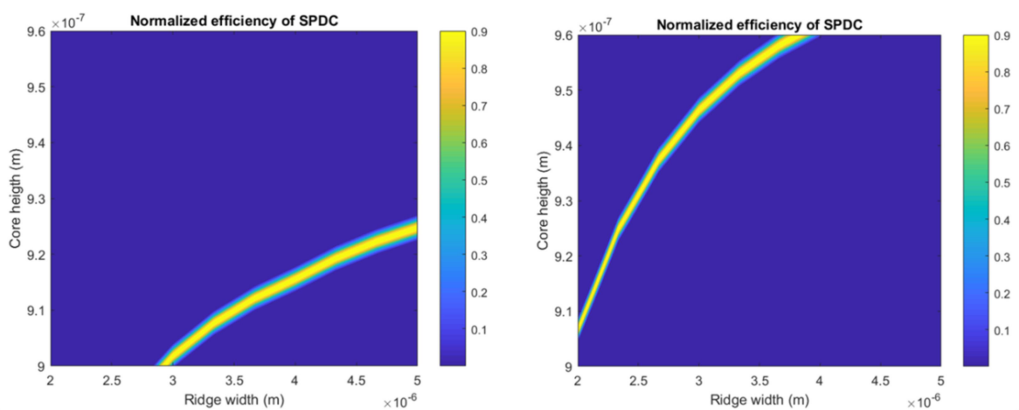


Figure 7-13. Normalized SPDC efficiency as a function of ridge width and thickness, for pump wavelengths of 990 nm (left) and 1010 nm (right). Temperature is 20°C in both cases.

DBR design

The DBRs should provide a reflectivity above 95% at both signal and idler wavelengths (see [figure 7-10](#)) and nearly null reflectivity at pump wavelength. This has already been demonstrated with dielectric stacks deposited on the waveguide facets [53]. While the outer mirror can be fabricated in this fashion, the inner one needs to be etched at an interface. Let us estimate now the DBR coupling constants in the approximation of weak perturbations. Given the important depths on which our calculations converge, a determination of the reflectivity by a FDTD simulation would likely be useful. For a DBR length of 100 μm , the coupling constant should be 220 cm^{-1} in order to achieve 95% reflectivity.

[Table 7-5](#) presents the coupling constants of the fundamental TE and TM modes at 2 μm for a grating depth of 200 nm. The grating is supposed perfectly rectangular, with a filling factor of one half. Whether the grating is formed by etching the top interface (air/GaAs) or by etching the underlying cladding and restarting epitaxy (GaAs/ $\text{Al}_{0.8}\text{Ga}_{0.2}\text{As}$ interface), an etch depth of at least 200 nm is necessary to achieve reflectivity over 95% with a DBR smaller than 100 μm .

Grating depth (nm)	Grating at the top interface (air/GaAs)		Grating at the lower interface (GaAs/ $\text{Al}_{0.8}\text{Ga}_{0.2}\text{As}$)	
	κ_{TE} (cm^{-1})	κ_{TM} (cm^{-1})	κ_{TE} (cm^{-1})	κ_{TM} (cm^{-1})
200	214.5	242.5	277	180.9

Table 7-5. Coupling constants for fundamental TE and TM modes at 2 μm , given a rectangular grating of depth 200 nm and duty cycle 50%.

Tunability

We show in [figure 7-14](#) the tunability curves of the waveguide at temperatures 20 and 40°C. Outside of degeneracy, a signal / idler wavelength range of 300 nm is accessible for a pump wavelength variation of a few nm.

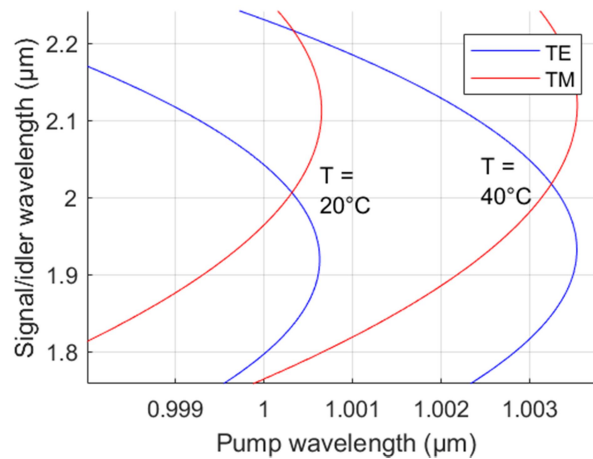


Figure 7-14. Tunability curves of the waveguide supporting frequency conversion.

Transfer

2-D approximation for the effective index

A transverse view of the structure is shown in [figure 7-15](#). The two waveguides are separated by 300 nm of $\text{Al}_{0.3}\text{Ga}_{0.7}\text{As}$. [Figure 7-16](#) presents a simulation of light propagation along the structure by a Beam Propagation Method (BPM), which I carried out with the commercial software RSoft. To reduce calculation time, we first make a 2D effective-index approximation, whose validity will be checked in the next section. The injected mode, visible on the right-end side of [figure 7-16a](#), is the eigenmode presenting the highest overlap with the active region. As is visible from [figure 7-16b](#), 90% of the guided power is contained in the laser core layer at $Z = 0$, i.e. before the taper. Thus modal gain is expected to not suffer from the presence of the underlying GaAs layer. From $Z = 0$ to $Z = 300 \mu\text{m}$, the two top layers widths are reduced from 4 μm to 0. From $Z = 300 \mu\text{m}$ to $Z = 500 \mu\text{m}$, the separation layer ($\text{Al}_{0.3}\text{Ga}_{0.7}\text{As}$) width is reduced in the same way. Over 95% of the power is transferred to the GaAs waveguide. To estimate the robustness of the design to a limited resolution in lithography, we simulate the same transfer with widths ending at 0.4 μm instead of 0: the transfer of power to the underlying waveguide is 85%. While a more detailed set of tests would be necessary to account for fabrication-induced deviations, these results are encouraging.

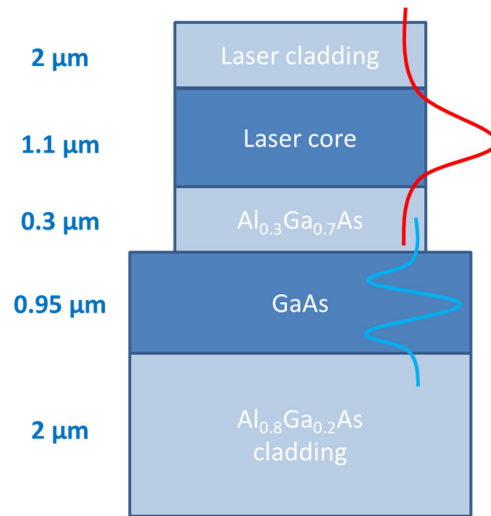


Figure 7-15. Transverse view of the structure. The fundamental mode of the top waveguide is shown in blue. Second-order mode of the lower waveguide is shown in red. The three top layers (laser cladding, laser core and Al_{0.3}Ga_{0.7}As separation) have widths varying from 4 μm to 0 μm. The GaAs waveguide and inferior cladding have infinite width.

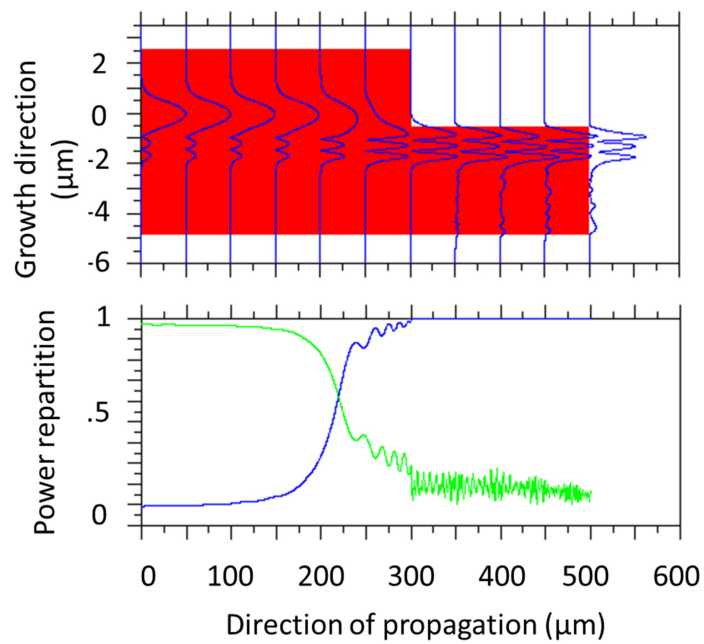


Figure 7-16. a) BPM simulation of light propagation in the structure. b) Normalized guided power along z , in the upper (laser, green) and the lower (OPO, blue) waveguide.

In order to find out if the power in the slab is in the desired TE₂ mode, we calculate the overlap of the BPM-simulated field with the GaAs waveguide eigenmodes. The result, reported in [figure 7-17](#), is that 97% of the power is in the TE₂ mode after one transfer length.

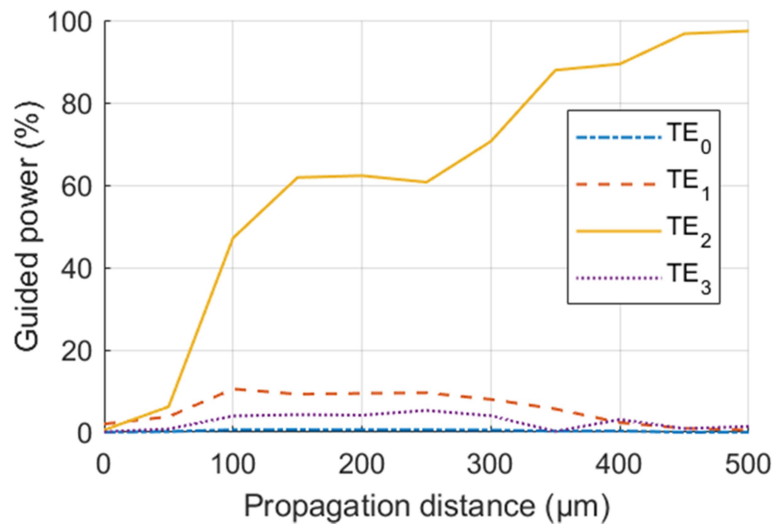


Figure 7-17. Modal decomposition of the BPM-simulated field in [figure 7-16](#) on the eigenmodes of the GaAs waveguide.

3D simulations

In the 2D-effective index approximation made in the previous section, we assumed single-mode behavior in the lateral direction. The geometry chosen in 3D must balance two conditions in order to give a high transfer to the TE₂₀ mode. On one hand, the lateral confinement of the buried waveguide should be minimal so that the single-mode approximation is satisfied, and coupling to higher-order modes in the lateral direction is minimized. On the other hand, the buried waveguide should be confined enough to prevent the field from escaping.

[Figure 7-18](#) shows the proposed taper design. From $Z = 0$ to $Z = 300 \mu\text{m}$, the width of laser cladding, top half of the laser core and QW is reduced from $4 \mu\text{m}$ to 0. From $Z = 300 \mu\text{m}$ to $Z = 600 \mu\text{m}$, the width of the bottom half of laser core and separation layer ($\text{Al}_{0.3}\text{Ga}_{0.7}\text{As}$) is reduced in the same way. The width of the final GaAs waveguide is $2 \mu\text{m}$. For this design, the calculated transfer efficiency into the TE₂₀ mode is as large as 80%.

[Figure 7-19](#) shows the power transmitted to the eigenmodes of the $2 \mu\text{m}$ wide and air clad GaAs ridge waveguide that are plotted in [figure 7-20](#). For sake of clarity,

among all the eigenmodes supported by the waveguide, we only show those that are the most likely to sustain a transfer (because they have a similar effective index, the same polarization and the same horizontal parity as the laser mode).

Modifying the taper shape affects the effective index and thus the position of transfer. A -0.02 shift in the laser core and cladding refractive indices accelerates the transfer without affecting the total transmission. An opposite shift (+0.02), which can be caused by a 30°C temperature increase, makes the transfer drop to 30-40% depending on the taper shape.

These values must be compared to the estimated OPO thresholds (figure 7-10): depending on the OPO cavity length and mirror reflectivity, its threshold can range from 20 to 100 mW. Transmission of 30 to 80% thus sets the target optical power at 25 to 300mW. Since AlGaAs laser diodes at 980 nm can emit powers in excess of 10W in broad-area configurations [174] and 700 to 1500 mW in narrow, laterally single-mode configurations [172], our target power seems within reach.

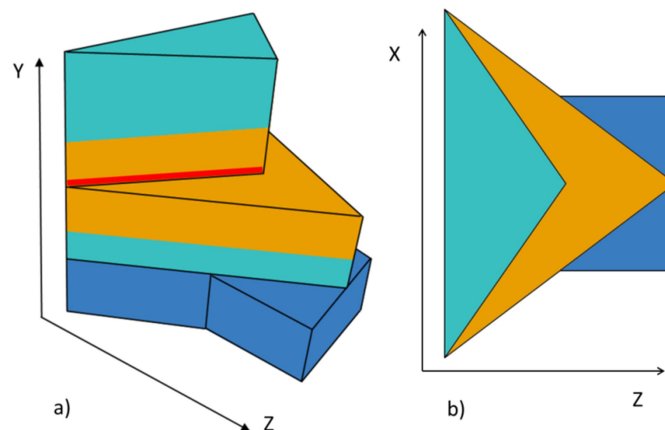


Figure 7-18. Side (a) and top (b) view of the proposed taper geometry. Green: $\text{Al}_{0.3}\text{Ga}_{0.7}\text{As}$, orange: laser core layer, dark blue: GaAs, red: quantum well. Dimensions are not to scale.

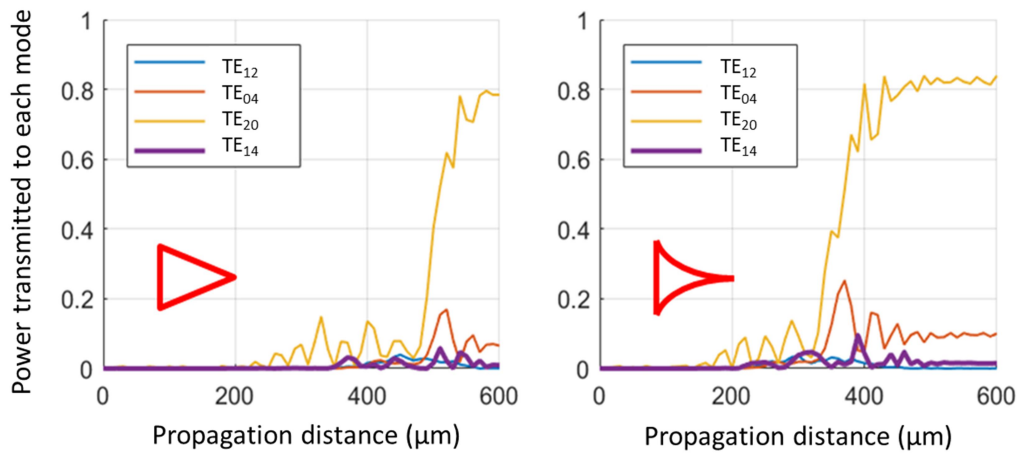


Figure 7-19. Power transmitted to the eigenmodes in figure 7-20. Left: triangular tapers, right: quadratic tapers

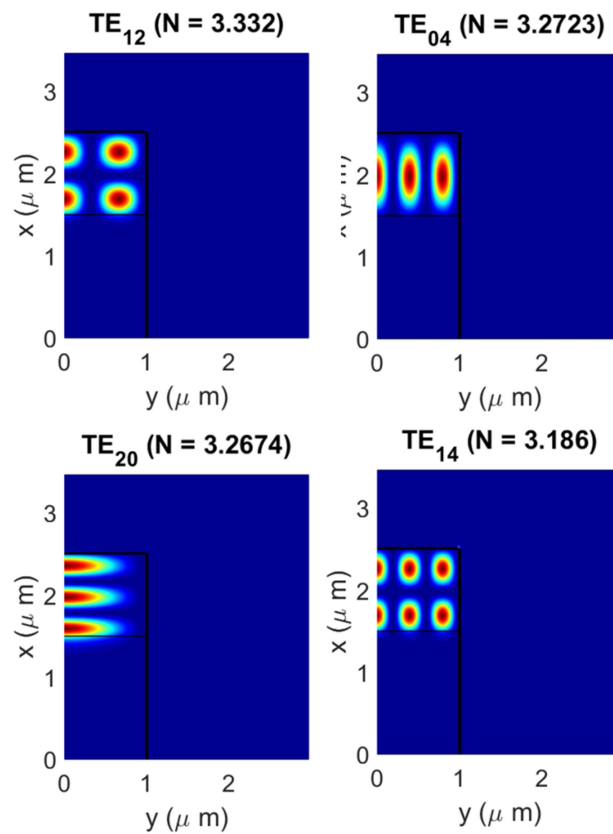


Figure 7-20. Four eigenmodes of the ridge GaAs waveguide of width 2 μm. The pump mode for SPDC is TE₂₀ (bottom left). Only half of the waveguide is represented in the lateral direction for symmetry reasons.

Laser

We propose here a preliminary description of the laser cavity. While the laser design is unconventional, we show that its key parameters (confinement in the QW, reflectivity, estimated differential efficiency) fall in a typical range of values for AlGaAs lasers. Active properties are not investigated, although they could be undertaken in the future on the basis of this work.

Thermal behavior

As mentioned earlier, thermal behavior is a critical point for the operation of the DOPO source. Given a maximal ridge width for single-mode operation, an epi-up geometry and a target optical power, we can estimate the temperature rise in the laser.

The laser ridge width is taken to be $5\ \mu\text{m}$, as this size provides single-mode operation for an index contrast of 0.005 [172]. Assuming a target optical power of 100 mW and a wall-plug efficiency of 16%, the emitted power in the form of heat is 500 mW. We simulate a crude model of the temperature rise with the software COMSOL. The heat is assumed to escape fully from the junction, of size $5\ \mu\text{m} \times 0.1\ \mu\text{m} \times L$ (1, 2 or 3 mm) (figure 7-21). The latter is set inside $10\ \mu\text{m}$ of $\text{Al}_{0.3}\text{Ga}_{0.7}\text{As}$, and the underlying material is GaAs. Figure 7-22 shows the junction temperature calculated as a function of the substrate thickness for three different lengths ($L = 1, 2$ or 3 mm).

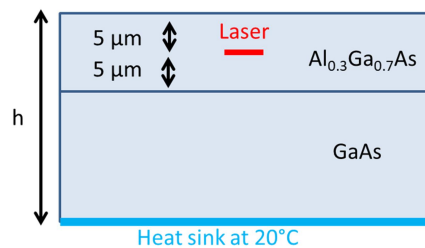


Figure 7-21. Model used to estimate the laser temperature rise

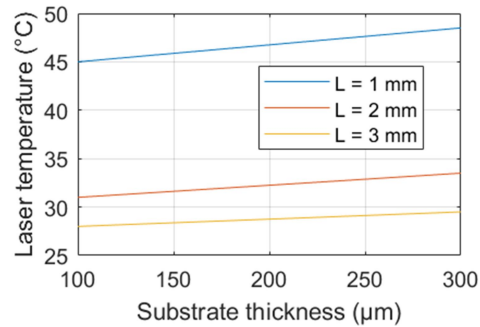


Figure 7-22. Junction temperature as a function substrate thickness, for three laser lengths.

To stay under 40°C, we find that the laser should be at least 2 mm long and the wall-plug efficiency should be over 16% at the target power.

Key parameters

To limit its temperature rise, the laser should be at the least 2 mm long. This size is above the average for common sources in integrated optics, which often favor compactness. Large DFB grating lengths increase modal reflectivity, lowering threshold but also degrading differential efficiency. Furthermore, the laser mode is only partially confined before the taper, so we estimate the impact of confinement on the modal gain.

In order to achieve high optical powers and single-mode operation, we propose a DFB laser with low grating reflectivity and HR coating on the external facet. We assume that the DFB grating is etched at the interface between laser core and top cladding. To avoid regrowth, gratings can also be etched on the surface [175]. However, optimization of surface gratings depends on the top contact geometry, which has not been defined yet. Therefore we present only the buried grating case.

If the laser is 1 to 2 mm long to limit temperature rise, an etch depth of 10 to 20 nm is necessary to provide a κL product of ~ 0.5 (where κ is the coupling constant of the fundamental mode). This value is realistically achievable with a shallow etch and epitaxy regrowth.

For a laser of length 2 mm with a coating of reflectivity 90% on the external facet, assuming a κL product of 0.5, total output coupling losses are 9 cm^{-1} [86]. If parasitic losses are 10 cm^{-1} and internal efficiency is 80%, external differential efficiency is 0.38. The modal gain needed to reach laser oscillation is 19 cm^{-1} [86]. QW lasers at 980 nm commonly achieve modal gains in excess of this value [125], however the threshold is also affected by the confinement factor. For a single QW of thickness 10

nm, we find that the confinement of lasing mode in the well is 1.2%, which corresponds to a material gain of 1600 cm^{-1} at threshold. This is achieved under a carrier density of $2.5 \times 10^{18} \text{ cm}^{-3}$ in the well [123]. Assuming a recombination time of 3 ns, the threshold current density is then expected to be 130 A/cm^2 , comparable to the range of 120 to 150 A/cm^2 measured in similar lasers [122,170].

In conclusion, we have shown that the key parameters (threshold and efficiency) of this laser are not affected by its unusual design, and that they are compatible with operation in excess of 100 mW.

Conclusion

In this chapter we have defined the main conditions that a DOPO structure based on a vertical coupler should satisfy, and we have described the passive properties of this source. Phase-matching is realistically achievable in situ, through wavelength and temperature tuning. We achieve transfer to a higher-order mode of the structure, with sufficient efficiency given the optical power likely deliverable. The taper layout can presumably be improved in further work.

Overall, this design predicts promising results for the fabrication of an integrated diode-OPO. Unlike the original all-in-one DOPO proposal, the latter does not require record-low propagation losses in the laser diode. The constraints on parasitic losses and doping profile are reported to constraints on the operation of a laser at once single-mode, high-power and contacted by the surface. Future work will likely be inspired by the sources developed in III/V on Si integration.

Fabrication is more complex than in the original setup. If the laser DFB grating can be defined at the surface, epitaxy regrowth can be avoided completely. Most of the technological complexity occurs in the various etching levels necessary to define the whole structure, from tapers to DFB grating to DBRs.

To ensure feasibility of this project, future work should focus on laser design, particularly on expected optical power and impact of doping on the transfer.

General conclusion

We have presented the work done towards the demonstration of an electrically injected optical parametric oscillator. The main part of this project relies on the use of narrow, deeply-etched laser diodes in order to control phase mismatch through the ridge width. Quantum dots and dashes are therefore proposed as an active medium in order to limit nonradiative recombinations on the sidewalls. Waveguides are designed to lase on a higher-order mode in the growth direction and enable down-conversion to fundamental modes.

Complementary designs were developed in the GaAs and InP platforms, with laser emission respectively at 0.98 and 1.55 μm . In order to establish a design in InP, I built an m-lines setup to measure the refractive index of InGaAsP outside of the wavelength range covered in literature. Index was determined with a precision of 10^{-3} , at wavelengths 1.55, 2.1 and 3.1 μm , in a range of composition of the quaternary lattice-matched to InP. Accuracy on our interpolation of index is limited to 10^{-2} to 2×10^{-2} because of composition variations in the tested samples, although it could be increased if measurements are repeated on a larger sample collection. Agreement with previously published data is good in the wavelengths range where comparison is possible. On the base of these measurements, I designed a laser diode in the InGaAsP/ InP platform.

Because of a major failure of the epitaxy system in INAC, epitaxy of quantum dot laser structures was not possible during the course of this PhD. However, wide (100 μm) quantum well lasers were fabricated in the III-V Lab. Their characterization allowed us to confirm emission on a higher order mode and to assess basic electrical characteristics. Threshold currents are low for this type of laser (in the range of 100 A/cm²). Series resistance, 0.5 Ω for 1x0.1 mm lasers, is higher than in state of the art laser diodes of the same type. This is likely due to the atypical band and doping profiles. Emission on a higher-order mode is verified, however a shift towards the fundamental mode emission occurs for cavities longer than 2 mm. This is an inconvenient since OPO threshold is lower in long cavities. The phenomena of modal competition are not well understood and will hopefully be clarified in narrow ridge lasers. Furthermore, as mentioned in chapter 3, modal selectivity will likely be higher in QD lasers, as threshold gains for both modes lie closer to gain at saturation. Propagation losses are in the range of calculated values and relatively low for this type of laser, under 3 cm⁻¹. We estimate that they mainly arise from FCA from the introduced doping profile. Doping should be lowered in the future to keep

losses at the signal / idler frequency under nonlinear gain. It is unclear whether FCA in dots and dashes will have a significant impact on absorption: we are lacking data from the literature on the absorption in confined heterostructures. Thus it would be interesting to measure absorption losses in contacted ridge lasers at the signal / idler frequency.

In future developments of this design, the doping profile should be modified in the future to lower propagation losses from a current value of 3 cm^{-1} to less than 0.8 cm^{-1} . This value corresponds to the OPO threshold in the case of high reflectivity ($R > 0.99$) mirrors with a pump intracavity power of 100 mW. Series resistance is expected to increase in future devices with lower doping. Thermal resistance can be expected to increase in narrow lasers, so measuring it in the current broad area devices would be of interest.

Maximal power density in short (1 mm) cavities at the moment permits OPO threshold if propagation losses are under 0.2 cm^{-1} , under the value of record propagation losses to this day [127]. Nonlinear gain could instead be increased. This can be done either by raising the pump power density or by using longer cavities. Exploring a larger range of current to increase optical power seems difficult since thermal and series resistance will likely increase in narrow geometries. In contrast, pump power density can be raised by depositing high-reflectivity mirrors on the facets. Furthermore, nonlinear gain can be improved by using narrower geometries, at the cost of increased fabrication complexity and lower tolerances on ridge width.

Thus, the perspectives for this laser – OPO design are the fabrication of narrow ridge waveguides with lower doping levels and high reflectivities at the laser wavelength. Epitaxy of quantum dots on GaAs should be possible in the next months in the MBE of INAC. For the fabrication of narrow deeply-etched geometries, I have developed a dry etch procedure yielding deep ($10 \text{ }\mu\text{m}$) etches with a control of angle to the degree. Reaching OPO threshold in these structures seems like an achievable goal, albeit ambitious. Propagation losses must be brought to levels close to state of the art. Furthermore, fabrication process must be mastered in order to provide high reflectivities at all wavelengths, ideally with an independent control of phase mismatch at separate wavelengths in the future, while keeping threshold, series and thermal resistance low in narrow structures with a precise control of ridge width.

The main constraints of this system are doping-induced propagation losses and the condition of triple resonance on pump, signal and idler. To alleviate these two

points I have described a source based on an alternative design, in which a laser cavity is vertically coupled by a taper to an underlying waveguide where nonlinear conversion frequency can take place. While fabrication is more complex than in the original diode-OPO design, spectral stability is improved and the constraint on low intracavity losses in the laser cavity disappears. Transfer is achieved to a higher-order mode of the underlying waveguide and threshold lies in the 20 to 100 mW range. Tolerances are estimated and it is found that variations in fabrication can be compensated by a shift of laser emission wavelength. The most important change of this design with respect to existing vertically coupled lasers is the requirement of relatively high (over 20 mW) laser emission with simultaneous monomode emission. Furthermore, the laser should be contacted by the surface. So far, all work done is in a passive design. Future work should concentrate on the detailed description of laser characteristics, in particular maximal available power and impact of doping on the transfer.

List of publications and conferences

Publications

A. Bernard, J.M. Gérard, M. Krakowski, O. Parillaud, B. Gérard, I. Favero, G. Leo. "Design of a widely tunable source in the 2 μm range based on a vertical coupler". In preparation.

A. Bernard, M. Ravaro, I. Roland, J.M. Gérard, M. Krakowski, O. Parillaud, B. Gérard, I. Favero, G. Leo. "Mid-infrared optical characterization of InGaAsP". In preparation.

A. Bernard, M. Ravaro, I. Roland, J.M. Gérard, M. Krakowski, O. Parillaud, B. Gérard, I. Favero, G. Leo. "Widely tunable quantum dot source around 3 μm ". "Quantum-dot based light-emitting diodes", *InTech*, Oct. 2017.

A. Bernard, S. Mariani, A. Andronico, J.M. Gerard, M. Kamp, P.U. Jepsen, G. Leo. "Quantum-dot-based integrated non-linear sources". *IET Optoelectronics*. vol. 2, no. 2, pp. 82-87, Feb. 2015.

Conferences

A. Bernard, M. Ravaro, I. Roland, J.M. Gérard, M. Krakowski, O. Parillaud, B. Gérard, I. Favero, G. Leo. "Parametric quantum-dash source around 3 μm ". In Mid-Infrared Coherent Sources and Applications. Oral presentation. Mar. 2018.

A. Bernard, J.M. Gérard, M. Kamp, I. Favero, S. Ducci, G. Leo. Journées Boîtes Quantiques, Grenoble. "Diode OPO à boîtes quantiques". Poster. Jun. 2015.

A. Bernard, J.M. Gérard, M. Kamp, I. Favero, S. Ducci, G. Leo. Ecole d'été sur l'Optique non linéaire, Les Houches. "Diode OPO à boîtes quantiques". Poster. Apr. 2015

A. Bernard, J.M. Gérard, M. Kamp, I. Favero, S. Ducci, G. Leo. Journée Ruptures Technologiques en Optoélectronique. "Diode OPO à boîtes quantiques". Poster. Jun. 2014.

Bibliography

- [1] T. H. Maiman, "Stimulated Optical Radiation in Ruby," *Nature*, vol. 187, no. 4736, pp. 493–494, Aug. 1960.
- [2] M. I. Nathan, W. P. Dumke, G. Burns, F. H. Dill, and G. Lasher, "STIMULATED EMISSION OF RADIATION FROM GaAs *p-n* JUNCTIONS," *Appl. Phys. Lett.*, vol. 1, no. 3, pp. 62–64, Nov. 1962.
- [3] R. N. Hall, G. E. Fenner, J. D. Kingsley, T. J. Soltys, and R. O. Carlson, "Coherent Light Emission From GaAs Junctions," *Phys. Rev. Lett.*, vol. 9, no. 9, pp. 366–368, Nov. 1962.
- [4] H. Rong *et al.*, "An all-silicon Raman laser," *Nature*, vol. 433, no. 7023, p. 292, Jan. 2005.
- [5] Z. Zhou, B. Yin, and J. Michel, "On-chip light sources for silicon photonics," *Light Sci. Appl.*, vol. 4, no. 11, pp. e358–e358, Nov. 2015.
- [6] Y. B. Bolkhovityanov and O. P. Pchelyakov, "GaAs epitaxy on Si substrates: modern status of research and engineering," *Phys.-Uspekhi*, vol. 51, no. 5, pp. 437–456, May 2008.
- [7] S. Nakamura, M. Senoh, and T. Mukai, "High-power InGaN/GaN double-heterostructure violet light emitting diodes," *Appl. Phys. Lett.*, vol. 62, no. 19, pp. 2390–2392, May 1993.
- [8] R. Kazarinov, "Possibility of amplification of electromagnetic waves in a semiconductor with superlattice," *Sov Phys-Semicond*, vol. 5, no. 4, pp. 707–709, Oct. 1971.
- [9] J. Faist, F. Capasso, D. L. Sivco, C. Sirtori, A. L. Hutchinson, and A. Y. Cho, "Quantum Cascade Laser," *Science*, vol. 264, no. 5158, pp. 553–556, Apr. 1994.
- [10] M. S. Vitiello, G. Scalari, B. Williams, and P. De Natale, "Quantum cascade lasers: 20 years of challenges," *Opt. Express*, vol. 23, no. 4, p. 5167, Feb. 2015.
- [11] R. Q. Yang, "Infrared laser based on intersubband transitions in quantum wells," *Superlattices Microstruct.*, vol. 17, no. 1, pp. 77–83, Jan. 1995.

- [12] C.-H. Lin *et al.*, "Type-II interband quantum cascade laser at 3.8 μm ," *Electron. Lett.*, vol. 33, no. 7, pp. 598–599, Mar. 1997.
- [13] M. Kim *et al.*, "Interband cascade laser emitting at $\lambda=3.75\ \mu\text{m}$ in continuous wave above room temperature," *Appl. Phys. Lett.*, vol. 92, no. 19, p. 191110, May 2008.
- [14] "Quantum cascade laser (Wikipedia)," *Wikipedia*. [Online]. Available: en.wikipedia.org/wiki/Quantum_cascade_laser. [Accessed: 12-Apr-2018].
- [15] "Next generation mid-infrared Chemical and Biological Sensors," *ICL*. [Online]. Available: <http://www.spectroscopyonline.com/next-generation-mid-infrared-chemical-and-biological-sensors-combining-quantum-cascade-lasers-thin-f>. [Accessed: 12-Apr-2018].
- [16] Scholle, "2 μm Laser Sources and Their Possible Applications | InTechOpen," in *Frontiers in Guided Wave Optics and Optoelectronics*, InTech, 2010.
- [17] S. P. Siebenaler, A. M. Janka, D. Lyon, J. P. Edlebeck, and A. E. Nowlan, "Methane Detectors Challenge: Low-Cost Continuous Emissions Monitoring," p. V003T04A013, Sep. 2016.
- [18] C. Wang and P. Sahay, "Breath Analysis Using Laser Spectroscopic Techniques: Breath Biomarkers, Spectral Fingerprints, and Detection Limits," *Sensors*, vol. 9, no. 10, pp. 8230–8262, Oct. 2009.
- [19] J. Faist, F. Capasso, D. L. Sivco, A. L. Hutchinson, S.-N. G. Chu, and A. Y. Cho, "Short wavelength ($\lambda\sim 3.4\ \mu\text{m}$) quantum cascade laser based on strained compensated InGaAs/AlInAs," *Appl. Phys. Lett.*, vol. 72, no. 6, pp. 680–682, Feb. 1998.
- [20] J. Devenson, D. Barate, O. Cathabard, R. Teissier, and A. N. Baranov, "Very short wavelength ($\lambda=3.1\text{--}3.3\ \mu\text{m}$) quantum cascade lasers," *Appl. Phys. Lett.*, vol. 89, no. 19, p. 191115, Nov. 2006.
- [21] J. Devenson, O. Cathabard, R. Teissier, and A. N. Baranov, "InAs/AlSb quantum cascade lasers emitting at 2.75–2.97 μm ," *Appl. Phys. Lett.*, vol. 91, no. 25, p. 251102, Dec. 2007.
- [22] O. Cathabard, R. Teissier, J. Devenson, J. C. Moreno, and A. N. Baranov, "Quantum cascade lasers emitting near 2.6 μm ," *Appl. Phys. Lett.*, vol. 96, no. 14, p. 141110, Apr. 2010.

- [23] N. Bandyopadhyay, Y. Bai, S. Tsao, S. Nida, S. Slivken, and M. Razeghi, "Room temperature continuous wave operation of $\lambda \sim 3\text{--}3.2\ \mu\text{m}$ quantum cascade lasers," *Appl. Phys. Lett.*, vol. 101, no. 24, p. 241110, Dec. 2012.
- [24] Q. Gaimard, L. Cerutti, R. Teissier, and A. Vicet, "Distributed feedback GaSb based laser diodes with buried grating," *Appl. Phys. Lett.*, vol. 104, no. 16, p. 161111, Apr. 2014.
- [25] T. Milde et al., "New GasB-based single-mode diode lasers in the NIR and MIR spectral regime for sensor applications," in *Novel In-Plane Semiconductor Lasers XVII*, 2018, vol. 10553, p. 105530C.
- [26] K. M. Manfred, G. a. D. Ritchie, N. Lang, J. Röpcke, and J. H. van Helden, "Optical feedback cavity-enhanced absorption spectroscopy with a $3.24\ \mu\text{m}$ interband cascade laser," *Appl. Phys. Lett.*, vol. 106, no. 22, p. 221106, Jun. 2015.
- [27] L. Dong, C. Li, N. P. Sanchez, A. K. Gluszek, R. J. Griffin, and F. K. Tittel, "Compact CH_4 sensor system based on a continuous-wave, low power consumption, room temperature interband cascade laser," *Appl. Phys. Lett.*, vol. 108, no. 1, p. 011106, Jan. 2016.
- [28] P. Rauter and F. Capasso, "Multi-wavelength quantum cascade laser arrays: Multi-wavelength quantum cascade laser arrays," *Laser Photonics Rev.*, vol. 9, no. 5, pp. 452–477, Sep. 2015.
- [29] B. G. Lee et al., "Widely tunable single-mode quantum cascade laser source for mid-infrared spectroscopy," *Appl. Phys. Lett.*, vol. 91, no. 23, p. 231101, Dec. 2007.
- [30] N. Bandyopadhyay, M. Chen, S. Sengupta, S. Slivken, and M. Razeghi, "Ultra-broadband quantum cascade laser, tunable over $760\ \text{cm}^{-1}$ with balanced gain," *Opt. Express*, vol. 23, no. 16, p. 21159, Aug. 2015.
- [31] G. N. Rao and A. Karpf, "External cavity tunable quantum cascade lasers and their applications to trace gas monitoring," *Appl. Opt.*, vol. 50, no. 4, pp. A100–A115, Jan. 2011.
- [32] R. Ostendorf et al., "Real-time spectroscopic sensing using a widely tunable external cavity-QCL with MOEMS diffraction grating," in *Quantum Sensing and Nano Electronics and Photonics XIII*, 2016, vol. 9755, p. 975507.

- [33] D. Caffey *et al.*, "Performance characteristics of a continuous-wave compact widely tunable external cavity interband cascade lasers," *Opt. Express*, vol. 18, no. 15, pp. 15691–15696, Jul. 2010.
- [34] N. Owschimikow *et al.*, "Resonant Second-Order Nonlinear Optical Processes in Quantum Cascade Lasers," *Phys. Rev. Lett.*, vol. 90, no. 4, p. 043902, Jan. 2003.
- [35] C. Gmachl *et al.*, "Optimized second-harmonic generation in quantum cascade lasers," *IEEE J. Quantum Electron.*, vol. 39, no. 11, pp. 1345–1355, Nov. 2003.
- [36] J. Peng, "Developments of mid-infrared optical parametric oscillators for spectroscopic sensing: a review," *Opt. Eng.*, vol. 53, no. 6, pp. 061613–061613, Feb. 2014.
- [37] D. D. Arslanov, M. Spunei, J. Mandon, S. M. Cristescu, S. T. Persijn, and F. J. M. Harren, "Continuous-wave optical parametric oscillator based infrared spectroscopy for sensitive molecular gas sensing," *Laser Photonics Rev.*, vol. 7, no. 2, pp. 188–206, Mar. 2013.
- [38] J. A. Giordmaine and R. C. Miller, "Tunable Coherent Parametric Oscillation in LiNbO₃ at Optical Frequencies," *Phys. Rev. Lett.*, vol. 14, no. 24, pp. 973–976, Jun. 1965.
- [39] M. Yamada, N. Nada, M. Saitoh, and K. Watanabe, "First-order quasi-phase matched LiNbO₃ waveguide periodically poled by applying an external field for efficient blue second-harmonic generation," *Appl. Phys. Lett.*, vol. 62, no. 5, pp. 435–436, Feb. 1993.
- [40] J. A. Armstrong, N. Bloembergen, J. Ducuing, and P. S. Pershan, "Interactions between Light Waves in a Nonlinear Dielectric," *Phys. Rev.*, vol. 127, no. 6, pp. 1918–1939, Sep. 1962.
- [41] W. Sohler *et al.*, "Integrated Optical Devices in Lithium Niobate," *Opt. Photonics News*, vol. 19, no. 1, pp. 24–31, Jan. 2008.
- [42] C. C. Lee and H. Y. Fan, "Second-harmonic generation in InSb, InP, and AlSb," *Phys. Rev. B*, vol. 10, no. 2, pp. 703–709, Jul. 1974.
- [43] L. A. Eyres *et al.*, "All-epitaxial fabrication of thick, orientation-patterned GaAs films for nonlinear optical frequency conversion," *Appl. Phys. Lett.*, vol. 79, no. 7, pp. 904–906, Aug. 2001.

- [44] K. L. Vodopyanov, "Optical generation of narrow-band terahertz packets in periodically-inverted electro-optic crystals: conversion efficiency and optimal laser pulse format," *Opt. Express*, vol. 14, no. 6, pp. 2263–2276, Mar. 2006.
- [45] A. Grisard, F. Gutty, E. Lallier, and B. Gérard, "Compact fiber laser-pumped mid-infrared source based on orientation-patterned Gallium Arsenide," in *Technologies for Optical Countermeasures VII*, 2010, vol. 7836, p. 783606.
- [46] C. Kieleck, M. Eichhorn, A. Hirth, D. Faye, and E. Lallier, "High-efficiency 20–50 kHz mid-infrared orientation-patterned GaAs optical parametric oscillator pumped by a 2 μm holmium laser," *Opt. Lett.*, vol. 34, no. 3, pp. 262–264, Feb. 2009.
- [47] M. B. Oron, P. Blau, S. Pearl, and M. Katz, "Optical parametric oscillation in orientation patterned GaAs waveguides," in *Nonlinear Frequency Generation and Conversion: Materials, Devices, and Applications XI*, 2012, vol. 8240, p. 82400C.
- [48] S. Roux *et al.*, "Low-loss orientation-patterned GaSb waveguides for mid-infrared parametric conversion," *Opt. Mater. Express*, vol. 7, no. 8, p. 3011, Aug. 2017.
- [49] S. Guha, J. O. Barnes, and P. G. Schunemann, "Mid-wave infrared generation by difference frequency mixing of continuous wave lasers in orientation-patterned Gallium Phosphide," *Opt. Mater. Express*, vol. 5, no. 12, p. 2911, Dec. 2015.
- [50] J. Hite *et al.*, "Development of periodically oriented gallium nitride for non-linear optics," *Opt. Mater. Express*, vol. 2, no. 9, pp. 1203–1208, Sep. 2012.
- [51] J. P. van der Ziel and A. C. Gossard, "Optical birefringence of ultrathin $\text{Al}_x\text{Ga}_{1-x}\text{As}/\text{GaAs}$ multilayer heterostructures," *J. Appl. Phys.*, vol. 49, no. 5, pp. 2919–2921, May 1978.
- [52] A. Fiore *et al.*, "Second-harmonic generation at $\lambda=1.6 \mu\text{m}$ in $\text{AlGaAs}/\text{Al}_2\text{O}_3$ waveguides using birefringence phase matching," *Appl. Phys. Lett.*, vol. 72, no. 23, pp. 2942–2944, Jun. 1998.
- [53] M. Savanier *et al.*, "Near-infrared optical parametric oscillator in a III-V semiconductor waveguide," *Appl. Phys. Lett.*, vol. 103, no. 26, p. 261105, Dec. 2013.
- [54] J. B. Khurgin, M. W. Pruessner, T. H. Stievater, and W. S. Rabinovich, "Suspended AlGaAs waveguides for tunable difference frequency generation in mid-infrared," *Opt. Lett.*, vol. 33, no. 24, pp. 2904–2906, Dec. 2008.

- [55] A. S. Helmy, "Phase matching using Bragg reflection waveguides for monolithic nonlinear optics applications," *Opt. Express*, vol. 14, no. 3, pp. 1243–1252, Feb. 2006.
- [56] R. Horn, P. Abolghasem, B. J. Bijlani, D. Kang, A. S. Helmy, and G. Weihs, "Monolithic Source of Photon Pairs," *Phys. Rev. Lett.*, vol. 108, no. 15, p. 153605, Apr. 2012.
- [57] F. Boitier *et al.*, "Electrically Injected Photon-Pair Source at Room Temperature," *Phys. Rev. Lett.*, vol. 112, no. 18, May 2014.
- [58] M. L. Iu *et al.*, "Efficient frequency conversion over S-C-L-U bands within an electrically pumped chip using χ^2 ," in *Photonics Conference (IPC) Part II, 2017 IEEE*, 2017, pp. 1–2.
- [59] P. Abolghasem, D. Kang, D. F. Logan, M. Lungwitz, and A. S. Helmy, "Widely tunable frequency conversion in monolithic semiconductor waveguides at 2.4 μm ," *Opt. Lett.*, vol. 39, no. 12, pp. 3591–3594, Jun. 2014.
- [60] N. Zareian and A. S. Helmy, "Static and dynamic characteristics of integrated semiconductor optical parametric oscillators," *J. Opt. Soc. Am. B*, vol. 30, no. 8, p. 2306, Aug. 2013.
- [61] A. Andronico, J. M. Gérard, I. Favero, S. Ducci, and G. Leo, "Quantum Dot parametric source," *Opt. Commun.*, vol. 327, pp. 27–30, Sep. 2014.
- [62] J. M. Gérard, O. Cabrol, and B. Sermage, "InAs quantum boxes: Highly efficient radiative traps for light emitting devices on Si," *Appl. Phys. Lett.*, vol. 68, no. 22, pp. 3123–3125, May 1996.
- [63] P. A. Franken, A. E. Hill, C. W. Peters, and G. Weinreich, "Generation of Optical Harmonics," *Phys. Rev. Lett.*, vol. 7, no. 4, pp. 118–119, Aug. 1961.
- [64] R. W. Boyd, *Nonlinear Optics*. Academic Press, 2003.
- [65] Suhura, *Waveguide Nonlinear-Optic Devices*. Springer, 2003.
- [66] R. L. Sutherland, *Handbook of Nonlinear Optics*. CRC Press, 2003.
- [67] G. Bava, I. Montrosset, W. Sohler, and H. Suche, "Numerical modeling of Ti:LiNbO₃ integrated optical parametric oscillators," *IEEE J. Quantum Electron.*, vol. 23, no. 1, pp. 42–51, Jan. 1987.

- [68] C. Ozanam, "Oscillateur paramétrique optique en guides d'ondes AlGaAs/AlO_x," PhD Thesis, Université Sorbonne Paris Cité - Université Paris Diderot (Paris 7), 2015.
- [69] A. Yariv, *Quantum electronics*. Wiley, 1989.
- [70] J. Bjorkholm, A. Ashkin, and R. Smith, "Improvement of optical parametric oscillators by nonresonant pump reflection," *IEEE J. Quantum Electron.*, vol. 6, no. 12, pp. 797–799, Dec. 1970.
- [71] T. Debuisschert, A. Sizmann, E. Giacobino, and C. Fabre, "Type-II continuous-wave optical parametric oscillators: oscillation and frequency-tuning characteristics," *JOSA B*, vol. 10, no. 9, pp. 1668–1680, Sep. 1993.
- [72] M. Oshman and S. Harris, "Theory of optical parametric oscillation internal to the laser cavity," *IEEE J. Quantum Electron.*, vol. 4, no. 8, pp. 491–502, Aug. 1968.
- [73] M. Martinelli, K. S. Zhang, T. Coudreau, A. Maître, and C. Fabre, "Ultra-low threshold CW triply resonant OPO in the near infrared using periodically poled lithium niobate," *J. Opt. Pure Appl. Opt.*, vol. 3, no. 4, p. 300, Jul. 2001.
- [74] L. Scaccabarozzi, M. M. Fejer, Y. Huo, S. Fan, X. Yu, and J. S. Harris, "Enhanced second-harmonic generation in AlGaAs/Al₂O₃ tightly confining waveguides and resonant cavities," *Opt. Lett.*, vol. 31, no. 24, pp. 3626–3628, Dec. 2006.
- [75] E. Rosencher and B. Vinter, *Optoelectronics*. Cambridge University Press, 2002.
- [76] G. Bloom, A. Grisard, E. Lallier, C. Larat, M. Carras, and X. Marcadet, "Optical parametric amplification of a distributed-feedback quantum-cascade laser in orientation-patterned GaAs," *Opt. Lett.*, vol. 35, no. 4, pp. 505–507, Feb. 2010.
- [77] S. Vasilyev *et al.*, "Broadly tunable single-frequency CW mid-infrared source with milliwatt-level output based on difference-frequency generation in orientation-patterned GaAs," *Opt. Lett.*, vol. 33, no. 13, pp. 1413–1415, Jul. 2008.
- [78] X. Yu, L. Scaccabarozzi, J. S. Harris, P. S. Kuo, and M. M. Fejer, "Efficient continuous wave second harmonic generation pumped at 1.55 μm in quasi-phase-matched AlGaAs waveguides," *Opt. Express*, vol. 13, no. 26, pp. 10742–10748, Dec. 2005.

- [79] M. W. Street *et al.*, "Modification of the second-order optical nonlinearities in AlGaAs asymmetric multiple quantum well waveguides by quantum well intermixing," *Appl. Phys. Lett.*, vol. 70, no. 21, pp. 2804–2806, May 1997.
- [80] A. S. Helmy *et al.*, "Quasi phase matching in GaAs–AlAs superlattice waveguides through bandgap tuning by use of quantum-well intermixing," *Opt. Lett.*, vol. 25, no. 18, pp. 1370–1372, Sep. 2000.
- [81] Marsh John H., "Quantum Well Intermixing Revolutionizes High Power Laser Diodes," *Laser Tech. J.*, vol. 4, no. 5, pp. 32–35, Nov. 2007.
- [82] Y. Dumeige and P. Féron, "Whispering-gallery-mode analysis of phase-matched doubly resonant second-harmonic generation," *Phys. Rev. A*, vol. 74, no. 6, p. 063804, Dec. 2006.
- [83] N. Morais *et al.*, "Directionally induced quasi-phase matching in homogeneous AlGaAs waveguides," *Opt. Lett.*, vol. 42, no. 21, pp. 4287–4290, Nov. 2017.
- [84] I. Biaggio, V. Coda, and G. Montemezzani, "Coupling-length phase matching for nonlinear optical frequency conversion in parallel waveguides," *Phys. Rev. A*, vol. 90, no. 4, p. 043816, Oct. 2014.
- [85] A. S. Helmy, B. Bijlani, and P. Abolghasem, "Phase matching in monolithic Bragg reflection waveguides," *Opt. Lett.*, vol. 32, no. 16, pp. 2399–2401, 2007.
- [86] L. A. Coldren, S. W. Corzine, and M. L. Mashanovitch, *Diode lasers and photonic integrated circuits*, vol. 218. John Wiley & Sons, 2012.
- [87] J. M. Gérard, J. B. Génin, J. Lefebvre, J. M. Moison, N. Lebouché, and F. Barthe, "Optical investigation of the self-organized growth of InAs/GaAs quantum boxes," *J. Cryst. Growth*, vol. 150, pp. 351–356, May 1995.
- [88] T. W. Schlereth, C. Schneider, W. Kaiser, S. Höfling, and A. Forchel, "Low threshold, high gain AlGaInAs quantum dot lasers," *Appl. Phys. Lett.*, vol. 90, no. 22, p. 221113, May 2007.
- [89] P. K. Tien, "Light Waves in Thin Films and Integrated Optics," *Appl. Opt.*, vol. 10, no. 11, pp. 2395–2413, Nov. 1971.
- [90] A. De Rossi *et al.*, "Measuring propagation loss in a multimode semiconductor waveguide," *J. Appl. Phys.*, vol. 97, no. 7, p. 073105, Mar. 2005.

- [91] P. Bhattacharya, Z. Mi, J. Yang, D. Basu, and D. Saha, "Quantum dot lasers: From promise to high-performance devices," *J. Cryst. Growth*, vol. 311, no. 7, pp. 1625–1631, Mar. 2009.
- [92] B. E. A. Saleh and M. C. Teich, *Fundamentals of Photonics*. Wiley, 2007.
- [93] Y. Arakawa and H. Sakaki, "Multidimensional quantum well laser and temperature dependence of its threshold current," *Appl. Phys. Lett.*, vol. 40, no. 11, pp. 939–941, Jun. 1982.
- [94] M. Asada, Y. Miyamoto, and Y. Suematsu, "Gain and the threshold of three-dimensional quantum-box lasers," *IEEE J. Quantum Electron.*, vol. 22, no. 9, pp. 1915–1921, Sep. 1986.
- [95] P. Borri, W. Langbein, J. M. Hvam, F. Heinrichsdorff, M.-H. Mao, and D. Bimberg, "Time-resolved four-wave mixing in InAs/InGaAs quantum-dot amplifiers under electrical injection," *Appl. Phys. Lett.*, vol. 76, no. 11, pp. 1380–1382, Mar. 2000.
- [96] M. Sugawara, K. Mukai, Y. Nakata, K. Otsubo, and H. Ishikawa, "Performance and physics of quantum-dot lasers with self-assembled columnar-shaped and 1.3- μm emitting InGaAs quantum dots," *IEEE J. Sel. Top. Quantum Electron.*, vol. 6, no. 3, pp. 462–474, 2000.
- [97] M. T. Crowley, N. A. Naderi, H. Su, F. Grillot, and L. F. Lester, "GaAs-Based Quantum Dot Lasers," in *Semiconductors and Semimetals*, vol. 86, Elsevier, 2012, pp. 371–417.
- [98] J. Wu, S. Chen, A. Seeds, and H. Liu, "Quantum dot optoelectronic devices: lasers, photodetectors and solar cells," *J. Phys. Appl. Phys.*, vol. 48, no. 36, p. 363001, Sep. 2015.
- [99] J. P. Reithmaier and A. Forchel, "Recent advances in semiconductor quantum-dot lasers," *Comptes Rendus Phys.*, vol. 4, no. 6, pp. 611–619, Jul. 2003.
- [100] S. G. Li *et al.*, "A review of external cavity-coupled quantum dot lasers," *Opt. Quantum Electron.*, vol. 46, no. 5, pp. 623–640, May 2014.
- [101] A. Somers, W. Kaiser, J. P. Reithmaier, A. Forchel, M. Gioaninni, and I. Montrosset, "Optical gain properties of InAs/InAlGaAs/InP quantum dash structures with a spectral gain bandwidth of more than 300 nm," *Appl. Phys. Lett.*, vol. 89, no. 6, p. 061107, Aug. 2006.

- [102] S. A. Moore, L. O'Faolain, M. A. Cataluna, M. B. Flynn, M. V. Kotlyar, and T. F. Krauss, "Reduced surface sidewall recombination and diffusion in quantum-dot lasers," *IEEE Photonics Technol. Lett.*, vol. 18, no. 17, pp. 1861–1863, Sep. 2006.
- [103] M. Munsch *et al.*, "Room temperature, continuous wave lasing in microcylinder and microring quantum dot laser diodes," *Appl. Phys. Lett.*, vol. 100, no. 3, p. 031111, Jan. 2012.
- [104] L. Harris, D. J. Mowbray, M. S. Skolnick, M. Hopkinson, and G. Hill, "Emission spectra and mode structure of InAs/GaAs self-organized quantum dot lasers," *Appl. Phys. Lett.*, vol. 73, no. 7, pp. 969–971, Aug. 1998.
- [105] S. M. Kim, Y. Wang, M. Keever, and J. S. Harris, "High-Frequency Modulation Characteristics of 1.3 μm Quantum Dot Lasers," *IEEE Photonics Technol. Lett.*, vol. 16, no. 2, pp. 377–379, Feb. 2004.
- [106] Y. Qiu, P. Gogna, S. Forouhar, A. Stintz, and L. F. Lester, "High-performance InAs quantum-dot lasers near 1.3 μm ," *Appl. Phys. Lett.*, vol. 79, no. 22, pp. 3570–3572, Nov. 2001.
- [107] A. D. Lee, T. Wang, F. Pozzi, A. J. Seeds, and H. Liu, "A room temperature electrically pumped 1.3- μm InAs quantum dot laser monolithically grown on silicon substrates," in *8th IEEE International Conference on Group IV Photonics*, 2011, pp. 184–186.
- [108] G. Bastard, "Wave mechanics applied to semiconductor heterostructures," Jan. 1990.
- [109] S. Cortez, O. Krebs, P. Voisin, and J. M. Gérard, "Polarization of the interband optical dipole in InAs/GaAs self-organized quantum dots," *Phys. Rev. B*, vol. 63, no. 23, May 2001.
- [110] M. Zieliński, "Fine structure of light-hole excitons in nanowire quantum dots," *Phys. Rev. B*, vol. 88, no. 11, Sep. 2013.
- [111] S. Gehrsitz, F. K. Reinhart, C. Gourgon, N. Herres, A. Vonlanthen, and H. Sigg, "The refractive index of $\text{Al}_x\text{Ga}_{1-x}\text{As}$ below the band gap: Accurate determination and empirical modeling," *J. Appl. Phys.*, vol. 87, no. 11, pp. 7825–7837, Jun. 2000.
- [112] M. A. Fromowitz, "Refractive index of $\text{Ga}_{1-x}\text{Al}_x\text{As}$," *Solid State Commun.*, vol. 15, no. 1, pp. 59–63, Jul. 1974.

- [113] S. Seifert and P. Runge, "Revised refractive index and absorption of $\text{In}_{1-x}\text{Ga}_x\text{As}_y\text{P}_{1-y}$ lattice-matched to InP in transparent and absorption IR-region," *Opt. Mater. Express*, vol. 6, no. 2, pp. 629–639, Feb. 2016.
- [114] G. D. Pettit and W. J. Turner, "Refractive Index of InP," *J. Appl. Phys.*, vol. 36, no. 6, pp. 2081–2081, Jun. 1965.
- [115] S. H. Wemple and M. DiDomenico, "Behavior of the Electronic Dielectric Constant in Covalent and Ionic Materials," *Phys. Rev. B*, vol. 3, no. 4, pp. 1338–1351, Feb. 1971.
- [116] F. Heinrichsdorff *et al.*, "Room-temperature continuous-wave lasing from stacked InAs/GaAs quantum dots grown by metalorganic chemical vapor deposition," *Appl. Phys. Lett.*, vol. 71, no. 1, pp. 22–24, Jul. 1997.
- [117] L. Landin *et al.*, "Optical investigation of InAs/InP quantum dots at different temperatures and under electric field," *Thin Solid Films*, vol. 364, no. 1–2, pp. 161–164, Mar. 2000.
- [118] T. Ikegami, "Reflectivity of mode at facet and oscillation mode in double-heterostructure injection lasers," *IEEE J. Quantum Electron.*, vol. 8, no. 6, pp. 470–476, Jun. 1972.
- [119] J. E. Ripper, J. C. Dymont, L. A. D'Asaro, and T. L. Paoli, "Stripe-geometry double-heterostructure junction lasers: mode structure and CW operation above room temperature," *Appl. Phys. Lett.*, vol. 18, no. 4, pp. 155–157, Feb. 1971.
- [120] S. Rapp, "Long-wavelength vertical-cavity lasers based on InP/GaInAsP Bragg reflectors," PhD Thesis, Institutionen för elektronisk systemkonstruktion, 1999.
- [121] T. Dupont, "Réalisation de sources laser III-V sur silicium," PhD Thesis, Ecole Centrale de Lyon, 2011.
- [122] S. Adachi, *Physical Properties of III-V Semiconductor Compounds*. John Wiley & Sons, 1992.
- [123] S. W. Corzine, R. H. Yan, and L. A. Coldren, "Theoretical gain in strained InGaAs/AlGaAs quantum wells including valence-band mixing effects," *Appl. Phys. Lett.*, vol. 57, no. 26, pp. 2835–2837, Dec. 1990.

- [124] J. S. Osinski, Y. Zou, P. Grodzinski, A. Mathur, and P. D. Dapkus, "Low-threshold-current-density 1.5 μm lasers using compressively strained InGaAsP quantum wells," *IEEE Photonics Technol. Lett.*, vol. 4, no. 1, pp. 10–13, 1992.
- [125] F. Klopf, J. P. Reithmaier, and A. Forchel, "Highly efficient GaInAs/(Al)GaAs quantum-dot lasers based on a single active layer versus 980 nm high-power quantum-well lasers," *Appl. Phys. Lett.*, vol. 77, no. 10, pp. 1419–1421, Aug. 2000.
- [126] F. Lelarge *et al.*, "Recent Advances on InAs/InP Quantum Dash Based Semiconductor Lasers and Optical Amplifiers Operating at 1.55 μm ," *IEEE J. Sel. Top. Quantum Electron.*, vol. 13, no. 1, pp. 111–124, Jan. 2007.
- [127] D. G. Deppe, K. Shavritranuruk, G. Ozgur, H. Chen, and S. Freisem, "Quantum dot laser diode with low threshold and low internal loss," *Electron. Lett.*, vol. 45, no. 1, pp. 54–56, Jan. 2009.
- [128] B. Broberg and S. Lindgren, "Refractive index of $\text{In}_{1-x}\text{Ga}_x\text{As}_y\text{P}_{1-y}$ layers and InP in the transparent wavelength region," *J. Appl. Phys.*, vol. 55, no. 9, pp. 3376–3381, May 1984.
- [129] M. Amiotti and G. Landgren, "Ellipsometric determination of thickness and refractive index at 1.3, 1.55, and 1.7 μm for $\text{In}_{(1-x)}\text{Ga}_x\text{As}_y\text{P}_{(1-y)}$ films on InP," *J. Appl. Phys.*, vol. 73, no. 6, pp. 2965–2971, Mar. 1993.
- [130] F. Fiedler and A. Schlachetzki, "Optical parameters of InP-based waveguides," *Solid-State Electron.*, vol. 30, no. 1, pp. 73–83, Jan. 1987.
- [131] C. Henry, L. Johnson, R. Logan, and D. Clarke, "Determination of the refractive index of InGaAsP epitaxial layers by mode line luminescence spectroscopy," *IEEE J. Quantum Electron.*, vol. 21, no. 12, pp. 1887–1892, Dec. 1985.
- [132] P. Chandra, L. A. Coldren, and K. E. Strege, "Refractive index data from $\text{Ga}_x\text{In}_{1-x}\text{As}_y\text{P}_{1-y}$ films," *Electron. Lett.*, vol. 17, no. 1, pp. 6–7, Jan. 1981.
- [133] G. Sonek *et al.*, "Dielectric properties of GaAs/AlGaAs multiple quantum well waveguides," *IEEE J. Quantum Electron.*, vol. 22, no. 7, pp. 1015–1018, Jul. 1986.
- [134] C. Alibert, M. Skouri, A. Joullie, M. Benouna, and S. Sadiq, "Refractive indices of AlSb and GaSb-lattice-matched $\text{Al}_x\text{Ga}_{1-x}\text{As}_y\text{Sb}_{1-y}$ in the transparent wavelength region," *J. Appl. Phys.*, vol. 69, no. 5, pp. 3208–3211, Mar. 1991.

- [135] P. Martin, E. M. Skouri, L. Chusseau, C. Alibert, and H. Bissessur, "Accurate refractive index measurements of doped and undoped InP by a grating coupling technique," *Appl. Phys. Lett.*, vol. 67, no. 7, pp. 881–883, Aug. 1995.
- [136] G. Leo *et al.*, "X-ray and optical characterization of multilayer AlGaAs waveguides," *Appl. Phys. Lett.*, vol. 77, no. 24, pp. 3884–3886, Dec. 2000.
- [137] E. M. Skouri *et al.*, "Measurement of the refractive index of GaInAs/InP quantum wells by a grating coupling technique," *Appl. Phys. Lett.*, vol. 67, no. 23, pp. 3441–3443, Dec. 1995.
- [138] E. Kuphal, "Phase diagrams of InGaAsP, InGaAs and InP lattice-matched to (100)InP," *J. Cryst. Growth*, vol. 67, no. 3, pp. 441–457, Aug. 1984.
- [139] G. P. Agrawal and N. K. Dutta, "Long wavelength semiconductor lasers," Jan. 1986.
- [140] S. Adachi, "Material parameters of $\text{In}_{1-x}\text{Ga}_x\text{As}_y\text{P}_{1-y}$ and related binaries," *J. Appl. Phys.*, vol. 53, no. 12, pp. 8775–8792, Dec. 1982.
- [141] P. Barritault, M. Brun, P. Labeye, O. Lartigue, J.-M. Hartmann, and S. Nicoletti, "M-lines characterization of the refractive index profile of SiGe gradient waveguides at 2.15 μm ," *Opt. Express*, vol. 21, no. 9, p. 11506, May 2013.
- [142] C. Tanguy, "Refractive index of direct bandgap semiconductors near the absorption threshold: influence of excitonic effects," *IEEE J. Quantum Electron.*, vol. 32, no. 10, pp. 1746–1751, Oct. 1996.
- [143] G. A. Porkolab, P. Apiratikul, B. Wang, S. H. Guo, and C. J. K. Richardson, "Low propagation loss AlGaAs waveguides fabricated with plasma-assisted photoresist reflow," *Opt. Express*, vol. 22, no. 7, p. 7733, Apr. 2014.
- [144] O. Auciello, A. Gras-Marti, J. A. Valles-Abarca, and D. L. Flamm, Eds., *Plasma-Surface Interactions and Processing of Materials*. Dordrecht: Springer Netherlands, 1990.
- [145] J. W. Lee *et al.*, "Plasma etching of III–V semiconductors in BCl_3 chemistries: Part I: GaAs and related compounds," *Plasma Chem. Plasma Process.*, vol. 17, no. 2, pp. 155–167, Jun. 1997.
- [146] S. Agarwala *et al.*, "High-density inductively coupled plasma etching of GaAs/AlGaAs in $\text{BCl}_3/\text{Cl}_2/\text{Ar}$: A study using a mixture design experiment," *J. Vac.*

Sci. Technol. B Microelectron. Nanometer Struct. Process. Meas. Phenom., vol. 16, no. 2, pp. 511–514, Mar. 1998.

[147] S. Agarwala *et al.*, “Response surface study of inductively coupled plasma etching of GaAs/AlGaAs in BCl₃/Cl₂,” *J. Vac. Sci. Technol. Vac. Surf. Films*, vol. 17, no. 1, pp. 52–55, Jan. 1999.

[148] T. Maeda *et al.*, “Inductively coupled plasma etching of III–V semiconductors in BCl₃-based chemistries: I. GaAs, GaN, GaP, GaSb and AlGaAs,” *Appl. Surf. Sci.*, vol. 143, no. 1, pp. 174–182, Apr. 1999.

[149] S. S. Cooperman, “Reactive ion etching of GaAs and AlGaAs in a BCl₃-Ar discharge,” *J. Vac. Sci. Technol. B Microelectron. Nanometer Struct.*, vol. 7, no. 1, p. 41, Jan. 1989.

[150] J. Daleiden, “Chemical analysis of a Cl₂/BCl₃/IBr₃ chemically assisted ion-beam etching process for GaAs and InP laser-mirror fabrication under cryo-pumped ultrahigh vacuum conditions,” *J. Vac. Sci. Technol. B Microelectron. Nanometer Struct.*, vol. 13, no. 5, p. 2022, Sep. 1995.

[151] R. J. Shul and S. J. Pearton, Eds., *Handbook of Advanced Plasma Processing Techniques*. Springer, 2000.

[152] S. J. Pearton, “Reactive ion etching of GaAs, AlGaAs, and GaSb in Cl₂ and SiCl₄,” *J. Vac. Sci. Technol. B Microelectron. Nanometer Struct.*, vol. 8, no. 4, p. 607, Jul. 1990.

[153] P. Yinsheng *et al.*, “Optimization of inductively coupled plasma etching for low nanometer scale air-hole arrays in two-dimensional GaAs-based photonic crystals,” *J. Semicond.*, vol. 31, no. 1, p. 012003, Jan. 2010.

[154] E. W. Berg and S. W. Pang, “Low-Pressure Etching of Nanostructures and Via Holes Using an Inductively Coupled Plasma System,” *J. Electrochem. Soc.*, vol. 146, no. 2, pp. 775–779, Feb. 1999.

[155] L. Jalabert *et al.*, “High aspect ratio GaAs nanowires made by ICP-RIE etching using Cl₂/N₂ chemistry,” *Microelectron. Eng.*, vol. 85, no. 5–6, pp. 1173–1178, May 2008.

[156] M. Volatier, D. Duchesne, R. Morandotti, R. Arès, and V. Aimez, “Extremely high aspect ratio GaAs and GaAs/AlGaAs nanowaveguides fabricated using

chlorine ICP etching with N₂-promoted passivation," *Nanotechnology*, vol. 21, no. 13, p. 134014, Apr. 2010.

[157] K. A. Atlasov, P. Gallo, A. Rudra, B. Dwir, and E. Kapon, "Effect of sidewall passivation in BCl₃/N₂ inductively coupled plasma etching of two-dimensional GaAs photonic crystals," *J. Vac. Sci. Technol. B Microelectron. Nanometer Struct. Process. Meas. Phenom.*, vol. 27, no. 5, pp. L21–L24, Aug. 2009.

[158] R. Braive *et al.*, "Inductively coupled plasma etching of GaAs suspended photonic crystal cavities," *J. Vac. Sci. Technol. B Microelectron. Nanometer Struct. Process. Meas. Phenom.*, vol. 27, no. 4, pp. 1909–1914, Jul. 2009.

[159] S. Varoutsis *et al.*, "Reactive-ion etching of high-Q and submicron-diameter GaAs/AlAs micropillar cavities," *J. Vac. Sci. Technol. B Microelectron. Nanometer Struct. Process. Meas. Phenom.*, vol. 23, no. 6, pp. 2499–2503, Nov. 2005.

[160] W. Hease, "Disques optomécaniques en arseniure de gallium dans le régime quantique," 2016.

[161] F. Karouta, "A practical approach to reactive ion etching," *J. Phys. Appl. Phys.*, vol. 47, no. 23, p. 233501, Jun. 2014.

[162] S. Golka, M. Austerer, C. Pflügl, W. Schrenk, and G. Strasser, "Processing of deeply etched GaAs/AlGaAs quantum cascade lasers with grating structures," *MRS Online Proc. Libr. Arch.*, vol. 829, 2004.

[163] J. W. Lee *et al.*, "Advanced selective dry etching of GaAs/AlGaAs in high density inductively coupled plasmas," *J. Vac. Sci. Technol. Vac. Surf. Films*, vol. 18, no. 4, pp. 1220–1224, Jul. 2000.

[164] M. Aoki *et al.*, "InGaAs/InGaAsP MQW electroabsorption modulator integrated with a DFB laser fabricated by band-gap energy control selective area MOCVD," *IEEE J. Quantum Electron.*, vol. 29, no. 6, pp. 2088–2096, Jun. 1993.

[165] A. W. Fang, H. Park, O. Cohen, R. Jones, M. J. Paniccia, and J. E. Bowers, "Electrically pumped hybrid AlGaInAs-silicon evanescent laser," *Opt. Express*, vol. 14, no. 20, pp. 9203–9210, Oct. 2006.

[166] X. Sun and A. Yariv, "Engineering supermode silicon/III-V hybrid waveguides for laser oscillation," *JOSA B*, vol. 25, no. 6, pp. 923–926, Jun. 2008.

- [167] X. Sun, H.-C. Liu, and A. Yariv, "Adiabaticity criterion and the shortest adiabatic mode transformer in a coupled-waveguide system," *Opt. Lett.*, vol. 34, no. 3, pp. 280–282, Feb. 2009.
- [168] Fengnian Xia, V. M. Menon, and S. R. Forrest, "Photonic integration using asymmetric twin-waveguide (ATG) technology: part I-concepts and theory," *IEEE J. Sel. Top. Quantum Electron.*, vol. 11, no. 1, pp. 17–29, Jan. 2005.
- [169] Y. Ding, J. Xu, F. Da Ros, B. Huang, H. Ou, and C. Peucheret, "On-chip two-mode division multiplexing using tapered directional coupler-based mode multiplexer and demultiplexer," *Opt. Express*, vol. 21, no. 8, p. 10376, Apr. 2013.
- [170] X. Liang, J. Mu, X. Li, and Y. Xi, "Efficient Active-to-Passive Light Coupling of InGaAsP/InP Laser Using Subwavelength Coupler," *IEEE Photonics J.*, vol. 5, no. 6, pp. 6602408–6602408, Dec. 2013.
- [171] L.-W. Luo *et al.*, "WDM-compatible mode-division multiplexing on a silicon chip," *Nat. Commun.*, vol. 5, Jan. 2014.
- [172] H. Wenzel *et al.*, "Fundamental-Lateral Mode Stabilized High-Power Ridge-Waveguide Lasers With a Low Beam Divergence," *IEEE Photonics Technol. Lett.*, vol. 20, no. 3, pp. 214–216, Feb. 2008.
- [173] M. Beaudoin, A. J. G. DeVries, S. R. Johnson, H. Laman, and T. Tiedje, "Optical absorption edge of semi-insulating GaAs and InP at high temperatures," *Appl. Phys. Lett.*, vol. 70, no. 26, pp. 3540–3542, Jun. 1997.
- [174] M. Krakowski *et al.*, "Very high-power broad area laser diode with internal wavelength stabilization at 975 nm for Yb fibre laser pumping," in *Novel In-Plane Semiconductor Lasers XIII*, 2014, vol. 9002, p. 90021G.
- [175] K. Dridi, A. Benhsaien, A. Akrouf, J. Zhang, and T. Hall, "Narrow-linewidth three-electrode regrowth-free semiconductor DFB lasers with uniform surface grating," in *Novel In-Plane Semiconductor Lasers XII*, 2013, vol. 8640, p. 864009.